TOPICAL REVIEW • OPEN ACCESS

Electronic and geometric determinants of adsorption: fundamentals and applications

IOP Publishing J. Phys. Energy 3 (2021) 022001 https://doi.org/10.1088/2515-7655/abd295

Journal of Physics: Energy

TOPICAL REVIEW

Electronic and geometric determinants of adsorption: fundamentals and applications

Bo Li, Wang Gao and Qing Jiang

Key Laboratory of Automobile Materials, Ministry of Education, and College of Materials Science and Engineering, Jilin University, Changchun 130022, People's Republic of China

E-mail: wgao@jlu.edu.cn **and** Jiangq@jlu.edu.cn

Keywords: adsorption, electronic structure, geometric structure, catalysis

OPEN ACCESS

RECEIVED
1 May 2020

REVISED
13 July 2020

ACCEPTED FOR PUBLICATION
10 December 2020

PUBLISHED
28 January 2021

Abstract

Adsorption is an essential phenomenon in surface science and is closely related to many applications such as catalysis, sensors, energy storage, biomedical applications and so on. It is widely accepted that the adsorption properties are determined by the electronic and geometric structures of substrates and adsorbates. The *d*-band model and the generalized coordination number model take the electronic and geometric structures of substrates into consideration respectively, successfully rationalizing the trends of adsorption on transition metals (TMs), TM nanoparticles (NPs) and some TM alloys. The linear scaling relationship (LSR) uncovers the role of the electronic structures of adsorbates in adsorption and allow the ascertainment of the trend of adsorption between different adsorbates. Recently, we develop an effective model to correlate adsorption energy with the easily accessible intrinsic electronic and geometric properties of substrates and adsorbates which holds for TMs, TM NPs, near-surface alloys and oxides. This intrinsic model can naturally derive the LSR and its generalized form, indicates the efficiency and limitation of engineering the adsorption energy and reaction energy, and enables rapid screening of potential candidates and designing of catalysts since all parameters are accessible and predictable. In this comprehensive review, we summarize these models to clarify their development process and uncover their connection and distinction, thereby drawing an explicit and overall physical picture of adsorption. Consequently, we provide a more comprehensive understanding about the broad applications of these models in catalysis. The theoretical part introduces necessary theoretical foundations and several well-built models with respect to the electronic models, the geometric models, the LSR and the intrinsic model. The application section describes their broad scope in catalysis, including oxygen reduction reaction, CO_2 reduction reaction and nitrogen reduction reaction. We believe this review will provide necessary and fundamental background knowledge to further understand the underlying mechanism of adsorption and offer beneficial guidance for the rapid screening of catalysts and materials design.

1. Introduction

Adsorption is one of the most important phenomena on solid surfaces and is often essential in determining the application of materials in many fields, such as catalysis, energy storage, biomedical applications and so on [1–4]. For instance, a catalytic process consists of several elementary steps: adsorbing the reactants to surface, diffusing on surface, breaking some bonds and forming new bonds, and eventually desorbing from surface [5]. According to the Sabatier principle [6], an 'ideal catalyst' should bind the reactants and products neither too strong nor too weak. The too weak (strong) binding strength gives rise to the difficulty of the dissociative chemisorption of reactants (desorption of products), reducing the activity of catalyst. Furthermore, the Brønsted–Evans–Polanyi relation [7] has verified that the activation energy of a certain

reaction depends strongly on the reaction energy, indicating that the reaction kinetics is also related to the properties of adsorption. Hence, determining the adsorption energy on various materials has been one of the central goals in the fields.

Adsorption can occur between numerous adsorbates and substrates and forms a variety of adsorption systems. Small molecules such as species binding via O, C, and N are likely the simplest adsorbates and are the most widely studied ones, since they are the important intermediates for oxygen reduction reaction (ORR), oxygen evolution reaction, N_2 reduction reaction (NRR), CO_2 reduction reaction (CO_2RR), and the decomposition and/or oxidation of CH_4, CH_3OH and HCOOH. The corresponding substrates contain pure transition metals (TMs), nanoparticles (NPs), alloys, oxides, carbides, nitrides, sulfides and single-atom catalysts (SACs). The diverse adsorption systems bring multiple factors to adsorption properties, including the materials-dependent nature, sites and facets selectivity, strain and coverage, not to mention temperature and pressure. Generally, the electronic nature and geometric structure of adsorbates and substrates are the basis of these factors' effects. Therefore, identifying the electronic and geometric determinants of adsorption and the underlying mechanism has been a long-term goal in past decades.

The rapid development of density functional theory (DFT) methods makes it possible to systematically study the general properties of adsorption without complicated experimental costs and external interferences, in particular in providing atomic-scale mechanistic insight for adsorption. Accordingly, several successful models in regard to the electronic and geometric determinants of adsorption are put forward, rationalizing the general trends of adsorption for variant adsorbates and substrates. The *d*-band model by Nørskov *et al* [5, 8, 9] considers a surface chemisorption as a two-step interaction between the states of adsorbates and surface atoms, suggesting that it is the *d*-states of TMs that determine the variation of adsorption strength from one metal to the next, which holds for a wide range of metal systems including pure TMs (in particular the late TMs), some alloys, some TM surfaces with strains, TM surfaces with promoters and poisons [10–24]. The generalized coordination number ($\overline{CN}$) model [25, 26], a first-order extension of the usual coordination number, is used to describe the local geometric environment on surface. This simple arithmetical descriptor effectively characterizes the geometric effects of pure TMs and NPs for adsorption [27–31], providing rational theoretical guidance for engineering surface structures to reach optimal catalytic activity. Besides the electronic and geometric descriptors of substrates, Nørskov *et al* [32] also identified the linear scaling relationship (LSR) for the adsorption energies between atoms and their partially hydrogenated species on TM surfaces, implying that the slope of the LSR strongly depends on the valence of central atoms of adsorbates. Calle-Vallejo *et al* [33] generalize the LSR by taking the structure sensitivity into account, suggesting that the offset of LSR is dominated by the coordination of active sites. The LSR, established from the electron counting rules and bond-order conservation theory, explicitly elaborates the general trends of adsorption for different adsorbates and uncover some adsorption limitations of reactions on TMs and NPs. Recently, we develop an effective intrinsic model to describe adsorption energy based on three main factors: the valence of adsorbates, the valence and electronegative of surface atoms, and the coordination of active sites, which holds for a variety of materials including pure TMs, NPs, near-surface alloys (NSAs) and oxides [34]. This intrinsic model correlates the adsorption energy with the intrinsic electronic and geometric properties of adsorption systems, deduces the existing LSR naturally, clarifies the efficiency and limitation in modulating the adsorption energy and reaction energy, and enables the rapid materials design, consequently offering a novel physical picture of adsorption.

In this review, we report several models to describe the electronic and geometric determinants of adsorption, clarify their development process and uncover their connection and distinction, thereby drawing an explicit and overall physical picture of adsorption. Consequently, we provide a more comprehensive understanding about the broad applications of these models in catalysis. In section 2, we introduce necessary theoretical foundations for several well-built models such as the electronic models, the geometric models, the LSR and the intrinsic model. Section 3 exhibits their broad scope in catalysis, including ORR, CO_2RR and NRR. In section 4, we summarize the main conclusions in this review and present the future scopes of adsorption field.

2. Theoretical foundations

Many attempts have been made to uncover adsorption properties, laying necessary foundations for comprehensively understanding the physical picture of adsorption. So far, many important understandings are based on numerical calculations and theoretical models. The former uses the advanced calculation methods such as DFT to obtain the electronic and geometric information and energetics of adsorption systems, while the latter sets out from the physical background to understand the underlying mechanisms of adsorption such as the crystal orbital overlap population (COOP), the frontier orbital theory and the

effective medium theory (EMT). Benefit from these contributions, the subsequent electronic and geometric models to explain the adsorption properties have achieved great success.

2.1. DFT calculations

With the substantial enhancement of the performance of computers, quantum theoretical calculations have attracted extensive attention [35–37]. DFT calculations can verify the rationality and reliability of experiments and fulfill the simulations with extreme conditions that are not realizable experimentally. Most importantly, they can set out from the view of electronic and geometric structures to elaborate the mechanism of numerous phenomena, thereby providing beneficial guidance for experiments.

In DFT, the energy of a given system is a function of the electron density (n) according to the Kohn–Sham (K–S) single-electron approximation [38, 39], which can be expressed as,

$$E(n) = T(n) + \int \mathrm{d}^3 r n(r) V_{\mathrm{ext}}(r) + \frac{1}{8\pi\varepsilon_0} \int \mathrm{d}^3 r \int \mathrm{d}^3 r' n(\mathrm{r}') \frac{1}{(r-r')} n(r) + E_{\mathrm{xc}}(n) \quad (1)$$

$T(n)$ is the kinetic energy term, the second and the third term represent the external potential energy (interaction between nucleus and electron) and the Coulomb potential energy, and $E_{\mathrm{xc}}(n)$ is the exchange-correlation energy. Note that only the $E_{\mathrm{xc}}(n)$ term in equation (1) contains approximations that are necessary for calculations, namely equation (1) provides the possibility of accurately solving the Schrödinger equation as long as the exchange-correlation functionals are sufficiently accurate. Therefore, finding the appropriate exchange-correlation functional is the most crucial issue with respect to DFT calculations, which controls the error of calculations.

The commonly used exchange-correlation functionals can be classified into five categories based on the Jacob's ladder [40, 41]. The first rung is the local spin density approximation [42], which is obtained with homogenous electron gas model. The second rung is the functional with the various degree of gradient corrections for electron density, namely the generalized gradient approximation (GGA) [43], in which Perdew–Burke–Ernzerhof (PBE) functional [44] yields reasonable accuracy for a large variety of systems and is one of the most widely used functionals. The third rung of the ladder is the meta-GGA that adds the local spin kinetic density into GGA. The fourth rung is hybrid functional (could be either GGA or meta-GGA), which usually admixes a fraction of Hartree–Fork exchange to the GGA- or meta-GGA-based exchange, such as Heyd–Scuseria–Ernzerhof [45], B3LYP [46] and M06-class functionals [47–49]. Hybrid functionals can be sufficiently accurate but are computationally very demanding. The double hybrid density functional (DHDF) locates at the fifth rung which mixes the electron correlation corrections to the hybrid functional. For adsorption, GGAs are commonly used functionals and can reach reasonable accuracy, with the error of adsorption energy about ±0.2 eV. For instance, Hammer, Hansen, Nørskov modified PBE functional (rPBE) [50] is often used to calculate adsorption properties. However, GGA does not consider the orbital kinetic energy density, suffers the empirical error of self-interactions and lacks the van der Waals (vdW) interactions, which play crucial roles in many systems. Hence, other functionals such as meta-GGA and DHDF and the accurate vdW interactions must be adopted for describing the specific adsorption systems.

Meta-GGA is one of the most popular functionals at present by simultaneously considering the electron density, the gradient of electron density and the orbital kinetic energy density [51], among which the M06-class functionals [47–49] are suitable for a large variety of systems and the strongly constrained appropriately normed (SCAN) functional [52] is expected to be one of the most promising functionals to describe all kinds of interactions within systems. Both of these two kinds of functionals can be used to characterize the properties of adsorption. M06-class functionals belong to hybrid functionals that mix Hartree–Fork exchange and DFT exchange, including M06-L [48], M06-HF [47], M06 and M06-2X [49]. M06-L is a local functional and performs well at TM area. The local constraint makes it inefficient in main-group compounds, transition states and non-covalent interactions. M06-HF, possessing the full Hartree–Fork exchange, is expected to be the only functional that can describe the electronically excited states with useful accuracy, while is not applicable for TMs. M06 functional admixes partial Hartree–Fork exchange to the PBE exchange and is mainly suitable for TMs and nonmetals. M06-2X is similar to M06 but with twice the Hartree–Fork exchange mixing (2X), which performs well only for nonmetals. SCAN is the first nonempirical meta-GGA that fulfills all the 17 known constraints that a meta-GGA can. Some appropriate norms such as rare-gas atoms and nonbonded interactions are also added into SCAN. These characteristics of SCAN lead to the significantly better performance for both energies and geometries than LDA and PBE. Remarkably, SCAN yields comparable accuracy for a large amount of materials (even for soft materials), covering metallic, covalent, ionic, hydrogen and intermediate-vdW bondings [53]. Moreover, the computational cost of SCAN is close to that of GGA, which makes SCAN promising for predicting the electronic and geometric properties of materials.

DHDF combines a standard hybrid function with the non-local electron correlation treated by second-order perturbation theory, which can be sufficiently accurate for thermodynamic data and can also be used to predict important quantities such as reaction energies, barrier heights and isomerization energies. The first DHDF is B2PLYP developed by Grimme [54], containing the B88 exchange and LYP correlation, which are followed with several modifications such as B2GPPLYP [55], DSD-BLYP [56], PTPSS and PWPB95 functionals [57]. B2GPPLYP follows the same strategy as B2PLYP but with different amounts of the Hartree–Fork exchange and perturbative correlation mixing. DSD-BLYP also uses the B88 exchange and LYP correlation, while the perturbative part depends on the spin-component scaling idea. PTPSS and PWPB95 use the different ingredients from B2PLYP: TPSS exchange and correlation for PTPSS, and PW exchange and B95 correlation for PWPB95. Both of these two functionals are sufficiently accurate for main group compounds and show good performances for TMs. Moreover, there exist other kinds of DHDFs such as XYG3 [58]. XYG3 includes the nonlocal orbital-dependent component in the exchange and the unoccupied K–S orbitals' information in the correlation, performing well for thermochemistry, reaction barrier heights, and nonbond interactions of main group compounds. It is noteworthy that one evident shortcoming of DHDFs is the underestimation of the long-range vdW interactions (only 25% semi-local correlation is corrected by perturbation). Hence, Grimme applied the D3 approach (what will be introduced in the following) into DHDFs for capturing the long-range dispersion energy [59]. Furthermore, although DHDFs yield highly accurate results, the computational costs are extremely demanding that are usually N^5 or N^4 (N denotes the size of system), hampering its application to large-scale systems.

The vdW interactions are indispensable for numerous systems especially for large-scale molecules such as DNA, proteins, aggregates, and vdW heterostructures [60]. However, conventional exchange-correlation functional with GGA cannot describe accurately the long-range vdW forces. Many methods have been proposed to solve this issue, of which the most widely accepted methods are the DFT+D approach (such as the D1–D3 approaches by Grimme [61] and the Tkatchenko–Scheffler (TS)-based models by Tkatchenko and Scheffler [62]) and the vdW-DF method [63]. The DFT+D approach considers an additional dispersion correction to the self-consistent K–S energy while the vdW-DF method directly applies the correction to the exchange-correlation function.

Wu *et al* firstly proposed the idea of dispersion corrected DFT method and tried it on molecular dimers and metal carbonyls [64]. Then Grimme systematically developed a series of DFT+D approaches to consider the dispersion energy. The dispersion corrected total energy is given as,

$$E = E_{\mathrm{DFT}} + E_{\mathrm{vdW}} \tag{2}$$

where E_{DFT} is the usual self-consistent K–S energy calculated by chosen functional. E_{vdW} is the dispersion correction which can be expressed as,

$$E_{\mathrm{vdW}} = -\frac{1}{2}\sum_{\mathrm{A,B}} f_{\mathrm{damp}}\left(R_{\mathrm{AB}}, R_{\mathrm{A}}^{0}, R_{\mathrm{B}}^{0}\right) C_{6\mathrm{AB}} R_{\mathrm{AB}}^{-6} \tag{3}$$

where R_{AB} denotes the interatomic distance between atom pair A and B, R_{A}^{0} and R_{B}^{0} are the vdW radii for atoms A and B, and $C_{6\mathrm{AB}}$ represents the corresponding C_6 coefficient. f_{damp} is the damping function that is necessary to avoid the near-singularities for small R. According to equation (3), it is most important to determine the C_6 coefficient for calculating the vdW forces. For D1 approach [65], C_6 coefficient is obtained as,

$$C_{6\mathrm{AB}} = 2\frac{C_{6\mathrm{AA}} C_{6\mathrm{BB}}}{C_{6\mathrm{AA}} + C_{6\mathrm{BB}}} \tag{4}$$

$C_{6\mathrm{AA}}$ and $C_{6\mathrm{BB}}$ are the free atom reference values of C_6 coefficient of A and B, which are cited from experiments. DFT+D1 approach can give a reasonable description of the pairwise vdW interactions while possesses some empirical properties since the C_6 coefficient is taken from experiments. As a successor of D1 approach, D2 approach [66] uses the geometric mean of the homoatomic C_6 coefficient between A and B as,

$$C_{6\mathrm{AB}} = \sqrt{C_{6\mathrm{AA}} C_{6\mathrm{BB}}} \tag{5}$$

The homoatomic C_6 coefficient is obtained with $C_{6\mathrm{AA}} = 0.05 N I_{\mathrm{p}}^{\mathrm{a}} \alpha^{\mathrm{a}}$, where N is equal to 2, 10, 18, 36 and 54 for atoms corresponding to the period number 1–5 of the periodic table, I_{p} and α are the atomic ionization potentials and static dipole polarizability. D2 approach eliminates some degree of the empiricism of D1 approach and represents one of the first semiclassical methods to describe the vdW interactions which holds

for a large amount of elements of the periodic table. However, this approach loses efficiency for molecular environment. Then in 2010, Grimme *et al* proposed D3 approach [67] to consider the many-body interactions by using the concept of coordination numbers. Overall, D1–D3 series methods provide the effective descriptions of the long-range vdW interactions and are widely used in many systems.

Tkatchenko and Scheffler proposed a density-dependent scheme to consider the vdW interactions (TS-vdW) [68]. The C_6 coefficient is calculated as follows,

$$C_{6\mathrm{AB}} = 2\frac{C_{6\mathrm{AA}}C_{6\mathrm{BB}}}{\frac{\alpha_{\mathrm{B}}^0}{\alpha_{\mathrm{A}}^0}C_{6\mathrm{AA}} + \frac{\alpha_{\mathrm{A}}^0}{\alpha_{\mathrm{B}}^0}C_{6\mathrm{BB}}} \tag{6}$$

where α_{A}^0 and α_{B}^0 is the static polarizability of atoms A and B. For free atoms, α^0 and C_6 are extracted from literature. For atoms in molecules or solids, α^0 and C_6 are calculated by the effective volume (V^{eff}) as,

$$C_{6\mathrm{AA}}^{\mathrm{eff}} = \left(\frac{V_{\mathrm{A}}^{\mathrm{eff}}}{V_{\mathrm{A}}^{\mathrm{free}}}\right)^2 C_{6\mathrm{AA}}^{\mathrm{free}} \tag{7}$$

$$\alpha_{\mathrm{A}}^{\mathrm{eff}} = \left(\frac{V_{\mathrm{A}}^{\mathrm{eff}}}{V_{\mathrm{A}}^{\mathrm{free}}}\right)\alpha_{\mathrm{A}}^{\mathrm{free}} \tag{8}$$

The TS-vdW method effectively describes the pairwise dispersion energy of which the electronic structures are captured by the Hirshfeld partitioning [69, 70] and the precomputed parameters ensure the simple calculation of the C_6 coefficient. However, this scheme does not contain the long-range electrostatic screening effects that are important in both short- and long-range effects of the environment. Therefore, the original TS-vdW method was extended by Tkatchenko *et al* [71] to consider the long-range screening effects in the effective atomic polarizabilities by solving the classical electrodynamics self-consistent screening (SCS) equation,

$$\alpha^{\mathrm{SCS}}(\mathrm{r};i\omega) = \alpha^{\mathrm{TS}}(\mathrm{r};i\omega) + \alpha^{\mathrm{TS}}(\mathrm{r};i\omega)\int \mathrm{d}\mathrm{r}'\tau(\mathrm{r}-r')\alpha^{\mathrm{SCS}}(r';i\omega) \tag{9}$$

where $\alpha^{\mathrm{TS}}(\mathrm{r};i\omega)$ represents the sum of the TS-vdW effective polarizabilities and $\tau(\mathrm{r}–\mathrm{r}')$ denotes the dipole-dipole interaction tensor. Thus the screened polarizability α^{SCS} and screened static polarizability $\alpha^{0,\mathrm{SCS}}$ computed by equation (9) are used to calculate the screened C_6 coefficient $C_{6,\mathrm{SCS}}$. Furthermore, the many-body dispersion (MBD) [71, 72] interactions can be well described by TS-based methods using the coupled fluctuating dipole model [73, 74]. The MBD correction alleviates the shortcoming of TS method that overestimates the dispersion energy. Particularly, Tkatchenko *et al* also proposed an effective method (TSsurf) [75] to describe the adsorption on metal surfaces by considering the nonlocal Coulomb screening within the bulk via combining the TS-vdW method with the Lifshitz–Zaremba–Kohn (LZK) theory. The screened heteronuclear $C_{6,\mathrm{LZK}}^{ab}$ interaction coefficient is calculated by the homonuclear C_6^{aa} and $C_{6,\mathrm{LZK}}^{bb}$ coefficient,

$$C_{6,\mathrm{LZK}}^{ab} = \frac{2C_6^{aa}C_{6,\mathrm{LZK}}^{bb}}{\frac{\alpha_{\mathrm{LZK}}^b}{\alpha_0^a}C_6^{aa} + \frac{\alpha_0^a}{\alpha_{\mathrm{LZK}}^b}C_{6,\mathrm{LZK}}^{bb}} \tag{10}$$

where α_0^a and α_{LZK}^b denote the static polarizabilities of the adsorbate atom and the effective atom-in-a-solid system. Note that the LZK related parameters α_{LZK}^b and $C_{6,\mathrm{LZK}}^{bb}$ are independent of the adsorbate atom, namely they can be considered as intrinsic properties of bulk.

TS-based methods use the electron density-dependent quantity to describe the dispersion energy and adopt relatively less empirical parameters. Remarkably, the TS-based scheme holds for a large variety of systems with the relatively lower computational costs. TS-vdW is mainly suitable for molecular systems in a relatively small scale, such as noble-gas atoms and other small molecules [68], while SCS can effectively describe the large scale molecular systems and solid [71, 76], e.g. for understanding the point defects of semiconductors [77]. MBD has made great success in the multiple non-covalent bond systems [71, 72], which captures the dispersion interactions of conjugated aromatic molecules, heteroaromatic compounds [78, 79], biomolecules [80], high-pressure materials [81, 82], and variety nanostructures like graphite, hexagonal boron nitride and nanotubes [62, 83–86]. For adsorption, TSsurf method [75] is effective for describing the adsorption on metal-based substrates by considering the long-range screening effects [87] and the MBD method is powerful in characterizing the adsorption of nanomaterials where the many-body effects of vdW interactions are pronounced [84, 88].

Despite the great success of DFT, it usually describes the static process under 0 K and zero pressure, whereas atoms and molecules are always in movement affected by complex quantities such as temperature and pressure, which are crucial for realistic applications in surface science. The most widely used method to address this issue is *ab initial* molecular dynamics (AIMD) [89], which aims to simulate the dynamic process of molecules for describing the realistic physical picture of interactions. Combining DFT and molecular dynamics, AIMD replaces the semi-empirical effective potentials with the realistic physical potentials, of which the Car–Parrinello molecular dynamics [90] is one of the main methods to solve the AIMD. In Car–Parrinello molecular dynamics, the equations of motion of the electron ψ_i, nuclear R_I and external constrains α_{v} imposed on system such as volume and strain are expressed as,

$$\mu\ddot{\psi}_i(r,t) = -\frac{\delta E}{\delta\psi_i^*(r,t)} + \sum_{\mathrm{k}}\Lambda_{\mathrm{k}}\psi_{\mathrm{k}}(r,t) \tag{11}$$

$$M_I\ddot{R}_I = -\delta\Delta_{\mathrm{R_I}}E \tag{12}$$

$$\mu_v\ddot{\alpha}_v = -\frac{\delta E}{\delta\alpha_v} \tag{13}$$

where E is the potential energy of the system, M_I is the physical ionic masses, μ and μ_{v} are arbitrary parameters of appropriate units. Λ_{ik} is the Lagrange multipliers to maintain the constraints that $\int \mathrm{d}^3 r\psi_i^*(r,t)\,\psi_j(r,t) = \delta_{ij}$. If the velocities vary, the temperature of the system can be reduced and the potential energy E reaches minimum for $T \to 0$. AIMD provides an effective approach for describing the dynamic process and closing up the temperature and pressure gap, e.g. describing the isothermal and isobaric processes.

The effects of temperature and pressure can be also effectively captured with first-principles atomistic thermodynamics [91–95] for surface adsorption in gas phase condition by taking the chemical potentials of systems into account although still focusing on the static process. Scheffler *et al* [96, 97] demonstrate that the effects of temperature and pressure for $RuO_2(110)$ surface with O_2 and CO environment are directly related to the chemical potentials of gas phases, which can be easily obtained at any temperature and pressure by extrapolating from the conditions under 0 K and zero pressure. Hence, the equilibrium structure and reaction steps including the effects of temperature and pressure can be calculated in terms of first-principles atomistic thermodynamics.

2.2. COOP and frontier orbital theory

Hoffmann proposed the concept of COOP [98–100] to describe the bonding and antibonding contributions to the chemical bonds and Saillard and Hoffmann applied the frontier orbital theory to study the interactions during adsorption [101], thereby drawing an effective physical picture of bonding. When adsorption occurs on surface, partial bonds between adsorbate and surface atoms are formed while the bonds within adsorbate are weakened [102, 103]. Thus identifying the bonding properties upon adsorption is essential for understanding the mechanism of adsorption. Mulliken analysis [104] gives a mathematic understanding of bonding. For a two-center orbital,

$$\psi = c_1\phi_1 + c_2\phi_2 \tag{14}$$

then the normalized orbital is as follows,

$$\int |\psi|^2 \mathrm{d}\tau = 1 = c_1^2 + c_2^2 + 2c_1c_2S_{12} \tag{15}$$

Clearly, the overlap term $2c_1c_2S_{12}$ represents the bonding characteristics. The overlap integral S_{12} is usually taken as positive, so that $2c_1c_2S_{12}$ is positive for c_1 and c_2 with the same sigh, while negative for those with the opposite sigh. The magnitude of the overlap term $2c_1c_2S_{12}$ is the so-called Mulliken overlap population [104], which depends on c_1, c_2 and S_{12}. Hoffmann proposed an overlap population weighted density of states (DOS) to illustrate the bonding and antibonding contributions to the surface chemical bonds: COOP. Figure 1(a) is the schematic DOS and COOP curve of H-chain [105], where the positive and negative regions of COOP curve correspond to the bonding and antibonding respectively. The integral of the COOP up to the

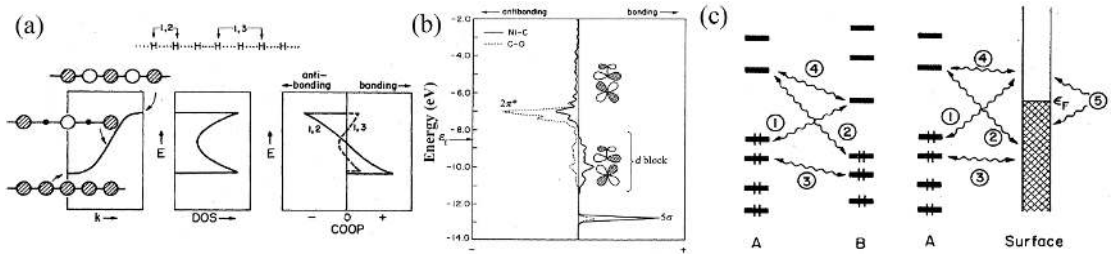

Figure 1. The bonding properties between atoms or molecules. (a) Schematic illustration of density of states (DOS) and crystal orbital overlap population (COOP) of hydrogen-chain. Reprinted figure with permission from [105], Copyright (1988) by the American Physical Society. (b) A typical COOP curve of CO adsorption on Ni(100) surface. Solid and dotted lines represent the Ni–C and C–O bonding properties [105]. (c) Schematic illustration of the interactions between the energy levels of molecules A and B and molecule A and solid surface [105]. Reprinted with permission from [105]. Copyright 1988 American Physical Society.

Fermi level corresponds to the total overlap population of the bond. Note that the strength of the COOP curve depends on the number of states, the magnitude of the coupling overlap and the size of the coefficients of orbitals. Taking CO adsorption on Ni(100) surface as an example, figure 1(b) plots the COOP curve for Ni–C bonding and C–O bonding [105]. It is evident that the 5σ orbital of CO and the *d*-band of Ni mainly contribute to the Ni–C bonding, while the $2\pi^*$–d_π interaction dominates the Ni–C and C–O antibonding above the Fermi level. The total overlap population is 0.84 for Ni–C bond and 1.04 for C–O bond, while is 1.21 for the free CO molecule. The weakening of the bond upon adsorption is mainly attributed to the population of $2\pi^*$ orbital.

A chemical interaction can be understood from the energy levels of the interacting atoms or molecules. Consider a simple pairwise interaction as shown in the left side of figure 1(c) [105], in which molecules A and B possess 4 and 6 electrons, respectively. Intuitively, there are three kinds of interactions between the individual energy levels of A and B: interaction ① (②), interaction ③ and interaction ④. Interaction ① (②) is a typical 2-electrons interaction and the stable true bond. Interaction ③ is a repulsive one since the antibonding state is filled with two electrons, leading to the increase of energy. Interaction ④ corresponds to no energy results due to the unoccupied energy levels. It is generally accepted that the highest occupied molecular orbital and the lowest unoccupied molecular orbital control the interactions between two molecules, which are called as the frontier orbitals [106]. The frontier orbitals are the valence states of molecules and are most easily affected by the interactions. Intriguingly, Hoffmann found that the two-orbital four-electron interaction (interaction ③ in the right side of figure 1(c)) and two-orbital zero-electron interaction (interaction ④ in the right side of figure 1(c)) between molecule and surface can also form bonding although the interactions ① and ② still dominate the adsorption properties [105], which is different from the bonding between molecules. This is attributed to the fact that the electrons of antibonding state in interaction ③ transfer to the states of surface atoms and the bonding state in interaction ④ is filled with electrons donated by the surface atoms, stabilizing the interactions ③ and ④ and improving the bonding of adsorption. Interaction ⑤ occurs between surface atoms, which is the second-order energetic and reflects the bonding consequences of shifts of electron density around the Fermi level.

2.3. Effective medium theory

It could be very complex to calculate the energies of adsorption systems, especially for those with low symmetry. Hence, finding a simple way, for instance, a reasonable approximation to determine the energy of an adsorption system seems to be meaningful. EMT [107] has offered a far-reaching solution to this issue, and its basic idea is to replace the inhomogeneous environment of host with the homogeneous electron gas. The binding energy of a homogenous adsorption system is a function of the electron gas density as $\Delta E^{\mathrm{hom}}(\rho)$. If one introduces a perturbation that changes the density of homogeneous electron gas $\overline{\rho}$ to that of inhomogeneous system as $\rho(r) = \overline{\rho} + \delta\rho(r)$, then the change in $\Delta E^{\mathrm{hom}}(\rho)$ should be as [108],

$$\delta\Delta E = \int [\Delta\rho(r) - Z\delta(r)]\,\delta v(r)\,\mathrm{d}r + \frac{1}{2}\int \delta\Delta\rho(r)\,\delta v(r)\,\mathrm{d}r \tag{16}$$

where δ and Δ represent the perturbation-induced changes and atom-induced changes respectively. Z is the charge of adsorption atom. $\Delta\rho = \rho(\mathrm{r}) - \rho_0$ is the difference between the density of adsorption system and the substrates alone. $\delta v(r)$ is the difference between the potential due to the positive background and the

potential due to the ion cores of the bounded substrate. Now one chooses the average electron density $\overline{\rho}$ such that

$$\int \Delta\phi(r)\delta\rho \mathrm{d}r = \int \Delta\phi(r)[\rho - \bar{\rho}]\mathrm{d}r = 0 \tag{17}$$

where $\Delta\phi$ is the atom-induced electrostatic potential in homogeneous substrates. Hence, the zero-order, first-order and second-order term of equation (16) are as follows,

$$\Delta E^{(0)} = \Delta E^{\mathrm{hom}}(\rho) \tag{18}$$

$$\Delta E^{(1)} = \int [\Delta\rho(r) - Z\delta(r)]\phi_0(r)\,\mathrm{d}r \tag{19}$$

$$\Delta E^{(2)} = \frac{1}{2}\iint [R(r,r') - R'(r',r)]\phi_0(r)\,\delta\rho(r')\,\mathrm{d}r\mathrm{d}r' \tag{20}$$

where $\phi_0(r)$ is the electrostatic potential of substrates, R and R' are the parameters related to the static polarizabilities P and P_0 and the dielectric functions ε and ε_0 of the homogenous electron gas with and without adsorbed atom. Note that the second-order term (including equation (20)) needs to be taken into account only when the adsorbate-induced resonance state is close to the Fermi level such as Li and Si that are particularly polarizable. While in most cases, the first-order approximation, namely equations (18) and (19) are accurate enough to describe the energy of adsorption systems as long as the resonance state is well below the Fermi level such as the electronegative adsorbates hydrogen and oxygen that are not particularly polarizable. EMT has profound significance to understand adsorption and has been utilized to explain the mechanism of the LSR [32, 33] and the intrinsic model [34].

2.4. Electronic models

Adsorption on a surface gives rise to the interaction between the valence states of adsorbates and surface atoms, which involves a study of electronic properties of materials. Over the past decades, several electronic models have been proposed for elucidating the roles of electronic structures in adsorption. In the following, we will introduce the electronic models and descriptors which are suitable for different kinds of materials such as pure TMs, NSAs, TM oxides and SACs.

2.4.1. News-Anderson model for adsorption

Adsorption occurs when the distance between an adsorbate (an atom or molecule) and surface atoms is getting closer, along with the states of adsorbates coupling with all the valence states of surface atoms. This coupling can be illustrated by the News-Anderson (NA) model [109, 110]. Here we take TMs as example to explicit the interaction between adsorbates and the different valence states of TM. Figure 2(a) illustrates a typical DOS of a given TM [5]. Clearly, a TM's states include a broad *s*-band and a narrow *d*-band, the latter is caused by the small coupling matrix strength between the localized *d*-states of TM (V_{dd}), namely the strength of V_{dd} is proportional to the bandwidth. When an adsorbate interacts with the *s*-states of TM, only a single resonance state is generated below the energy of the original adsorbate state. In contrast, the interaction between an adsorbate state and *d*-states of TM gives rise to the split-off bonding and antibonding states which locate below and above the original adsorbate state respectively as seen in figure 2(b) [5].

According to the NA model, adsorption on surfaces can be considered as a two-step process. At first, the valence state of a given adsorbate interacts with the metal *s*-state, generating a resonance state below the original valence state of adsorbate called renormalized state. Then the renormalized state couples with *d*-states of TMs. Since the *d*-band is narrow, this interaction gives rise to the state splitting: a bonding state and an antibonding state, which are below and above the renormalized state respectively. This two-step process is well illustrated in figure 2(c) [5]. Therefore, adsorption energy can be expressed as,

$$\Delta E = \Delta E_{\mathrm{a-s}} + \Delta E_{\mathrm{a-d}} \tag{21}$$

where $\Delta E_{\mathrm{a-s}}$ and $\Delta E_{\mathrm{a-d}}$ are the energy of renormalized state (adsorbates-*s* hybrid state) and adsorbates-*d* hybrid state. It is noteworthy that all TMs have similar half-filled *s*-band. Thus $\Delta E_{\mathrm{a-s}}$ for all TMs could be considered as a constant, which means that the variation of adsorption energy from one metal to the next is dominated by the interaction between the renormalized state and metal *d*-state $\Delta E_{\mathrm{a-d}}$. When the strength of $\Delta E_{\mathrm{a-d}}$ is weak, adsorption energy only depends on the position of the *d*-states relative to the Fermi level to a

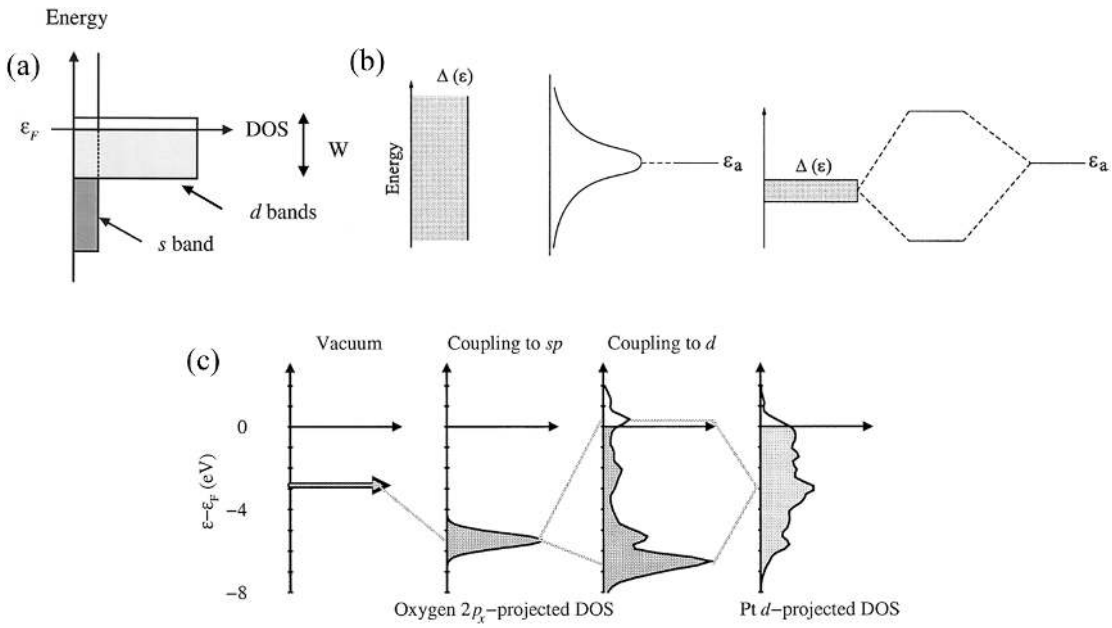

Figure 2. The coupling between adsorbates and surface atoms. (a) Schematic illustration of density of states (DOS) of transition metals (TMs). (b) Schematic illustration of the valence states of adsorbates coupling with the *sp*-states and *d*-states of TMs. (c) Schematic illustration of the two-step process of the coupling between adsorbates and TM atoms. Reprinted from [5], Copyright (2000), with permission from Elsevier.

first approximation, which is exactly the essential of the *d*-band model [5, 8, 9]. $\Delta E_{\mathrm{a-d}}$ can be quantitatively estimated by the NA model as [111],

$$\Delta E_{\mathrm{a-d}} = \frac{2}{\pi}\int_{-\infty}^{0} \mathrm{Arc\ tan}\left(\frac{\Delta(\varepsilon)}{\varepsilon - \varepsilon_{\mathrm{a}} - \Lambda(\varepsilon)}\right)\mathrm{d}\varepsilon - n_{\mathrm{a}}\varepsilon_{\mathrm{a}} \tag{22}$$

n_{a} and ε_{a} are the degeneracy and energy of the adsorbate energy level. $\Delta(\varepsilon) = \sum_{\mathrm{k}} |V_{\mathrm{ad}}|^2 \delta(\varepsilon - \varepsilon_{\mathrm{k}})$ and its transform version $\Lambda(\varepsilon) = \frac{1}{\pi} P \int_{-\infty}^{\infty} \frac{\Delta(\varepsilon')}{(\varepsilon - \varepsilon')}\mathrm{d}\varepsilon'$ are the adsorbate-induced changes to the metal states multiple the coupling between the adsorbate and metal states (P is the principal value of the integral for the transform). The coupling matrix element V_{ad}, which is strongly dependent on the spatial extent of metal *d*-states, can be expressed based on the bandwidth and elemental radius [112]:

$$V_{ad}^2 = \eta \frac{M_a M_d}{r^{l_a + l_d + 1}} \tag{23}$$

where η is a structure constant in LMTO, and l_i ($i = a, d$) is the angular momentum quantum number of adsorbate and metal. In $M_l = \sqrt{s^{2l_i+1}}\Delta_{l_i}$, s is the neutral sphere radius and Δl_i is a LMTO potential with respect to the bandwidth. Equation (22) can be applied to DOS distribution to obtain the interaction energy between the particular DOS distribution and an adsorbate level [112].

2.4.2. Electronic model for TMs:d-band center

d-band model [5, 8, 9], one of the most successful electronic models, has severed as a basis to clarify the mechanism of adsorption, which is proposed initially for TM surfaces especially for the late TMs. This model demonstrates that it is the *d*-states of TMs that determine the variation of adsorption energy from one TM to the next, namely the adsorption energy on TMs is controlled by the position of *d*-states relative to the Fermi level. In this section, we will make use of the *d*-band model to elaborate the materials-dependent effects, the coverage effects and strain effects of adsorption.

Table 1. The first (ε_d) and second moments ($m^c_{n=2}$) of the semi-empirical fits to the DFT-calculated density of states (DOS) and the coupling matrix element V^2_{ad} relative to Cu for 24 transition metals (TMs). The data are extracted from [112].

TMs	ε_d (eV)	$m^c_{n=2}$ (eV)	V^2_{ad}
Sc(0001)	1.18	2.19	7.9
Ti(0001)	0.7	3.05	4.65
V(110)	0.38	3.77	3.15
Cr(110)	−0.35	3.85	2.35
Fe(110)	−0.84	2.39	1.59
Co(0001)	−1.5	2.32	1.34
Ni(111)	−1.59	1.39	1.16
Cu(111)	−2.46	0.84	1
Y(0001)	1.14	4.33	17.3
Zr(0001)	0.72	5.22	10.9
Nb(110)	0.1	5.64	7.73
Mo(110)	−0.9	5.36	6.62
Ru(0001)	−1.95	4.3	3.87
Rh(111)	−2.1	3.44	3.32
Pd(111)	−1.78	1.27	2.78
Ag(111)	−4.04	0.75	2.26
Hf(0001)	0.66	6.99	11.9
Ta(110)	0.29	8.32	9.05
W(110)	−0.77	8.71	7.72
Re(0001)	−1.58	8.18	6.04
Os(0001)	−2.23	6.21	5.13
Ir(111)	−2.95	4.97	4.45
Pt(111)	−2.42	2.65	3.9
Au(111)	−3.36	1.61	3.35

2.4.2.1. Materials-dependent effects for atomic adsorbates

The first moment of the electronic DOS distribution $\rho(x)$, ε_d, namely the center of *d*-band, and the *n*th moments m^c_n of $\rho(x)$ centered at ε_d are defined as,

$$\varepsilon_d = \frac{\int_{-\infty}^{\infty} x\rho(x)\,dx}{\int_{-\infty}^{\infty} \rho(x)\,dx} \tag{24}$$

$$m^c_n = \frac{\int_{-\infty}^{\infty} (x-\varepsilon_d)^n \rho(x)\,dx}{\int_{-\infty}^{\infty} \rho(x)\,dx} \tag{25}$$

Note that another crucial electronic property, the *d*-band width of TM W_d, is defined as $W_d = 4\sqrt{m^c_2}$. Vojvodic *et al* [112] demonstrate that the semi-empirical fits to the DFT-calculated DOS are effective in representing the *d*-band properties of TMs. Table 1 summarizes the first and second moments of the semi-empirical fits to the DFT-calculated DOS and the coupling matrix element V^2_{ad} relative to Cu for 24 TMs.

A more simplified expression of ΔE_{a-d} can be obtained by assuming that both the renormalized adsorbate state and the partially filled metal *d*-band can be approximated by single energy levels ε_a and ε_d as [113],

$$\Delta E_{a-d} = -\alpha \frac{V^2_{ad}}{|\varepsilon_d - \varepsilon_a|} + \beta V^2_{ad} \tag{26}$$

Here α and β involve the information of *d*-band fillings, the level degeneracy, and the spatial extent of the adsorbate level state. The first term represents the attractive interaction between the adsorbate and metal *d*-states and the second term denotes the Pauli repulsion due to the orthogonal overlapping of states. According to equation (26), one can easily obtain that there exist three main factors that control the adsorption of TMs and can serve as the basic electronic descriptors: *d*-band center ε_d, *d*-band width W_d and *d*-band filling. Note that these three factors are related with each other. For instance, the variation of W_d

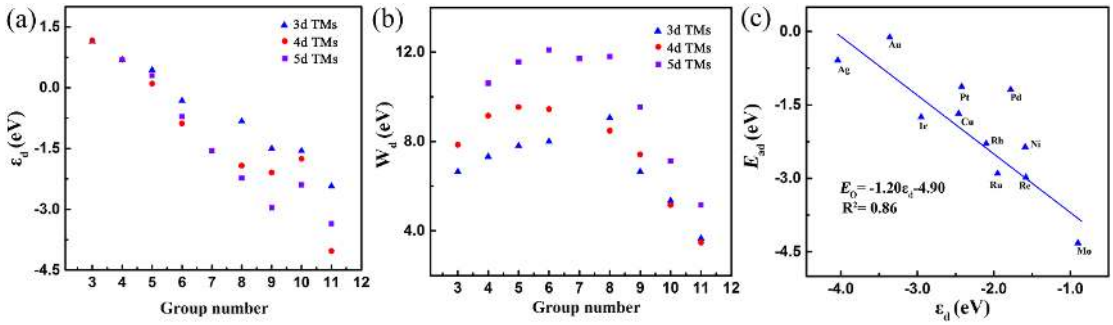

Figure 3. The *d*-band descriptors of adsorption energy. (a), (b) The *d*-band center ε_d and *d*-band width W_d versus group numbers (or the valence electrons) for 3*d*, 4*d* and 5*d* transition metals (TMs). (c) The adsorption energies of O versus ε_d for the late TMs. The data are adapted from [112].

generates the movement of ε_d in order to maintain the constant *d*-band filling. Figures 3(a) and (b) plot the calculated ε_d and W_d for 27 TMs against the group numbers or the number of valence electrons [112]. Clearly, ε_d shows a linear relation with group numbers except the outliers Ni, Pd and Pt, while W_d exhibits a broken-line correlation with group numbers. Both ε_d and W_d decrease with increasing group number for the late TMs while ε_d and W_d show opposite trends with group numbers for the early TMs.

Figure 3(c) plots the adsorption energies of O for the late TMs as a function of the *d*-band center ε_d [112]. Clearly, the adsorption energies correlate well with ε_d except the outlier Pd and Pt, which demonstrates that ε_d is indeed a good descriptor in understanding the trends of adsorption of oxygen. This corresponds to the classical *d*-band theory that has been widely used to understand the materials-dependent effects of adsorption.

There exist two main effects as shown in figure 3(c): (a) the adsorption strength decreases from the left of periodical table to the right and (b) the further down the periodical table, the weaker the adsorption energy. To understand the mechanism of these two effects, one needs to uncover the roles of *d*-states for different TMs. The *d*-states of metals increasingly move downward from the left of periodical table to the right as the *d*-band filling increases, finally all *d*-bands are occupied and are well below the Fermi level. This means that the antibonding states are gradually filled from the left to the right of periodical table and there are no empty antibonding states for Cu, Ag and Au. Therefore, the further to the right of periodical table, the weaker the attraction interactions and finally turning to the repulsive interactions, leading to the decreasing adsorption strength. In addition, the states of two atoms will be orthogonal to each other when the states overlap, which gives rise to the Pauli repulsion. The strength of Pauli repulsion for adsorption is proportional to the square of the coupling matrix element V_{ad}^2 (see equation (26)). For a given adsorbate and a fixed adsorbate geometry, the strength of V_{ad} only depends on the metal *d*-states (see equation (23)). Since the *d*-bands are well below the Fermi level for TMs with essentially filled *d*-states, it is the Pauli repulsion that determines the variation of adsorption energy. V_{ad}^2 increases down through the groups of the periodical table, rendering the fact that the repulsive interaction of TMs obeys the order that $5d > 4d > 3d$ metals. Hence, Au is the noblest metal [8]. It should be mentioned that both the attractive and repulsive interactions increase with increasing coupling matrix element (see equation (26)), and it is the competition between attraction and repulsion that determines the net results of coupling strength of adsorbate-*d* hybrid states.

As ε_d gives a good description of O adsorption energy for the late TMs despite the other factors that matter to the variation of adsorption energy such as W_d, we now discuss this origin. Actually, for the late TMs, ε_d and W_d are independent of each other. The hybridization energies (ΔE_{a-d}) are dominated by ε_d while depend weakly on W_d for the late TMs [112]. The case for the early TMs is different from that for the late TMs, which we will discuss in section 2.4.2.5.

2.4.2.2. Materials-dependent effects for molecular adsorbates

Molecular adsorbates on TM surfaces obey the same rule as atomic adsorbates, while the former's mechanism is more complicated. First, taking the H_2 molecule adsorbed on TM surfaces as an example [8, 9], the two *s*-states of H_2 overlap to generate bonding state σ_g and antibonding state σ_u^* as shown in figure 4(a) [9]. When the adsorption occurs, both the σ_g and σ_u^* couple with the metal *s*-states, leading to the two corresponding broad resonance states below the original σ_g and σ_u^* states. After that, the two renormalized states interact with the narrow *d*-band of TMs and split into bonding and antibonding states seen in figure 4(a). Since the two bonding states $\sigma_g - d$ and $\sigma_u^* - d$ are well below the Fermi level, it is the two

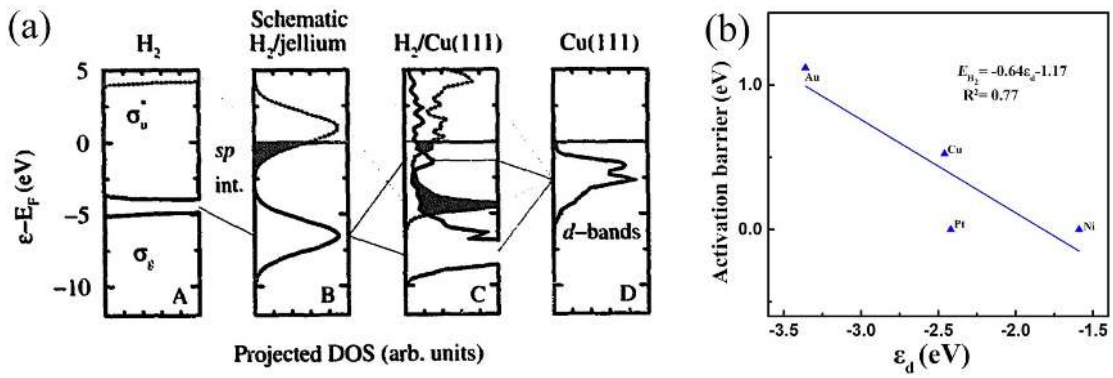

Figure 4. The coupling between the valence states of molecular adsorbates H_2 and transition metals (TMs). (a) The two-step process of the coupling between H_2 and metals. Reprinted from [9], Copyright (1995), with permission from Elsevier. (b) The activation barrier for H_2 dissociation on (111) surfaces of Au, Cu, Pt and Ni versus the *d*-band center ε_d. The data are adapted from [8].

corresponding antibonding states $(\sigma_g{-}d)^*$ and $(\sigma_u{}^*{-}d)^*$ that control the coupling strength with metal *d*-band.

Figure 4(b) shows that the activation barriers of four TMs (Ni, Pt, Cu and Au) exhibit a linear relation with the *d*-band center ε_d except the outlier Pt, making ε_d a good descriptor for the materials-dependent effects of H_2 adsorption [8]. It is clear that the activation barrier of H_2 dissociation varies for different TMs in the order Au > Cu > Pt = Ni, while the dissociation of H_2 on the latter two surfaces occurs spontaneously. This order can be explained by the *d*-band model. All the $(\sigma_u{}^*{-}d)^*$ states locate well above the Fermi level, leading to the large attraction. The position of $(\sigma_g{-}d)^*$ states varies from one TM to the next, namely the antibonding states are just above the Fermi level for Ni and Pt but are well below the Fermi level for Au and Cu [8]. Hence, there exists attractive interaction on Ni and Pt surfaces and repulsive interaction on Au and Cu surfaces towards H_2 caused by the $(\sigma_g{-}d)^*$ states. Since 5*d* metals have larger coupling matrix element than 3*d* metals, the stronger repulsion of Au than Cu makes Au exhibit the largest activation barrier seen in figure 4(b). In fact, the bonding between the H atom and Au is not weak at all due to the fact that the large attraction attributed to the coupling with the metal *s*-states is only partially compensated by the repulsion with *d*-bands. However, comparing with the bonding in H_2 molecule, the bond is only marginally stable for Cu and totally unstable for Au [8]. It is noteworthy that Cu and Pt hold the similar ε_d (−2.42 eV for Pt and −2.46 eV for Cu) while the activation barriers of H_2 dissociation vary a lot (see figure 4(b)). This is due to the different *d*-band filling (0.9 for Pt and 1.0 for Cu) and *d*-band width W_d (6.51 eV for Pt and 3.66 eV for Cu) [112] for Pt and Cu, which are also important in determining adsorption (see equation (26)). The larger W_d and less-filled *d*-band filling of Pt make the antibonding state $(\sigma_g{-}d)^*$ is just above the Fermi level, while the $(\sigma_g{-}d)^*$ state of Cu locates below the Fermi level [8, 114]. Hence, the empty $(\sigma_g{-}d)^*$ state of Pt and the filled $(\sigma_g{-}d)^*$ state of Cu lead to the attractive and repulsive interaction respectively, accounting for the different activity for the H_2 dissociation.

Then we discuss the adsorption of CO. The correlation between the adsorption energy of CO for TMs and the *d*-band center ε_d is illustrated in figure 5(a) [34], where the linear correlation indicates that ε_d serves as a good descriptor in describing the materials-dependent nature of CO adsorption. The widely accepted Blyholder model [106, 115] implies that it is the 5σ and $2\pi^*$ states of CO determine the adsorption. Similar to H_2, the 5σ and $2\pi^*$ states of CO couple with metal *s*-states firstly and then interact with *d*-states of TMs, leading to the split-off bonding and antibonding states seen in figure 5(b) [5]. One important effect from figure 5(b) is that the 5σ state of CO plays a minor role in the strength of adsorption compared with $2\pi^*$ state due to the fact that there are only few empty antibonding states of 5σ state and all the antibonding states of $2\pi^*$ state are well above the Fermi level. Hence, $2\pi^*$ interaction dominates the variation from one TM to the next. Moreover, from the view of symmetry, the highly directional 5σ state plays more vital roles for atop adsorption while the $2\pi^*$ state of CO is dominant for hollow sites adsorption [116, 117].

2.4.2.3. The interaction between adsorbates

What we discussed above is the adsorption of a single atom or molecule, neglecting the interaction between adsorbates, namely the coverage effects of adsorbates, which is crucial in practical applications. Generally, both the attractive and repulsive interactions can exist between adsorbates. The former is often due to the surface reconstruction and leads to island formation and clustering, while the repulsive interaction is the most common situation and results in separated overlayers [118–120]. Here one introduces the two main

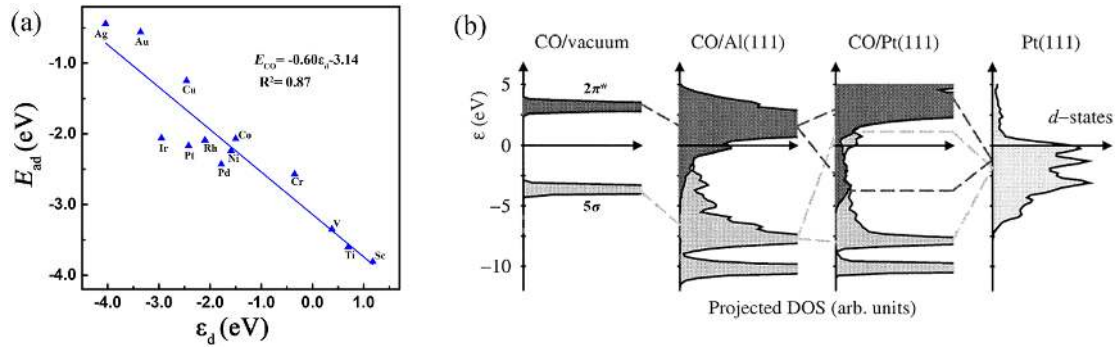

Figure 5. The coupling between the valence states of molecular adsorbates CO and transition metals (TMs). (a) The adsorption energies of CO on TMs versus the *d*-band center ε_d. The data are adapted from [34]. (b) The two-step process of the coupling between CO and metals. Reprinted figure with permission from [115], Copyright (1996) American Physical Society.

effects between adsorbates. One is the direct interaction which is caused by the overlaps of the valence states between adsorbates. If the valence states are close enough to the Fermi level so that the interaction may shift the states through the Fermi level, the attractive interaction will be generated. Otherwise, in more cases this direct interaction is dominated by the Pauli repulsion [5]. The other is the indirect interaction between adsorbates. Adsorption on surface changes the electronic structure of surface atoms, thereby affecting the coupling between another adsorbate (an atom or molecule) and surface atoms. It is normally considered that adsorption gives rise to the downshift of *d*-states of neighboring surface atoms [121, 122], namely the antibonding states are less empty and the attractive interaction is weakened. Therefore, the bonding between the second adsorbate and surface atoms may not be as strong as the first one.

2.4.2.4. Electronic model for strain effects

Strain effects are common phenomena in catalysis and are widely used to create numerous intriguing properties different from that of strain-free status [123], which can occur either externally by applying mechanical loading or internally by creating the lattice mismatch of surface layers (substituting surface atom with another one of different atomic radius or creating heterogeneous overlayers on surfaces such as alloying). Actually, strain effects are complicated and depend on numerous properties, such as the species of adsorbates and substrates, surface orientations, adsorption sites, and the intensity and direction of strain [124–131]. Both the *d*-band model [132] and the generalized coordination number model [133] can provide a partial explanation for strain effects. In this section, we focus on the electronic effects of strain, while the geometric effects of strain are discussed in section 2.5.3.

When a surface is subject to tensile or compressive strain, the electronic structures in particular the *d*-bands of TMs vary a lot. Tensile (compressive) strain on surface leads to the increasing (decreasing) atomic distances and decreasing (increasing) overlaps of *d*-states. Consequently, the width of *d*-band decreases (increases) as well. It is a general finding that there is no charge transfer under strain, which means that the *d*-band of metals would shift upward or downward to maintain a constant filling. Hence, compressive and tensile strain generate downshift and upshift of *d*-band [132]. These effects are explicitly illustrated in figure 6(a). Moreover, strain effects also depend on the adsorption sites which cannot be well clarified by the *d*-band model [134].

Figure 6(b) shows the adsorption energy of CO and O as a function of strain (lattice constants) and *d*-band center ε_d [132]. Clearly, the strength of adsorption enhances with increasing strain (the larger (smaller) lattice constant corresponds to the larger tensile (compressive) strain), which could be well understood by the *d*-band model as discussed above. From compressive strain to tensile strain, *d*-band moves to higher energy position, making the antibonding states coupled by adsorbate and metal *d*-states more likely be pushed above the Fermi level. Therefore, the larger the strain, the larger the net attractive interaction and the stronger the adsorption energy. As the shift of *d*-band can be well described by the center of *d*-band ε_d, ε_d is thus a good descriptor to characterize the trends of strain seen in figure 6(b).

Moreover, the strain effects are strongly related to the adsorption sites, namely the different sites may correspond to the different responses of substrates to strain. Figure 6(c) shows the calculated CH_2 binding energy to Cu(110) surface under biaxial strain [134]. For the bridge-site adsorption, the tensile strain makes the binding stronger, whereas the compressive strain accounts for the enhancement of binding strength at four-fold hollow site. This opposite trend generates a crossover of optimal adsorption sites as a function of strain shown in figure 6(c). This conflicting observation cannot be simply explained by the *d*-band model.

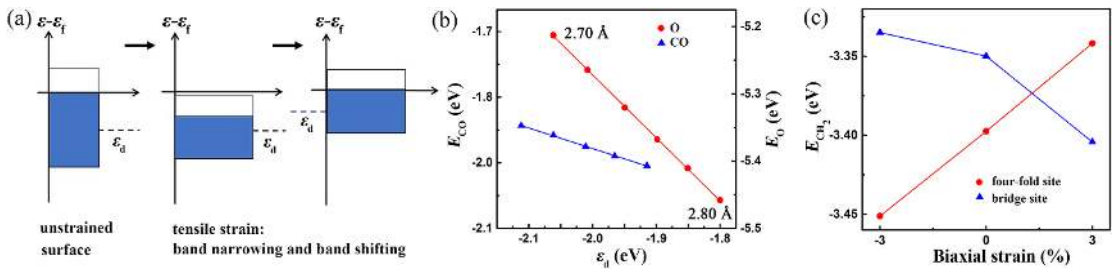

Figure 6. The electronic properties of strain effects. (a) The illustration of the effect of tensile strain on the *d*-band of transition metals (TMs). (b) The adsorption energies of CO and O under strain versus the *d*-band center ε_d on Ru(0001) surface. The data are adapted from [132]. (c) The binding energy of CH_2 on Cu(110) surface versus strain at bridge sites and four-fold sites. The data are adapted from [134].

Actually, it is the different response to strain of these two sites that control the variation tendency of binding energy. The fundamental difference between bridge and four-fold sites is that the neighboring metal atoms are put outward at bridge sites but are put inward at four-fold sites [134]. Therefore, the bridge-site adsorption feels the tensile strain to stabilize the interaction between adsorbate and surface atoms, on the contrary, the compressive strain is helpful to enhance the interaction at four-fold site.

2.4.2.5. Electronic model with the upper-edge of d*-bands*

It is noteworthy that the *d*-band center ε_d can provide a good description of the adsorption energy only for the late TMs [5, 8, 9]. This is due to the different contributions of ε_d and W_d to the adsorption energy for the late and early TMs: ε_d dominantly determines the adsorption energy for the late TMs while both ε_d and W_d contribute to the adsorption energy for the early TMs [112]. Therefore, a refined descriptor that contains both the contributions of ε_d and W_d is needed.

Vojvodic *et al* [112] find that the position of the upper-edge of the *d*-band shifts downwards as the center of *d*-band shifts down for 4*d*-series TMs. This implies that the upper-edge of the *d*-band is also an important quantity that varies from one TM to the next. Actually, bond strength strongly depends on the position and filling of antibonding states, which are pinned at the upper-edge of *d*-bands, thus it is reasonable to put forward a refined descriptor $\varepsilon_d + W_d/2$ to introduce a *d*-band width dependent term, ensuing the correlation between the position of the upper-edge of the *d*-band and the binding strength. As seen in figure 7, $\varepsilon_d + W_d/2$ describes the trends of adsorption energy well including the above outliers Pd and Pt [112]. Unfortunately, this refined descriptor is unable to rationalize the trends of TMs with completely filled *d*-bands such as Cu and Ag, which is due to the fact that the position of *d*-band for these metals is no longer pinned to the Fermi level.

2.4.3. Electronic model for NSAs

It has been verified both theoretically and experimentally that introducing guest atoms into the subsurface layer of a host to form NSAs can change the electronic properties of atoms on top surface layer [20, 135–137], thereby modulating the numerous properties such as adsorption and catalytic activity. Koper *et al* [138] find that the number of valence electrons for adsorption systems (which are the valence electrons of Pt, the guest atom in the second layer and the adsorbate) provides a good description for the variations of adsorption energy on Pt@M(111) NSAs (M represents the guest atom in subsurface layer from 3*d*, 4*d* and 5*d* TMs) seen in figures 8(a)–(c). One of the most remarkable features of figures 8(a)–(c) is that the minimum of adsorption energies in all cases locates at the total number of valence electrons 24: the minimum is 10 for C and Si (corresponding to Ni, Pd and Pt), 9 for N and P (corresponding to Co, Rh and Ir), and 8 for O and S (corresponding to Fe, Ru and Os). The underlying mechanism of the constant total minimum valence electrons can be understood by the electron-counting rules to form a noble-gas-like electron cloud, following the 8-electrons and 18-electrons for adsorbate and surface atoms respectively [139, 140]. Therefore, one obtains that adsorption energies on NSAs are strongly correlated to the number of valence electrons from top surface layer atoms, subsurface layer atoms and adsorbates. Moreover, the constant total valence numbers of minimum adsorption energy make it possible to predict the adsorption energies of other NSAs such as the NSAs of Au.

Linic *et al* [141] make use of the *d*-band model to elucidate the trends of adsorption energies on Pt@M(111) NSAs for 3*d* series TMs. Since the distance between the Pt host and the guest atom is similar for all 3*d*-series TMs, namely the geometry of Pt@M(111) NSAs is dominated by the contributions of *sp*-states of TMs, which are approximated as constant for all TMs. Hence, the *d*-band width projected on geometrically

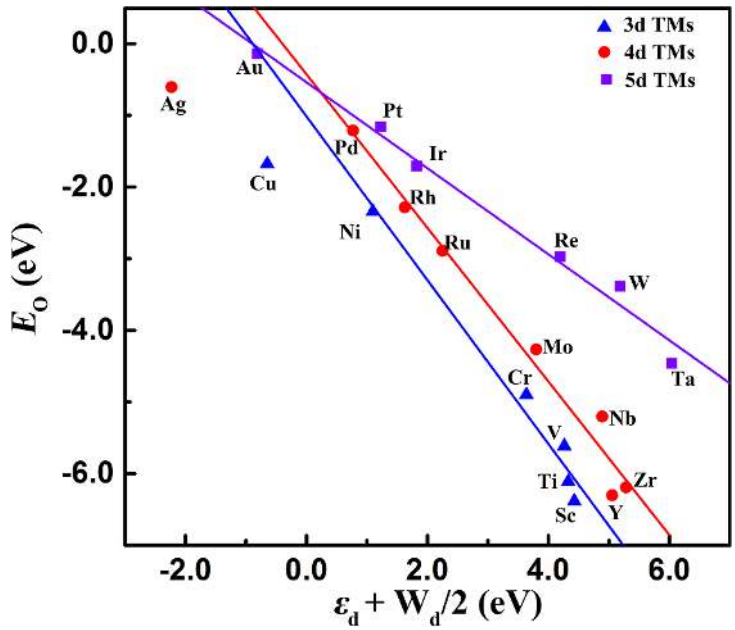

Figure 7. The adsorption energies of O versus the upper-edge of *d*-bands $\varepsilon_d + W_d/2$ for 20 transition metals (TMs). The data are adapted from [112].

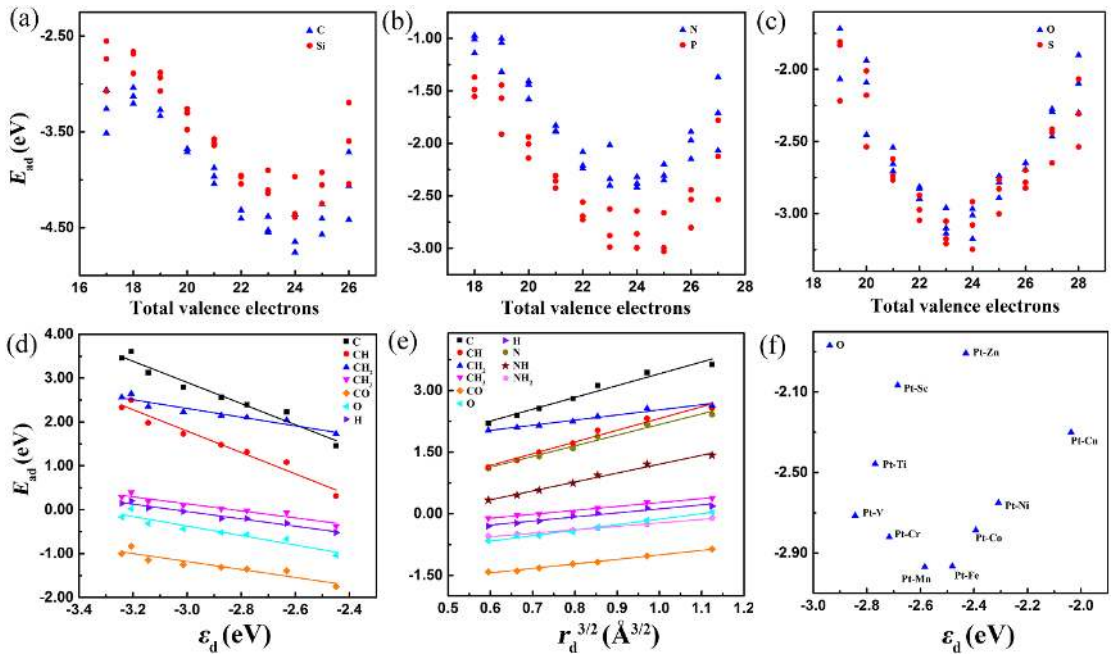

Figure 8. Electronic models for near-surface alloys (NSAs). (a)–(c) The adsorption energies of C, Si (a), N, P (b), O and S (c) versus the total valence electrons of systems for Pt@M(111) NSAs. The data are adapted from [138]. (d) The adsorption energies of CH_x ($x = 0, 1, 2, 3$), CO, O and H versus the *d*-band center ε_d for Pt@M(111) NSAs. (e) The adsorption energies of CH_x ($x = 0, 1, 2, 3$), NH_x ($x = 0, 1, 2$), CO, O and H versus the characteristic orbital length $r_d^{3/2}$ for Pt@M(111) NSAs. The data are adapted from [141]. (f) The adsorption energies of O versus ε_d for Pt@M(111) NSAs. The data are adapted from [138].

similar Pt sites should only be a function of the spatial extent of the *d*-states (r_d) of the 3*d*-metals directly coupling to the Pt host. Figures 8(d) and (e) exhibit the adsorption energies on NSAs as a function of *d*-band center ε_d and r_d, where the linear scaling behaviors exist [141]. The 3/2 power-dependent term between adsorption energies and r_d can be explained by tight-bonding (TB) approximation [142–144] in which the coupling matrix element V_{ad} is proportional to $r_d^{3/2}$.

Figure 8(f) exhibits the adsorption energies of O on atop sites of Pt@M(111) NSAs against ε_d of Pt skin [138]. Clearly, ε_d cannot provide a satisfying description for the adsorption energies of O on NSAs. Moreover, the variations from Pt-Sc to Pt-V and from Pt-Mn to Pt-Cu are conflicted with the predictions by

the *d*-band model where the increase of ε_d corresponds to the improvement of binding strength, namely the *d*-band model is ineffective in this case.

2.4.4. Electronic model for transition-metal oxides

TM oxides have attracted extensive attention and been applied to numerous fields due to the high catalytic activity, inexpensiveness, versatility and stability [145–148]. They are expected to reduce or completely replace the utilization of noble metals in many fields such as catalysis, fuel cells and metal-air batteries [149–151]. Hence, it is crucial to develop proper models to elucidate the trends of adsorption energy for TM oxides. Calle-Vallejo *et al* [152] demonstrate that the outer electrons (N_{oe}) which are defined as the number of remaining valence electrons of the metal atom upon oxidation can describe the variation of adsorption energies for species of O, OH and OOH on monoxides (MO) and perovskite oxides (ABO_3) (100) surfaces.

Taking Cr as an example, N_{oe} is equal to 6 for pure Cr, 4 for Cr^{2+} in CrO, 3 for Cr^{3+} in $LaCrO_3$ and 2 for Cr^{4+} in $SrCrO_3$. Figures 9(a)–(c) illustrates the linear relation between the adsorption energies and N_{oe} on MO and ABO_3 [152]. Clearly, the slopes of linear relation for OH and OOH are almost identical in all cases while the slope for O is about twice than that for OH and OOH seen in figures 9(a)–(c). One can easily obtain that the adsorption energies are weakened with the increasing N_{oe} despite the different species and surface structures. Note that different TM oxides share the same coordination and spatial distribution although their oxidation states are different. The e_g and t_{2g} orbitals are normally nonbonding or antibonding states while the O 2*p*-orbitals are bonding states, therefore, the increase of N_{oe} gives rise to the reductions in empty antibonding states and the weakening of adsorption energies. The outliers deviating from the guiding lines shown in figures 9(a)–(c) such as CaO, $LaScO_3$, $YScO_3$, $SrTiO_3$, $CaTiO_3$ and $BaTiO_3$ are attributed to fulfilling the octet or 18-electrons rules.

The *p*-band center of O or the average O 2*p*-state energy is initially proposed by Kitchin *et al* [153] to explain the adsorption energy of O for six 3*d*-series TMs and their rock-salt oxides. Subsequently, Nørskov *et al* [154] demonstrate that the average O 2*p*-state energy ($\bar{\varepsilon}_{2p}$) can serve as a descriptor to clarify the variation of $E_O - E_{OH}$ on face-centered cubic (fcc) metals (111), rutile oxides (110) and perovskite oxides (100) surfaces [155] ($E_O - E_{OH}$ implies that H atom is adsorbed on O atom rather than metal atom and is thus indicative of the reactivity of O atom). $\bar{\varepsilon}_{2p}$ can be expressed as the first moment of the DOS projected onto the atomic 2*p*-states of an adsorbed oxygen atom (after deprotonation) relative to the Fermi level:

$$\bar{\varepsilon}_{2p} = \frac{\int_{\varepsilon\,\min}^{\varepsilon\,\max} \rho_{2p}\varepsilon \mathrm{d}\varepsilon}{\int_{\varepsilon\,\min}^{\varepsilon\,\max} \rho_{2p}\varepsilon \mathrm{d}\varepsilon} \tag{27}$$

where ε_{min} and ε_{max} are chosen to −10 eV and 2 eV respectively. Figures 9(d)–(f) exhibits that $E_O - E_{OH}$ is strongly linearly correlated to $\bar{\varepsilon}_{2p}$ with the slope close to unity except the case of fcc(111), suggesting that the variation of $\bar{\varepsilon}_{2p}$ directly corresponds to that of $E_O - E_{OH}$. The linear relation implies that the higher-lying 2*p*-states lead to the weakening of adsorption energy, which is different from the *d*-band theory [5, 8, 9] that the upshift of *d*-bands gives rise to the receding adsorption strength. Note that $\bar{\varepsilon}_{2p}$ depends on the calculation of DOS, leading to the cost and qualitative results which is similar to the *d*-band model.

2.4.5. Electronic model for SACs

As the smallest size metal catalysts, SACs represent the study frontier in catalysis [156–166]. SACs can furthest improve the metal utilization with well-defined and atomically dispersed metal sites on supports. Moreover, as ideal and simplified models, SACs are beneficial to make a direct comparison between experiments and theoretical calculations [167]. Thus, understanding the physical and chemical nature of adsorption on SACs is of great importance. Zeng *et al* [168] propose an electronic descriptor in terms of valence electrons of occupied *d*-orbital of metal element (θ_d) and electronegativity of surface atoms to explain the trends of adsorption energies of OH and H on graphene-based SACs (see figures 10(a) and (b)). The electronic descriptor takes the local environment of single TM atom and its nearest neighbors into consideration and is expressed as follows,

$$\varphi = \theta_d \times \frac{E_M + \alpha \times (n_N \times E_N + n_C \times E_C)}{E_{O/H}} \tag{28}$$

E_M, E_N and E_C represent the electronegativity of metal element, nitrogen element and carbon element respectively. $E_{O/H}$ is the electronegativity of O element or H element which is determined by the adsorbate OH or H. n_N and n_C are the number of nearest-neighbor N and C atoms, and α is coefficient correction. α is

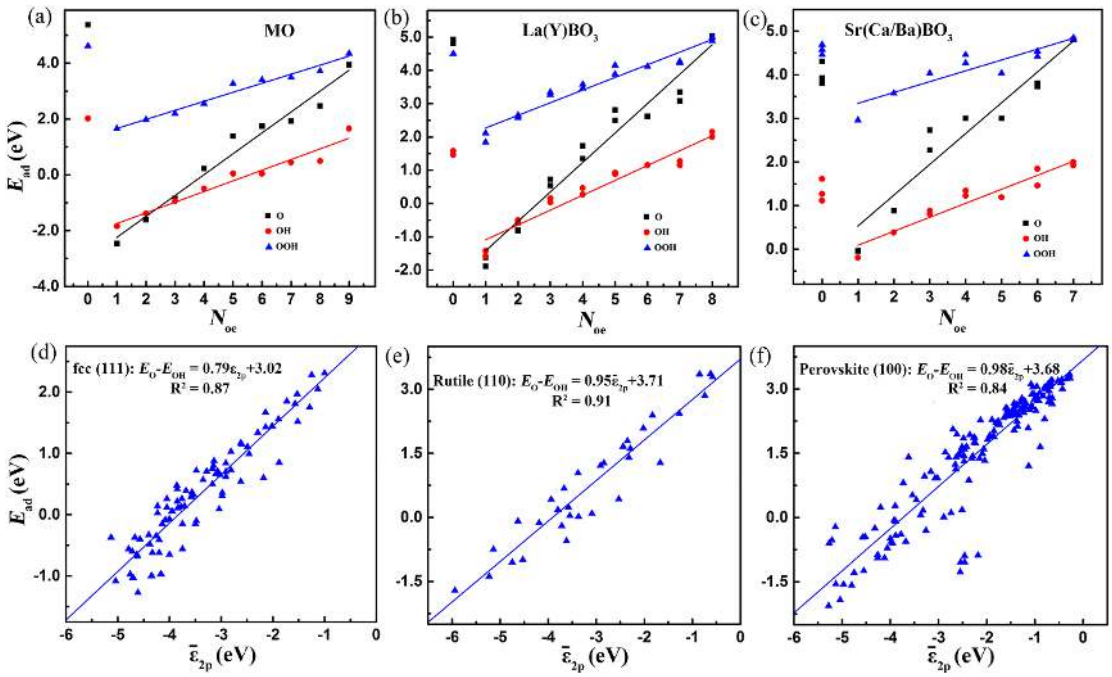

Figure 9. Electronic models for transition-metal (TM) oxides. (a)–(c) The adsorption energies of O, OH and OOH versus the outer electrons (N_{oe}) on monoxides (MO) (a) and perovskite oxides (ABO_3) (b) and (c) (100) surfaces. The data are adapted from [152]. (d)–(f) The energies of $E_O - E_{OH}$ versus the average O 2*p*-state energy ($\bar{\varepsilon}_{2p}$) on fcc(111), rutile (110) and perovskite oxides (100) surfaces. The data are adapted from [154] and [155].

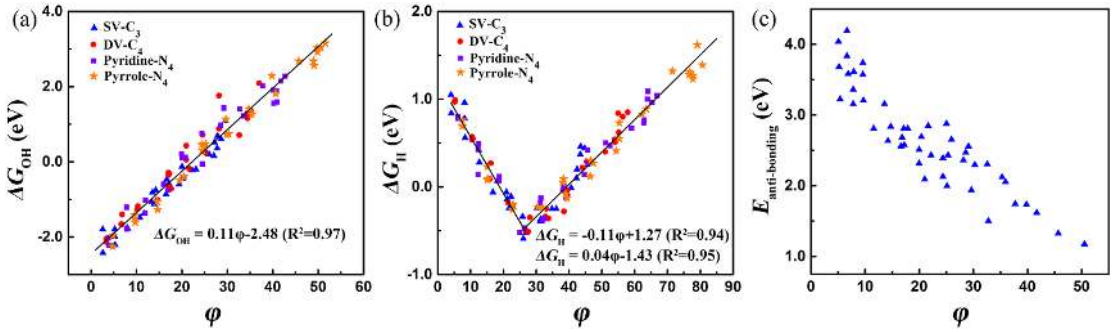

Figure 10. Electronic models for single-atom catalysts (SACs). (a), (b) The adsorption free energies of OH (a) and H (b) versus φ on SACs (3*d*, 4*d* and 5*d* single transition-metal (TM) atoms are doped in a graphene sheet with different coordination environments, including a single vacancy with three carbon neighbors ($SV\text{-}C_3$), a double vacancy with four carbon neighbors ($DV\text{-}C_4$), four pyridine nitrogen atoms ($pyridine\text{-}N_4$) and four pyrrole nitrogen atoms ($pyrrole\text{-}N_4$)). (c) The negative correlation between the band center of the antibonding orbitals and φ. The data are adapted from [168].

equal to 1.25 for single-TM-atom-pyrrole-N_4 and is equal to 1 for other active centers. It could be figured out that the adsorption free energy of OH ΔG_{OH} scales linearly with increasing φ on graphene-based SACs, namely the adsorption strength weakens with φ increases. This trend can be understood by the *d*-band model [5, 8, 9], which demonstrates that the lower *d*-band center gives rise to lower antibonding states and higher occupations, leading to the weak adsorption strength. Figure 10(c) shows a negative correlation between the band center of the antibonding orbital and φ. Therefore, the increase of φ corresponds to the downshift of *d*-band, thereby weakening the adsorption energy. Figure 10(b) illustrates the relationship between the adsorption free energy of H ΔG_H and φ, exhibiting a broken-line behavior. For SACs with $\varphi > 27$, ΔG_H increases linearly with φ, which is consistent with the trends of ΔG_{OH}. In contrast, the opposite trend can be observed for SACs with $\varphi < 27$ that ΔG_H decreases with increasing φ. This is due to the fact that the bonding states locate near the Fermi level instead of the deep-lying level when φ is too small so that the bonding states upshift with the upward shifting of *d*-band (corresponding to the decrease of φ), leading to the weakening of adsorption energy [169]. Remarkably, this electronic model can be easily generalized to describe the trends of adsorption energies for macrocyclic-molecule based SACs, implying the portability of this model. Unfortunately, this model cannot describe the trends of adsorption energies for TMs.

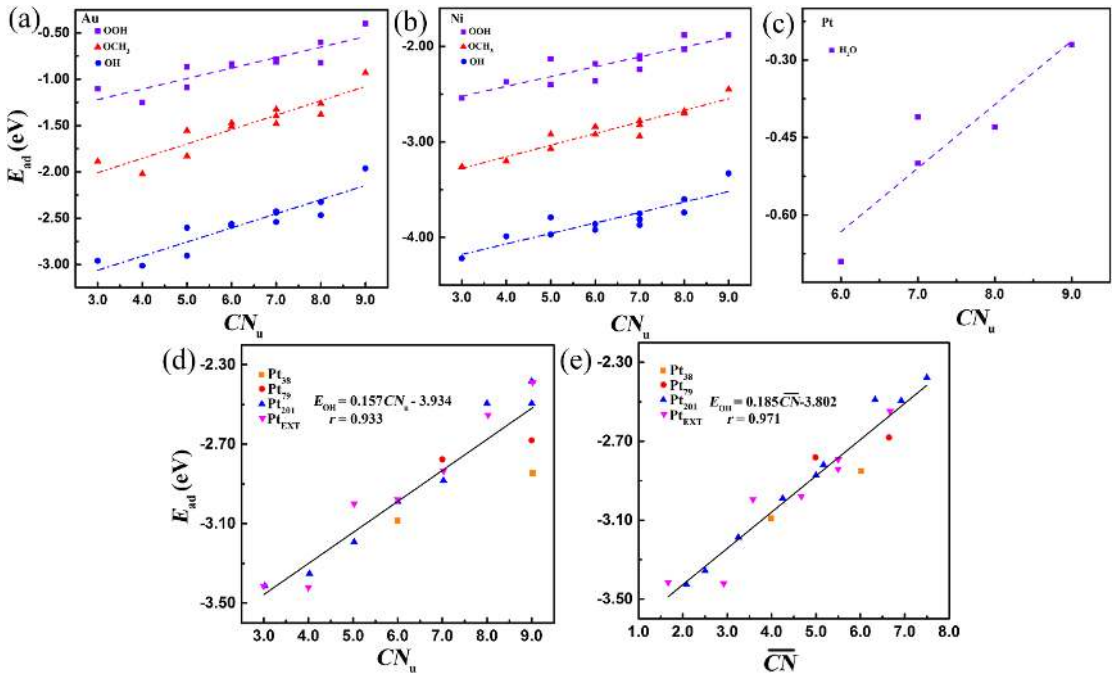

Figure 11. Adsorption energy against the usual coordination number (CN_u) and the generalized coordination number ($\overline{CN}$). (a)–(c) The adsorption energies of OH, OOH, OCH_3 and H_2O versus CN_u on Au (a), Ni (b) and Pt (c) extended surfaces. The data are adapted from [33] and [170]. (d), (e) The adsorption energies of OH versus CN_u (d) and $\overline{CN}$ (e) on Pt extended surfaces and Pt-nanoparticles (NPs). The data are adapted from [25].

2.5. Geometric models

We now attempt to uncover the geometric determinants of adsorption. It is widely acknowledged that adsorption on surfaces is strongly dependent on the geometric structures of surface atoms. For example, atoms of step surfaces or kink sites of NPs are normally more reactive than those of flat surfaces and bind to adsorbates stronger. This geometric effect is generally understood with the concept of coordination number (CN). Herein we introduce several geometric models in regard to CN, unravel their mechanisms in understanding adsorption on surfaces, discuss the geometric effects of strain, and clarify the correlation between the geometric and electronic models.

2.5.1. Usual coordination number model

One of the most intuitive descriptions of geometric structure for surface atoms is the usual coordination number (CN_u), which is defined by the number of nearest atoms bonded to the central atom, for instance, CN_u is equal to 9 for atoms on fcc(111) surfaces. This descriptor provides a good description for the geometric effects of adsorption energy as seen in figures 11(a)–(c) [33, 170], where the adsorption energies of OH, OOH, OCH_3 and H_2O increase linearly with CN_u for difference extended surface sites. The mechanism of this trend can be understood by the bond-order conservation theory [171, 172]: the larger CN_u of surface atoms such as (111) facet implies the less broken bonds, consequently the tendency for surface atoms to form new bonds and the strength of adsorption energy become weaker as seen in figures 11(a)–(c).

2.5.2. Generalized coordination number model

CN_u successfully describes the geometric effects of adsorption energy despite its simple arithmetical form. However, it indeed has some limitations. For surface sites with similar coordination distribution, it is too hard for CN_u to effectively distinguish their geometric effects. As seen in figure 11(d) [25], several surface sites of different NPs possess the same CN_u, while the adsorption energies of these sites vary up to 0.5 eV, which is far beyond ±0.2 eV, the error of DFT with (semi-) local approximation. Therefore, finding a more general expression of the geometric structure is necessary. A successful model is the generalized coordination number ($\overline{CN}$) [25], a first-order extension of CN_u, which takes the second nearest neighbors of active sites into consideration. For a given atom i with n_i nearest neighbors on surface, $\overline{CN}$ is expressed as follows,

$$\overline{CN}(i) = \frac{\sum_{j=1}^{n_i} CN(j)\, n_j}{CN_{\max}} \tag{29}$$

where CN_{max} is the CN_u for the corresponding crystals, for instance, CN_{max} is 12 and 8 for fcc [or hexagonal close-packed (hcp)] crystals and body-centered cubic (bcc) crystals respectively. Moreover, equation (29) can be extended to bridge sites with $CN_{max} = 18$ for fcc crystals, which is the number of nearest neighbors that surround the two bridge-site atoms in bulk, and to hollow sites with $CN_{max} = 22$ for threefold sites and $CN_{max} = 26$ for four-fold sites.

Figure 11(e) exhibits the adsorption energies of OH against $\overline{CN}$, where an evident linear relationship is observed [25]. More importantly, the adsorption energies for the similar sites of different NPs are separated apart and follow the guiding line. Since $\overline{CN}$ involves more general geometry of surfaces and is more sensitive to the geometric variations of active sites, it is no wonder that $\overline{CN}$ provides a more accurate description for the geometric effects of adsorption than CN_u. Likewise, the linear increase of adsorption energy with $\overline{CN}$ can also be explained by the fact that the decrease in coordination corresponds to the increase in the bonding strength, following the bond-order conservation theory [171, 172].

2.5.3. Geometric model for strain effects

$\overline{CN}$ can also be extended to explain strain effects by slightly modifying its definition [133]. In the case of strain, the usual coordination number CN_u can be expressed as,

$$CN_u = \sum_{k=1}^{n_i} \frac{d_{bulk}}{d_i - d_{k=1}} \tag{30}$$

where d_{bulk} and $d_i - d_{k=1}$ are the interatomic distance in the bulk and in the surface respectively. The simplest approximation of equation (30) is that the difference between bulk and surface interatomic distance is negligible, leading to $CN_u = \sum_{k=1}^{n_i} 1 = n_i$. Then one can consider the second-nearest neighbors for an atom by the sum of weights of its nearest neighbors as,

$$\overline{CN}^* = \frac{1}{CN_{max}} \sum_{j=1}^{n_j} \sum_{k=1}^{n_i} \frac{d_{bulk}}{d_i - d_{k=1}} \tag{31}$$

Note that equation (31) will transform to equation (29) automatically when d_{bulk} is approximated equal to $d_i - d_{k=1}$. In contrast, if the difference between bulk and surface interatomic distance is not negligible while the surface interatomic distance is approximated as an average value $\bar{d}$, $\overline{CN}^*$ can be expressed as,

$$\overline{CN}^* \approx \frac{d_{bulk}}{\bar{d}} \frac{1}{CN_{max}} \sum_{j=1}^{n_j} \sum_{k=1}^{n_i} 1 = \frac{d_{bulk}}{\bar{d}} \overline{CN} \tag{32}$$

Recalling that strain (S) is related to the interatomic-distance difference that obeys the relation $S = \frac{\bar{d} - d_{bulk}}{d_{bulk}} = \frac{\bar{d}}{d_{bulk}} - 1$ [132]. Accordingly, one obtains that:

$$\overline{CN}^* \approx \frac{1}{1+S} \overline{CN} \tag{33}$$

Equation (33) demonstrates that strain effects can be involved in the concept of coordination. Note that tensile strain and compressive strain correspond to the positive and negative value of S respectively, namely tensile strain (compressive strain) gives rise to the decrease (increase) of $\overline{CN}^*$ shown in equation (33).

Figure 12 plots the adsorption energies of OH and OOH versus $\overline{CN}^*$ on Pt(111), Pt(533), Pt(221) and cavity B surfaces with strain ranging from −3% to +3% [133]. Clearly, the adsorption energies of OH and OOH scale linearly with $\overline{CN}^*$ for all surfaces, demonstrating that $\overline{CN}^*$ indeed captures the strain effects of adsorption. Since both the generalized coordination number model and the d-band model describe a linear relationship with adsorption energy under strain, there may exist some links between these two models.

2.5.4. The relationship and distinction between the coordination number model and the d-band model

Generally, the variation of geometric structures may also give rise to the change of electronic structures [5]. Therefore, it is necessary to re-recognize the coordination number model from the view of electronic structures such as the d-band model and uncover the links and distinctions between the two models. The change in coordination numbers of surface atoms generates the change in the overlaps of electronic states, leading to the movement of states especially that of d-bands for TMs. When the coordination number for a given atom on TM surface decreases, the overlap of d-band also declines, thereby the d-band width W_d decreases and d-band center ε_d moves upshift towards Fermi level [5, 173, 174]. Hence, more empty antibonding states interact with adsorbates, leading to the enhancement of adsorption strength. From this

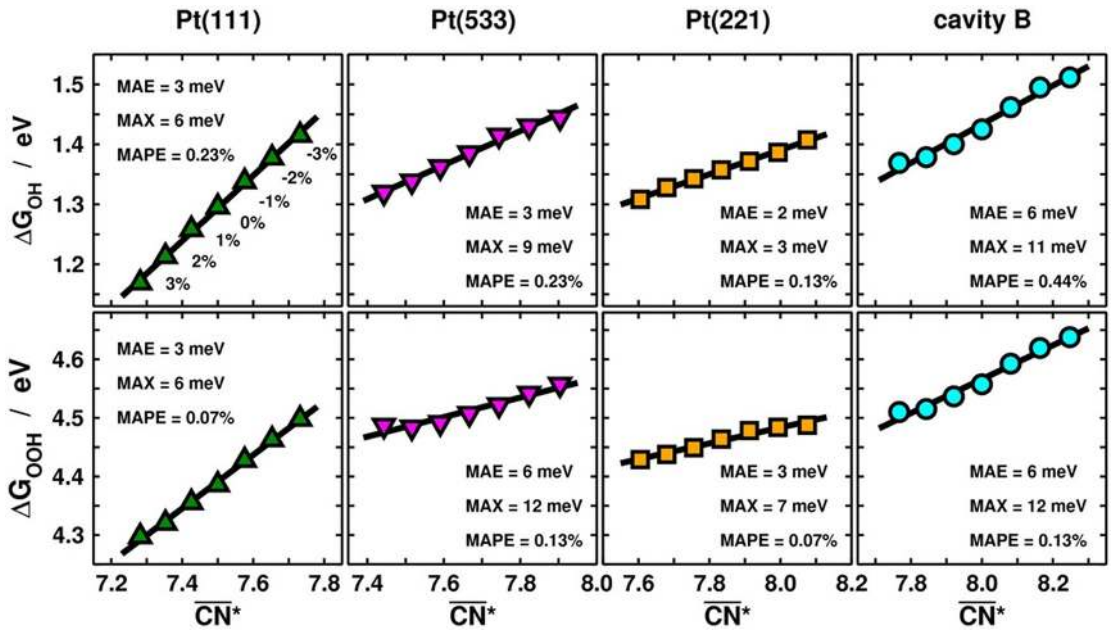

Figure 12. The adsorption energies of OH and OOH under strain versus the generalized coordination number ($\overline{CN}^*$) on Pt(111), Pt(533), Pt(221) and Cavity B surfaces. [133] John Wiley & Sons © 2018 Wiley-VCH Verlag GmbH & Co. KGaA, Weinheimundefined.

point, there indeed exist certain relationships between the coordination number model and the *d*-band model, and the coordination effects in adsorption energy can be understood by the *d*-band theory.

Calle-Vallejo *et al* [25] derive an approximately linear correlation between ε_d and $\overline{CN}$ based on broken-bond model [175–177] (which is a semi-empirical model to calculate surface energies of elemental crystals in solid phase) as follows,

$$\varepsilon_d^{surf} \approx \varepsilon_d^{bulk} + \frac{E}{2\theta_d f}\left(\frac{\overline{CN}_{surf}}{\overline{CN}_{bulk}} - 1\right) \tag{34}$$

where ε_d^{surf} and ε_d^{bulk} are the *d*-band center of atoms on surface and in the bulk respectively, E is cohesive energy of materials, θ_d is the average occupations of *d*-states and f is an additional ratio factor ($\theta_d = 1.8$ and $f = 1.125$ for Pt). Equation (34) demonstrates that the *d*-band center of surface atoms is mainly dominated by four factors: the *d*-band center of bulk atoms, the cohesive energy of materials, the electronic occupations of *d*-bands and the geometric environments around atoms. It should be noted that for a given kind of material, ε_d^{bulk}, E, θ_d, f and $\overline{CN}_{bulk}$ are all constants, which means that ε_d^{surf} scales linearly with $\overline{CN}_{surf}$. Equation (34) provides a quantitative relationship between ε_d and $\overline{CN}$ and proves again the variation of geometric structures leads to the variation of electronic structures.

Although the underlying mechanism of the coordination number model in adsorption can be explained by the *d*-band model, it does not mean that the former can be replaced by the latter. Actually, both the two models and their descriptors have strengths and limitations. Figure 13 illustrates the adsorption energies of OH and OOH on Pt_{201} NPs and extended surfaces against ε_d and $\overline{CN}$ respectively [25]. Although two linear scalings can be easily established, there are about ten different sites with variable adsorption energies possessing the similar ε_d at around −2.34 eV, indicating that ε_d is not a good descriptor in characterizing the trends of adsorption energy for these sites such as kinks and edges. In contrast, $\overline{CN}$ can well describe the variation of adsorption energies for these sites. On the other hand, ε_d is more effective to clarify the variation of adsorption energies from one TM to the next compared to $\overline{CN}$. Particularly, for a fixed adsorption site on given crystal surfaces, such as the top site on fcc(111) surfaces, $\overline{CN}$ is the same for all kinds of fcc metals, while the adsorption energies of different metals vary a lot. Namely, $\overline{CN}$ becomes invalid under this circumstance.

Overall, there indeed exist the links between the *d*-band model (electronic model) and the coordination number model (geometric model), whereas these two different models are not identical in many cases.

2.5.5. Orbitalwise coordination number

$\overline{CN}$ captures relatively accurate geometric information of a given active center and effectively describes the geometric effects of adsorption. Although it is a general concept and can be easily extended to the third- or more neighboring atoms, $\overline{CN}$ is unable to describe some specific systems such as alloys. A series of alloys may

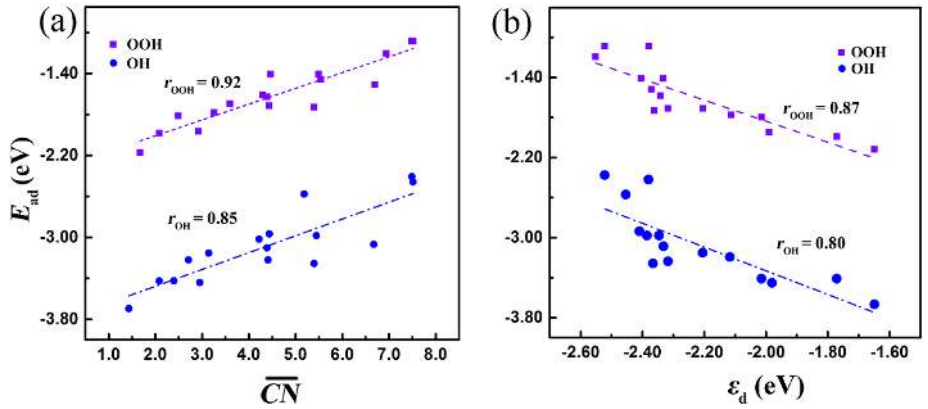

Figure 13. The comparison between the generalized coordination number model ($\overline{CN}$) and *d*-band model. (a) The adsorption energies of OH and OOH versus $\overline{CN}$ on Pt extended surfaces and Pt_{201} nanoparticles (NPs). (b) The adsorption energies of OH and OOH versus the *d*-band center ε_d on Pt extended surfaces and Pt_{201} NPs. The data are adapted from [25].

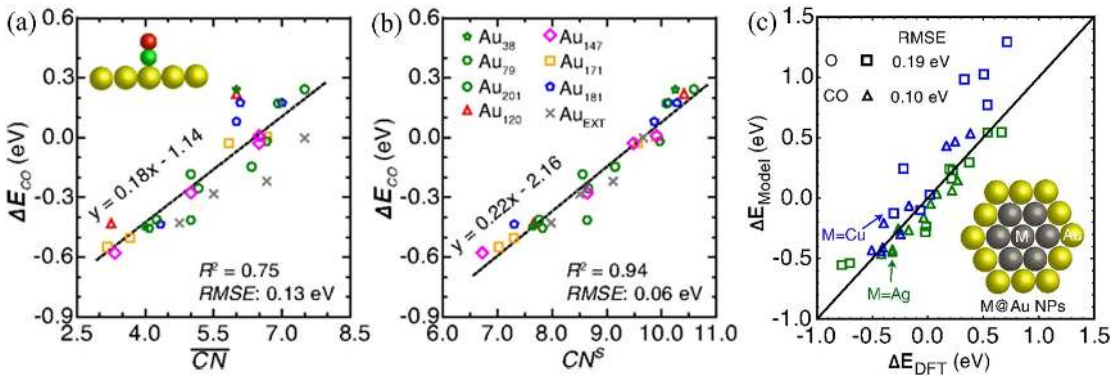

Figure 14. The orbitalwise coordination number model (CN^α) in describing the adsorption energy. (a), (b) The Adsorption energies of CO versus the generalized coordination number ($\overline{CN}$) and CN^α on Au extended surfaces and nanoparticles (NPs). (c) The comparison between the DFT-calculated adsorption energies of O and CO on M@Au core–shell NPs and the predicted ones by CN^α. Reprinted figure with permission from [178]. Copyright (2017) American Physical Society.

have the same value of $\overline{CN}$ but the ability of adsorption varies a lot. Xin *et al* [178] consider both the electronic and geometric structure of surface atoms, quantify the degree of coordinative saturation of metal atoms and their inclination to form new bond, and thus propose a descriptor based on the moments theorem [179] called orbitalwise coordination number as,

$$CN_i^\alpha = \frac{M_{2,i}^\alpha}{\left(t_{nn}^{\alpha,\infty}\right)^2}, \text{ where } \alpha = s \text{ or } d \tag{35}$$

$M_{2,i}^\alpha$ is the second moment of the distribution $\{\varepsilon_i^\alpha\}$ ($\{\varepsilon_i^\alpha\}$ is the moment eigenspectrum of the projected DOS onto the TM or noble metal atom *i*), which determines the variation in the local chemical reactivity of an adsorption site perturbed by neighboring atoms. $t_{nn}^{\alpha,\infty}$ is the sum of the α-electron hopping integrals to relevant valence orbitals of a neighboring atom in the bulk, which depends strongly on the orbital size or shape and internucleus distance. Figures 14(a) and (b) plot the adsorption energies of CO on NPs with various size and shape (cuboctahedron, truncated octahedron, tetrahedron and cube) as a function of $\overline{CN}$ and CN^α [178]. Clearly, CN^α provides a better description for the trends of adsorption energy of various-shape NPs due to the larger regression coefficient and smaller standard deviation. More importantly, CN^α can easily capture the properties of alloys as seen in figure 14(c) since it considers the electronic structure of surface atoms [178]. The small deviations between the predicted and DFT-calculated adsorption energies of CO and O on a series of core–shell NPs demonstrate the validity and reliability of CN^α in describing alloys. Unfortunately, this model requires complex DFT-calculations to obtain the basic parameters, resulting in the expensive costs and inconveniences.

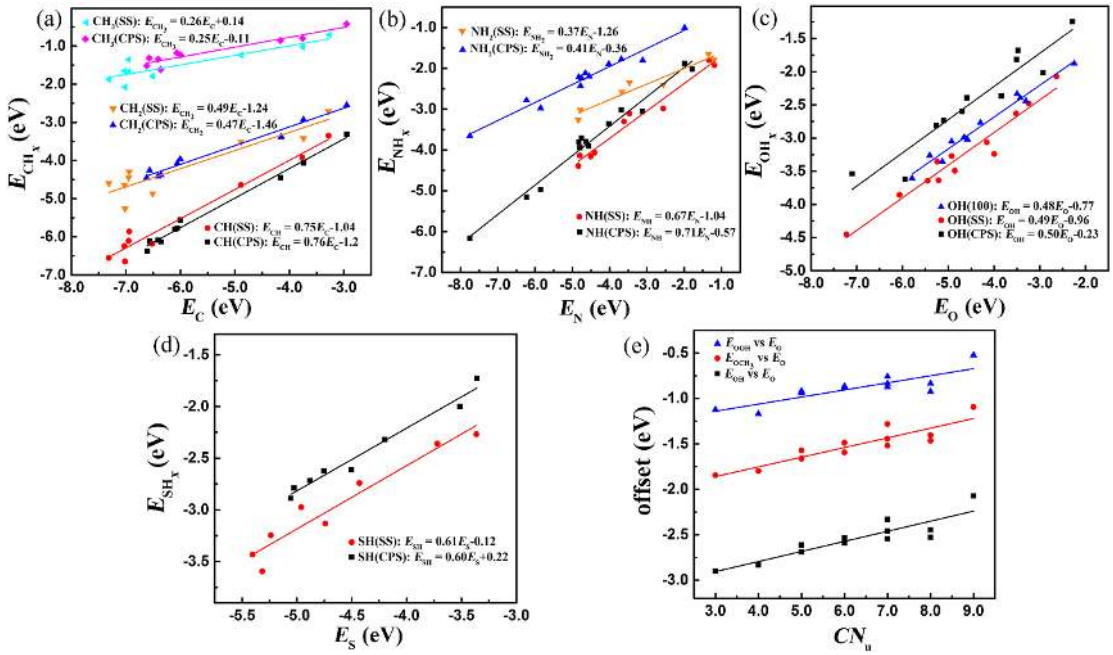

Figure 15. The dependence of the slope and offset of the linear scaling relationship (LSR). (a)–(d) The adsorption energies of AH_x versus the adsorption energies of A on transition-metal (TM) close-packed surfaces (CPS), stepped surfaces (SS) and (100) surfaces for species binding via C (a), N (b), O (c) and S (d). The data are adapted from [32]. (e) The offset of the LSR of OH vs O, OOH vs O and OCH_3 vs O versus the usual coordination number (CN_u) on TM extended surfaces. The data are adapted from [33].

2.6. The linear scaling relationship

The electronic models and the geometric models discussed above are mainly used to explain the trends of adsorption energy on different substrates, while rarely uncover the correlation between the adsorption energies of variant adsorbates. The LSR [32, 33] provides a profound solution to this issue, and it propose the relation between the adsorption energies for atoms and their partially hydrogenated species. In this section we summarize a simple derivation of the LSR, including its slope and intercept, and uncover its underlying mechanisms and connotations as well as the limitations.

Nørskov *et al* [32] first discover the LSR and ascertain the determinants of its slope for atoms and their partially hydrogenated species on TM surfaces. As shown in figures 15(a)–(d), the adsorption energies of AH_x is linearly related to adsorption energies of atom A as,

$$E^{AH_x} = \gamma(x)\, E^{A} + \xi \tag{36}$$

The slope in equation (36) is equal to $\gamma(x) = (X_m - X)/X_m$, where X_m and X are the maximum and actual numbers that the central atom of a given adsorbate bond to the specific coordinating group. The underlying mechanism of equation (36) can be understood by the *d*-band model [5, 8, 9]. As mentioned above, the adsorption energy can be divided into the coupling of adsorbate states with the *sp*-states and *d*-states of TMs, seen in equation (21). The coupling between adsorbates and metal *s*-states can be considered as a constant for different metals, and the main contribution to the variation in bond strength from one TM to the next comes from the coupling to the *d*-states. Assuming that $E_d^{AH_x} = \gamma(x)\, E_d^{A}$, one can rewrite equation (21) as,

$$\begin{aligned} E^{AH_x} &= E_d^{AH_x} + E_{sp}^{AH_x} = \gamma(x)\, E_d^{A} + E_{sp}^{AH_x} \\ &= \gamma(x)\, E^{A} + E_{sp}^{AH_x} - \gamma(x)\, E_{sp}^{A} \\ &= \gamma(x)\, E^{A} + \xi \end{aligned} \tag{37}$$

This is exactly equation (36). Hence, in order to ensure the validity of equation (36), it is crucial to estimate whether the above assumption that the *d*-coupling for AH_x is proportional to $\gamma(x)$ is correct, which requires the establishment of the expression between adsorption energy and the electronic properties of adsorbates and substrates.

EMT [107] can be utilized to understand and obtain the expression of $\gamma(x)$. In EMT, adsorption can be viewed as the adsorbates interacting with a homogeneous electron gas. Generally, there exists an equilibrium position of adsorption with electron density n_0, where the adsorption energy reaches minimum. Nørskov *et al* [32] adopt the zero-order approximation in EMT (equation (18)) to rationalize the slope term of the LSR, obtaining the expression for AH_x:

$$n_{\mathrm{surf}} = \frac{X_{\mathrm{m}} - X}{X_{\mathrm{m}}} n_0 = \gamma(x)\, n_0 \tag{38}$$

The *d*-band model suggests that the coupling to *d*-states scales with the square of the coupling matrix element V_{ad}^2. The decay length of n_{surf} is related to work function, which is the energy of the Fermi level relative to the vacuum. Since *d*-states also has energy close to the Fermi level, the decay length of *d*-bands may approximately the same as that of n_{surf}, namely $V_{\mathrm{ad}}^2 \propto \mathrm{n}_{\mathrm{surf}}$ [32]. Therefore, one can approximate that as follows,

$$E_{\mathrm{d}} \propto V_{\mathrm{ad}}^2 \propto \mathrm{n}_{\mathrm{surf}} \propto \frac{X_{\mathrm{m}} - X}{X_{\mathrm{m}}} = \gamma(x) \tag{39}$$

Equation (39) demonstrates the reasonability of equation (36) and unravels an approximate physical picture about the dependence of the LSR' slope. However, an obvious deficiency of these derivations is the neglect of the first-order term of EMT, which had been demonstrated to be essential for describing the adsorption energy of adsorbates that are not particularly polarizable such as hydrogen-containing molecules [107].

Now we turn to discuss the intercept of the LSR. Calle-Vallejo *et al* [33] find a linear correlation between the offsets of the adsorption-scaling for oxygenates versus oxygen and the usual coordination number CN_{u} (see figure 15(e)), namely the offset of the LSR depends on the geometric structures of surfaces. To rationalize this finding, they made a key assumption, by assuming that the electronic and geometric determinants of adsorption energy can be separated independently. Given species at facet *i*, one can obtain that:

$$E^{(i)} = g^{(i)}\left(\{\omega_j\}\right) + \beta^{(i)} \tag{40}$$

where $\{\omega_j\}$ is a set of electronic-structure parameters, $g^{(i)}$ is a function of $\{\omega_j\}$, and β is a parameter of surface geometry. Thus, the general expression for the offset of the LSR is as,

$$B_{1,2}^{(i)} = \left[f^{(i)}\left(\{\omega_j\}\right) - \gamma_{1,2}\, g^{(i)}\left(\{\omega_j\}\right)\right] + \left[\beta_2^{(i)} - \gamma_{1,2}\beta_1^{(i)}\right] \tag{41}$$

To obtain the dependence of the offset of the LSR on the surface geometries, it immediately requires $f^{(i)}\left(\{\omega_j\}\right) = \gamma\, \mathrm{g}^{(i)}\left(\{\omega_j\}\right)$, which is exactly the assumption that made by Nørskov *et al* [32] and Koper *et al* [138] for explaining the slopes of LSR. Considering a special case that species 2 and 3 scale with species 1 with the same slope such as OH and OOH versus O, one obtains,

$$E_3^{(i)} - E_2^{(i)} = B_{1,3}^{(i)} - B_{1,2}^{(i)} = \beta_3^{(i)} - \beta_2^{(i)} \tag{42}$$

Thus, the difference of adsorption energy is only determined by the geometric parameter β. The fitted correlations in figure 15(e) [33] further indicate that although $\beta_3^{(i)}$ and $\beta_2^{(i)}$ depend on the coordination numbers, their difference is constant for all considered surfaces. Namely, the difference between adsorption energies for any pair of oxygenates that binding to surface with oxygen is constant despite the electronic nature and geometric structure of surface, which reflects the experimental thermodynamics limitation for ORR [33, 180]. Now a complete expression of the LSR and its generalized form can be provided for atoms and their partially hydrogenated species as,

$$E_2 = \gamma(x)\, E_1 + \mu CN_{\mathrm{u}} + \vartheta_{1,2} \tag{43}$$

Equation (43) represents the entire LSR and its generalized form. However, the coefficient of CN_{u} term μ and the constant term $\vartheta_{1,2}$ remain unclear and this expression has only been verified to be effective for oxygen and its partially hydrogenated species such as OH_x ($x = 0, 1$), OOH and OCH_3.

Despite the great significance, the LSR and its generalized form still need further evidence and support from a more basic perspective. First, it is crucial to verify whether the assumptions that the *d*-coupling for AH_x is proportional to $\gamma(x)$ and the electronic and geometric determinants of adsorption energy can be separated independently are correct. Secondly, the generalized LSR does not provide a general expression for determining the geometric effect, with the prefactor of the coordination term and the constant term in equation (43) ambiguous. Thirdly, the perturbation induced by the adsorbed atom to the electron density,

namely the contribution of the first-order term of EMT to the adsorption energy, has to be identified. Fourth, the slope of LSR is only suitable for the atoms and their partially hydrogenated species and has not been applied to more complicated adsorbates like CO, CHO and COOH, which are crucial intermediates in numerous reactions. Last but not least, the LSR is the relationship between the adsorption energies of two species, thus requiring DFT-calculations to obtain the adsorption energy for at least one species on all considered substrates which are still expensive. To solve these issues, it is necessary to study the relation between the adsorption energy and the easily accessible intrinsic electronic and geometric properties of adsorbates and substrates.

2.7. The intrinsic model

Recently we propose a novel model [34] to correlate the adsorption energy with the intrinsic properties of adsorbates and substrates. This intrinsic model can naturally deduce the well-established LSR and its generalized form, generalizes the efficiency and limitation of engineering the adsorption energy and reaction energy, and enables rapid screening of potential candidates and designing of catalysts since all parameters are accessible and predictable. In this section, we introduce the framework of this intrinsic model and unravel its underlying theoretical basis and mechanistic insights.

2.7.1. Framework and performance

We identify the three main factors that control the adsorption on surfaces are the valence and electronegativity of surface atoms, the coordination of active sites and the valence of adsorbates, which correspond to the electronic descriptor ψ and the geometric descriptor $\overline{CN}$. The entire expression of the adsorption energy on TMs and NPs can be expressed in terms of ψ and $\overline{CN}$ as,

$$E_{\mathrm{ad}} = 0.1\times\frac{X_{\mathrm{m}} - X}{X_{\mathrm{m}} + 1}\times\psi + 0.2\times\frac{X+1}{X_{\mathrm{m}}+1}\times\overline{CN} + \theta \tag{44}$$

where X_{m} and X are the maximum and actual numbers that the central atom of a given adsorbate bond to the specific coordinating group. θ is constant for a given adsorbate and is the only pending parameter that needs to be determined, e.g. through DFT calculations, while the rest parameters are intrinsic and readily accessible. Clearly, this scheme allows a rapid estimation of the adsorption trend on different surfaces (without calculation cost). Note that the determination of θ only needs the calculations of a given adsorbate on one substrate.

One of the most important features of the intrinsic model is that we introduce a brand-new descriptor ψ to effectively consider the local-environment effect of the active sites based on the valence and electronegativity of surface atoms as:

$$\psi = \frac{\left(\prod_{i=1}^{N} S_{\mathrm{v}_i}\right)^{2/N}}{\left(\prod_{i=1}^{N}\chi_i\right)^{1/N}} \tag{45}$$

where S_{vi} and χ_i are the numbers of outer electrons and the electronegativity of the ith atom around the surface active center, and N is the sum number of neighboring atoms. Normally, the minimum repeat units are utilized to consider the effects of the local environment around the active centers. Taking the top-site adsorption on Pt-X@Pt(111) as an example, the local active centers contain one Pt atom at the adsorption site with $N_{\mathrm{adsorption}}\,(\mathrm{Pt}) = 1$, and six Pt atoms with $N_{1\mathrm{st}}\,(\mathrm{Pt}) = 6$ and three X atom with $N_{1\mathrm{st}}\,(X) = 3$ at the first-nearest neighboring sites so that the sum number of N is equal to 10. By considering the geometric mean of the valence and electronegativity for these atoms, one can obtain the value of the descriptor ψ. Note that equation (45) is a universal expression which is suitable for pure TMs, NPs, NSAs, oxides and SACs. Since the active center and its local coordinations are the same in pure TMs and NPs, equation (45) automatically decays to a simpler form in calculating pure TMs and NPs that:

$$\psi = \frac{S_{\mathrm{v}}^2}{\chi^{\beta}} \tag{46}$$

β is a parameter determined by the role of d- and s-orbitals in valence descriptions and electronegativity for TMs: $\beta = 1/2$ for Ag and Au while $\beta = 1$ for the other TMs, reflecting the fact that the d-state contribution to the adsorbate-surface binding is much less important in Ag and Au than in the other TMs (due to the full-filled d-band and the low position of d-band center relative to the Fermi levels in Ag and Au) [5, 108].

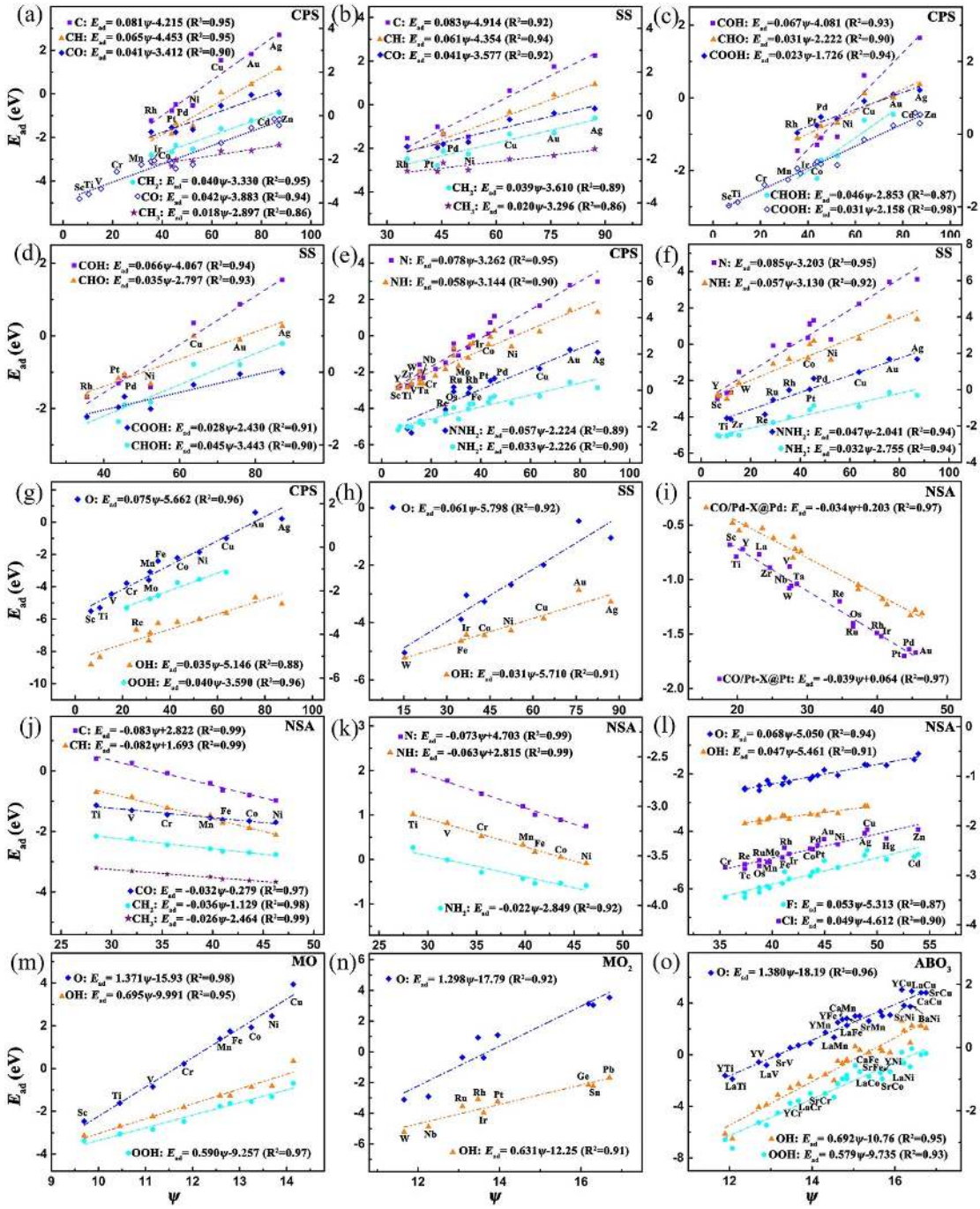

Figure 16. Adsorption energies against the electronic descriptor ψ on transition metals (TMs), near-surface alloys (NSAs) and oxides. (a), (b) CH_x and CO on close-packed (a) and stepped (b) surfaces (CPS and SS) of pure TMs [18]. (c), (d) COH, CHO, COOH, and CHOH on CPS (c) and SS (d) of pure TMs [18]. (e), (f) NH_x and NNH_2 on CPS (e) and SS (f) of pure TMs [13]. (g), (h) OH_x and OOH on CPS [152, 154] (g) and SS [32] (h) of pure TMs. (i) CO on (100) surface of the Pt- and Pd-NSAs [182]. (j)–(l) CH_x and CO [141] (j), N and NH_x [141] (k), OH_x, F, and Cl [138, 181] (l) on (111) surface of the Pt-NSAs. (m)–(o) OH_x and OOH on (100) surface of monoxides MO(100) [152] (m), (110) surface of dioxides MO_2(110) [154] (n), and (100) surface of perovskite oxides ABO_3(100) [152] (o). Reproduced from [34]. CC BY 4.0.

Figure 16 exhibits the adsorption energies against the electronic descriptor ψ for various adsorbates on TMs, NPs, NSAs and oxides [34]. The adsorbates we considered cover CH_x ($x = 0, 1, 2, 3$), CO, COH, CHO, CHOH, COOH, NH_x ($x = 0, 1, 2$), NNH_2, OH_x ($x = 0, 1$), OOH, OCH_3, P, F, and Cl and the surfaces include the TM extended surfaces, NPs, NSAs with Pt and Pd hosts, monoxides, dioxides and perovskite oxides [13, 18, 32, 138, 141, 152, 154, 181, 182]. Clearly, the adsorption energies on all surfaces scale linearly with ψ and the predicted coefficients of the ψ term by equation (44) are in good agreement with the direct fitted ones of DFT calculations (see tables 2 and 3 and figure 16) [13, 18, 32, 138, 141, 152, 154, 181, 182], which strongly supports the reliability and generality of the scheme. Specially, for oxides, the adsorption energies obey the relation as $E_{ad} = 2 \times \frac{X_m - X}{X_m + 1} \times \psi + b$. Note that the constant prefactor of oxides is 2 rather

Table 2. Comparison between the predicted prefactors of ψ [34] in equation (44) and the fitted DFT-calculated ones for different adsorbates on pure transition-metal (TM) close-packed surfaces (CPS), (211) surfaces and (100) surfaces.

	$k = 0.1 \times (X_m - X)/(X_m + 1)$											
		i [32]		ii [18]			iii [13]		iv [32]			v [152]
Species	Predicted	CPS	(211)	CPS	(211)	(100)	CPS	(211)	CPS	(211)	(100)	CPS
C	0.08	—	—	0.081	0.083	0.088	—	—	—	—	—	—
CH	0.06	0.071	0.063	0.065	0.061	0.065	—	—	—	—	—	—
CH_2	0.04	0.043	0.042	0.040	0.039	0.041	—	—	—	—	—	—
CH_3	0.02	0.020	0.021	0.018	0.020	0.018	—	—	—	—	—	—
CO	0.04	0.037	0.039	0.041	0.041	0.040	—	—	—	—	—	—
COH	0.067	0.072	0.062	0.067	0.066	0.067	—	—	—	—	—	—
CHO	0.03	0.032	0.036	0.031	0.035	0.038	—	—	—	—	—	—
CHOH	0.047	0.047	0.046	0.046	0.045	0.043	—	—	—	—	—	—
COOH	0.027	—	—	0.023	0.028	0.024	—	—	—	—	—	—
N	0.075	—	—	—	—	—	0.078	0.085	—	—	—	—
NH	0.05	—	—	—	—	—	0.058	0.057	—	—	—	—
NH_2	0.025	—	—	—	—	—	0.033	0.032	—	—	—	—
NNH_2	0.05	—	—	—	—	—	0.057	0.047	—	—	—	—
O	0.067	—	—	—	—	—	—	—	0.067	0.061	0.061	—
OH	0.033	—	—	—	—	—	—	—	0.030	0.031	0.028	—
OOH	0.033	—	—	—	—	—	—	—	—	—	—	0.040

Table 3. Comparison between the predicted prefactors of ψ [34] in equation (44) and the fitted DFT-calculated ones for different adsorbates on near-surface alloys (NSAs), monoxides MO(100), dioxides MO_2(110), and perovskite oxides ABO_3(100) surfaces.

	NSAs: $\lvert k\rvert = 0.1\times (X_m - X)/(X_m + 1)$					
		i [141]	ii [181]	iii [138]	iv [182]	
Species	Predicted	Pt@M(111)	Pt@M(111)	Pt@M(111)	Pt@M(100)	Pd@M(100)
C	0.08	0.083	—	0.080	—	—
CH	0.06	0.082	—	—	—	—
CH_2	0.04	0.036	—	—	—	—
CH_3	0.02	0.026	—	—	—	—
CO	0.04	0.032	—	—	0.039	0.034
N	0.075	0.073	—	0.078	—	—
NH	0.05	0.063	—	—	—	—
NH_2	0.025	0.022	—	—	—	—
O	0.067	—	—	0.068	—	—
OH	0.033	—	0.047	—	—	—
F	0.050	—	—	0.053	—	—
Cl	0.050	—	—	0.049	—	—
P	0.075	—	—	0.074	—	—

	Oxides: $k = 2 \times (X_m - X)/(X_m + 1)$					
Species	Predicted	MO [152]	MO_2 [154]	RuO_2 [183]	ABO_3 [152]	ABO_3 [184]
O	1.334	1.371	1.298	1.487	1.380	1.358
OH	0.667	0.695	0.631	0.873	0.692	0.767
OOH	0.667	0.590	—	—	0.579	—
OCH_3	0.667	—	—	0.795	—	—

than 0.1 in equation (44), ensuring that the efficiency of engineering the adsorption energies for pure TMs, NSAs and oxides is roughly the same from one surface to the next.

The linear relationship between the offset b ($b = E_{ad} - 0.1\times\frac{X_m - X}{X_m + 1}\times\psi$) and $\overline{CN}$ is illustrated in figure 17 [34], where the DFT-fitted slopes are also consistent with the predictions by equation (44) (see table 4) [26–31, 33]. The wide choice of the species and surfaces [the species involve CO, CHO, COOH, COH, NH_x ($x = 0, 1$), OH_x ($x = 0, 1$), OOH and OCH_3, and surfaces cover Au, Cu, Ag, Pt, Co and Ni extended surfaces and NPs] ensures the generality and reliability of this model. All these findings demonstrate that the intrinsic model captures the inherent electronic and geometric determinants of adsorption systems in adsorbate-substrate bonding.

One of the most striking advantages of the intrinsic model is that it can be used to estimate the adsorption energy for given adsorption systems. Figure 18 plots the comparison between the predicted

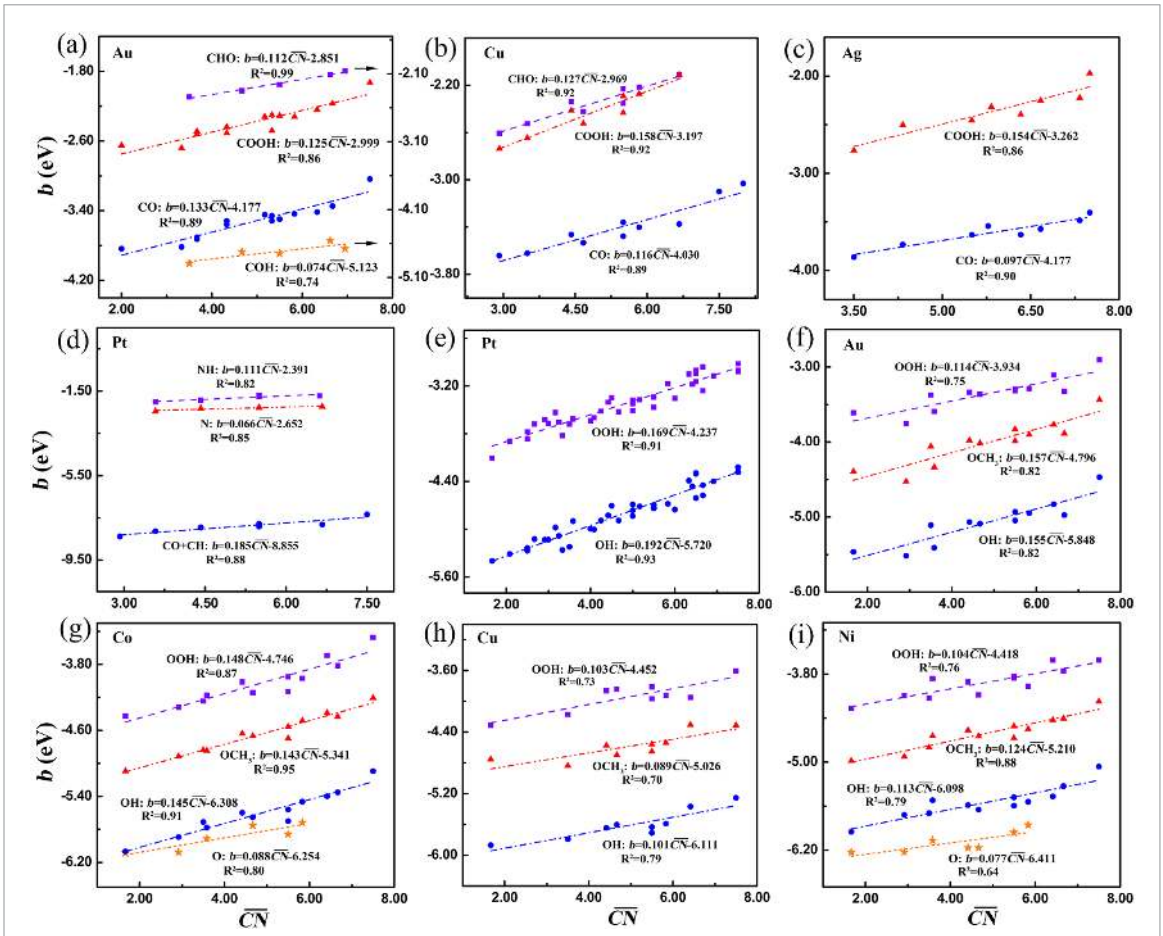

Figure 17. The offset b of the ψ-determined relation against the generalized coordination number ($\overline{CN}$). (a)–(c) The offset b for species binding via C on Au [28, 30] (a), Cu [31] (b) and Ag [27] (c) extended surfaces and nanoparticles (NPs). (d) The offset b for N, NH, CO +CH on Pt extended surfaces [29]. (e)–(i) The offset b for species binding via O on Pt [26] (e), Au (f), Co (g), Cu (h) and Ni (i) [33] extended surfaces and NPs. Reproduced from [34]. CC BY 4.0.

Table 4. Comparison between the predicted prefactors of $\overline{CN}$ [34] in equation (44) and the fitted DFT-calculated ones for different adsorbates on transition-metal (TM) surfaces and nanoparticles.

	$\lambda = 0.2 \times (X+1)/(X_m+1)$										
Species	Predicted	i [28] Au	ii [30] Au	iii [31] Cu	iv [27] Ag	v [29] Pt	vi [26] Pt	vii [33] Au	viii [33] Co	iv [33] Cu	v [33] Ni
CO	0.12	0.133	—	0.116	0.097	—	—	—	—	—	—
COH	0.067	—	0.074	—	—	—	—	—	—	—	—
CHO	0.14	—	0.112	0.127	—	—	—	—	—	—	—
CHOH	0.106	—	—	—	—	—	—	—	—	—	—
COOH	0.147	0.125	—	0.158	0.154	—	—	—	—	—	—
N	0.05	—	—	—	—	0.066	—	—	—	—	—
NH	0.1	—	—	—	—	0.111	—	—	—	—	—
O	0.067	—	—	—	—	—	—	—	0.088	—	0.077
OH	0.133	—	—	—	—	—	0.192	0.155	0.145	0.101	0.113
OOH	0.133	—	—	—	—	—	0.169	0.114	0.148	0.103	0.104
OCH_3	0.133	—	—	—	—	—	—	0.157	0.143	0.089	0.124

adsorption energies and DFT-calculated results for 25 TMs with 19 extended surfaces and another 20 NPs, 40 NSAs with 2 extended surfaces, and 85 oxides with three different crystal structures [10, 13, 17, 18, 25–33, 112, 138, 141, 152, 154, 155, 178, 181–194]. Clearly, most of the deviations are less than ±0.2 eV, the approximate error of DFT with (semi-) local approximation. Recalling the simplicity of the model, the clear picture of the underlying physics, the generality of adsorbates and substrates, and the large amount of available data, this model thus provides a solid basis for understanding and predicting the adsorption properties of small molecules.

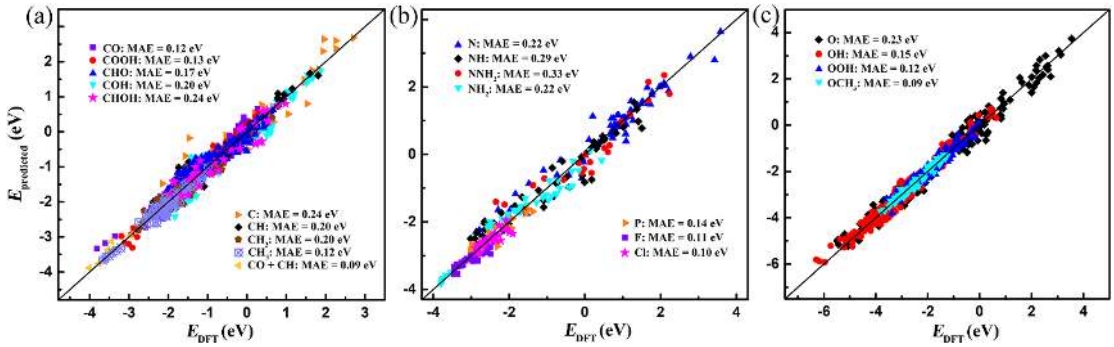

Figure 18. Comparison between the predicted adsorption energies by the intrinsic model and the DFT-calculated results. (a) The predicted and DFT-calculated adsorption energies for species binding via C [17, 18, 27–32, 138, 141, 178, 182, 185–191]. (b) The predicted and DFT-calculated adsorption energies for species binding via N, P, F and Cl [13, 20, 138, 141]. (c) The predicted and DFT-calculated adsorption energies for species binding via O [10, 25, 26, 32, 33, 112, 138, 152, 154, 155, 181, 183, 184, 192–194]. Reproduced [34]. CC BY 4.0.

2.7.2. Theoretical origin and basis

Having exhibited the high performance of the intrinsic model, we now show the underlying theoretical mechanisms of this scheme. Since the coupling between adsorbates and surfaces is determined by the valence properties of adsorption systems, it is reasonable for the electronic descriptor ψ to characterize the electronic nature of adsorption, as ψ is a function of the valence-electron number and electronegativity of surface atoms.

Figure 19 compares the electronic descriptor ψ with several established descriptors, revealing the theoretical origin and basis of ψ [34]. ψ scales linearly with the *d*-band center ε_d for 17 TMs but quadratically with that of the other 7 TMs (see figure 19(a)). It is noteworthy that these 7 TMs are the ones possessing hybridization energies that depend strongly on ε_d but weakly on the *d*-band width W_d, namely those can be well described by the *d*-band center model [112]. Hence, we introduce a W_d-dependent term to test this effect. By introducing the W_d effect on the top of ε_d with the formula of $\varepsilon_d+W_d/8$ for the 7 outlying metals, these 7 TMs immediately shift to the queue established for the other 17 TMs that only uses ε_d (see figure 19(b)). By introducing the W_d effect on the top of ε_d with the formula of $\varepsilon_d-W_d/8$ for the 17 TMs (but only using ε_d for 7 outlying metals), the 24 TMs consistently exhibit a quadratic relationship with ψ (see figure 19(c)). Hence, one can speculate that ψ reflects both the properties of ε_d and W_d, thus capturing the intrinsic electronic features of adsorption. Moreover, ψ exhibits an evident linear relationship with the upper edge of the *d*-states [112], namely the refined descriptor $\varepsilon_d + W_d/2$ (see figure 19(d)), which accounts for the effects of both the average energy of *d*-bands and their spread energy on the position of adsorbate-metal antibonding states. Actually, ψ performs even better than $\varepsilon_d + W_d/2$ due to the fact that ψ describes a single scaling line with the adsorption energy for TMs while $\varepsilon_d + W_d/2$ displays three different lines that are divided by the periods of TMs (see figure 7).

However, to the best of our knowledge, the descriptors established from the NA model are mainly suitable for pure TMs and TMs with few intermetallics, but not for oxides. Since the intrinsic model is general for the adsorption on TMs, NPs, NSAs and oxides, in particular for the adsorption of OH, F and Cl on NSAs and the adsorption of OH_x on oxides that cannot be accurately described by the *d*-band model [5, 8, 9], ψ indeed captures the electronic nature of NSAs and oxides. The reason of the inefficiency of the *d*-band model is most likely due to the fact that the *d*-band model cannot accurately characterize the effect of the local environment around the active sites. For the NSAs, ψ likely reflects not only the *d*-band center projected on the adsorption site but also the interaction between the local *d*-states of the substrate and the adsorbate state [141]. In the case of oxides, we correlate ψ with the number of outer electrons and the *p*-band center (or the O-2*p* average energy), which have been demonstrated as good descriptors in describing the trends of adsorption energy for oxides [152, 154]. Notably, ψ is also associated linearly with the number of outer electrons and the *p*-band center (see figures 19(e) and (f)), implying that ψ well manifests the outer-electron characteristics of surface atoms for oxides that cannot be depicted by the *d*-band model.

The prefactor of the electronic term $\frac{X_m-X}{X_m+1}$ can be understood and deduced by EMT [107]. As we have discussed above, in EMT, the inhomogeneous adsorption system is approximated as the interaction between the adsorbate atom and the homogeneous electron gas, so that the adsorbate atom exhibits a noble gas behavior at the optimal adsorption structures. Importantly, the first-order approximation of EMT [equations (18) and (19)] is essential for describing the adsorption of atoms that are not particularly polarizable like oxygen. One can derive the zero-order term based on the homogeneous electron gas model

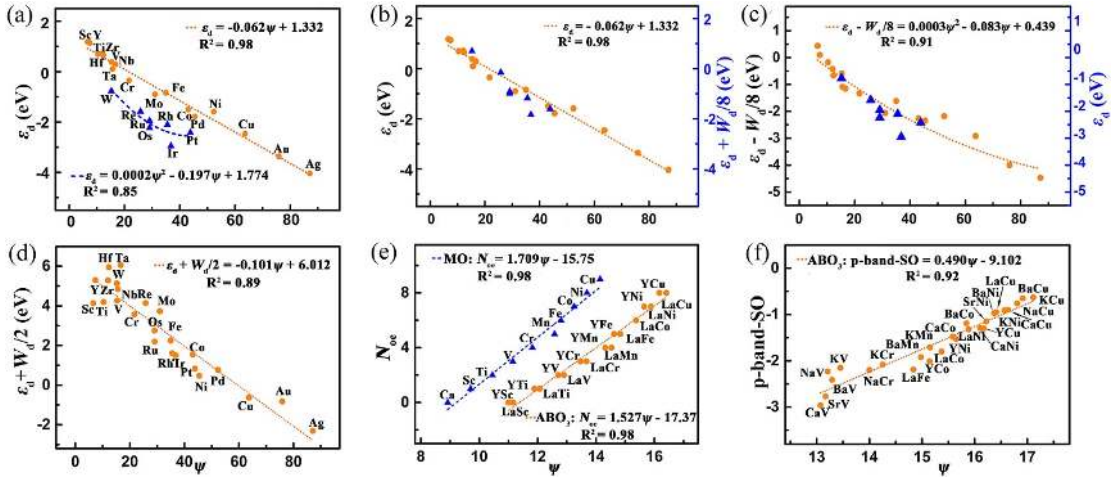

Figure 19. Comparison between the electronic descriptor ψ and other electronic descriptors. (a) The *d*-band center ε_d versus ψ for 24 transition metals (TMs) [112]. (b) ε_d versus ψ for 17 TMs, along with $\varepsilon_d + W_d/8$ (W_d denotes the *d*-band width) versus ψ for other 7 TMs [112]. (c) ε_d versus ψ for 7 TMs, along with $\varepsilon_d - W_d/8$ versus ψ for other 17 TMs [112]. (d) The upper-edge of *d*-bands $\varepsilon_d + W_d/2$ versus ψ for 24 TMs [112]. (e) The outer-electrons (N_{oe}) versus ψ for monoxides (MO) and perovskite oxides (ABO_3) [152]. (f) The *p*-band center (*p*-band SO) versus ψ for ABO_3 [155]. Reproduced from [34]. CC BY 4.0.

that $E^{(0)} \propto \frac{X_m - X}{X_m} n_0$ (n_0 is denoted as the homogenous electron density). Note that Nørskov *et al* [32] utilized the zero-order approximation to rationalize the slope term of the LSR as discussed above, although the slope of the LSR is not simply determined by the zero-order approximation. Since the bond number of adsorbates can only be integer, we introduce a perturbation effect induced by the adsorbed atom to the electron density, as $\Delta n = n_0/(X_m + 1)$. Then the first-order term is as follows,

$$E^{(1)} \propto \frac{(X_m - X)\, n_0}{X_m\,(X_m + 1)} = (X_m - X)\, n_0 \left[\frac{1}{X_m} - \frac{1}{X_m + 1}\right] \tag{47}$$

Therefore, as long as the considered adsorbates are not particularly polarizable, the adsorption energy E_{ad} should obey the relation as,

$$E_{ad} = E^{(0)} - E^{(1)} \propto \frac{X_m - X}{X_m + 1} n_0 \tag{48}$$

Equation (48) rationalizes the prefactor of the electronic term in equation (44). Actually, it is the determination of equation (48) that generates the slope of the LSR which is expressed by $\frac{X_m - X}{X_m}$, as the results in [32], which we will derive in the following.

The prefactor of the coordination term $\frac{X+1}{X_m+1}$ in equation (44) can be explained by the bond-order conservation theory [171, 172]. From the view of substrate, the adsorption energy is proportional to the coordination of active sites, which means that the saturated-bond number of active center controls the binding strength to adsorbates. This scheme also holds for adsorbates so that the adsorption energy is proportional to the saturated-bond number of adsorbates.

The constant θ term in equation (44) is a parameter related to adsorbates and is most likely attributed to the coupling between the valence of adsorbates and the *sp*-states of the metals in terms of the *d*-band model. We also find that θ is strongly related to the bond energy between the atom binding to surface and its coordination atoms in adsorbates (see figure 20).

2.7.3. Implications

The intrinsic model incorporates the effects of electronic and geometric structures of substrates and adsorbates together to determine adsorption, thereby providing a novel physical picture for adsorption. This model identifies the previous assumption that the electronic and geometric structures for substrates are independent of each other in determining adsorption and gives an intrinsic expression of adsorption energy [33, 70]. Hence, the intrinsic model can automatically derive the LSR and its generalized form [32, 33], uncovers the efficiency in modulating the adsorption energy and reaction energy, and deduces naturally the thermodynamic limitations of catalysis. All these implications pave the ways for applying the intrinsic model in catalysis.

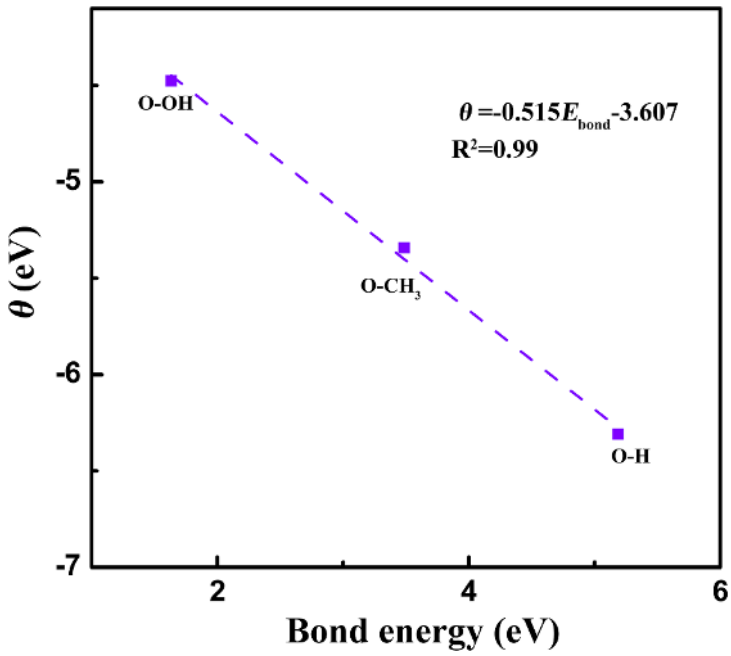

Figure 20. The θ in equation (44) of the species binding via oxygen versus the bond energy between the oxygen atom and its coordination atoms in adsorbates (O–O bond for OOH, O–C bond for OCH_3 and O–H bond for OH). Reproduced from [34]. CC BY 4.0.

Remarkably, the intrinsic model can derive the LSR and its generalized form automatically. For atoms (A) and their partially hydrogenated species (AH_x) on TM surfaces, one obtains that in terms of equation (44):

$$E_{\mathrm{ad}}^{\mathrm{A}} = 0.1 \times \frac{X_{\mathrm{m}}}{X_{\mathrm{m}}+1} \times \psi + b^{\mathrm{A}} \tag{49}$$

$$E_{\mathrm{ad}}^{\mathrm{AH}_x} = 0.1 \times \frac{X_{\mathrm{m}}-X}{X_{\mathrm{m}}+1} \times \psi + b^{\mathrm{AH}_x} \tag{50}$$

The actual bonding number for atoms (A) and their partially hydrogenated species (AH_x) are 0 and x respectively. Combining equations (49) and (50), one can naturally derive the correlation between the two species as,

$$\begin{aligned} E_{\mathrm{ad}}^{\mathrm{AH}_x} &= \frac{X_{\mathrm{m}}-X}{X_{\mathrm{m}}} \times E_{\mathrm{ad}}^{\mathrm{A}} + \left[b^{\mathrm{AH}_x} - \frac{X_{\mathrm{m}}-X}{X_{\mathrm{m}}} \times b^{\mathrm{A}} \right] \\ &= \gamma E_{\mathrm{ad}}^{\mathrm{A}} + \left(b^{\mathrm{AH}_x} - \gamma b^{\mathrm{A}} \right) \\ &= \gamma E_{\mathrm{ad}}^{\mathrm{A}} + \xi \end{aligned} \tag{51}$$

this is exactly the LSR, as equation (36). Moreover, with equations (44) and (51), the offset of the LSR is as follows,

$$\begin{aligned} \xi &= b^{\mathrm{AH}_2} - \gamma b^{\mathrm{AH}_1} \\ &= 0.2 \times \frac{X_2 - X_1}{X_{\mathrm{m}} - X_1} \times \overline{CN} + \left[\theta^{\mathrm{AH}_2} - \frac{X_{\mathrm{m}} - X_2}{X_{\mathrm{m}} - X_1} \times \theta^{\mathrm{AH}_1} \right] \end{aligned} \tag{52}$$

It is noteworthy that CN_{u} and $\overline{CN}$ are almost identical in describing the extended surfaces. Clearly, the offset ξ should scale linearly with the coordination of surface atoms, namely we theoretically derive the generalized form of the LSR [33]. Moreover, the generalized LSR only demonstrates that the offset is related to the coordination of surface atoms but cannot give the accurate expression for the prefactor of the coordination term and the constant term. Our scheme remedies this shortcoming and provides a general expression for the offset of the LSR, proposing that the prefactor of the coordination term is determined by the bonding numbers of the central atoms of the two species (see equation (52)). The prefactors of $\overline{CN}$ is predicted to be ~0.10 for the LSR of OH vs. O, OOH vs. O and OCH_3 vs. O since $X_1 = 0$, $X_2 = 1$ and $X_{\mathrm{m}} = 2$

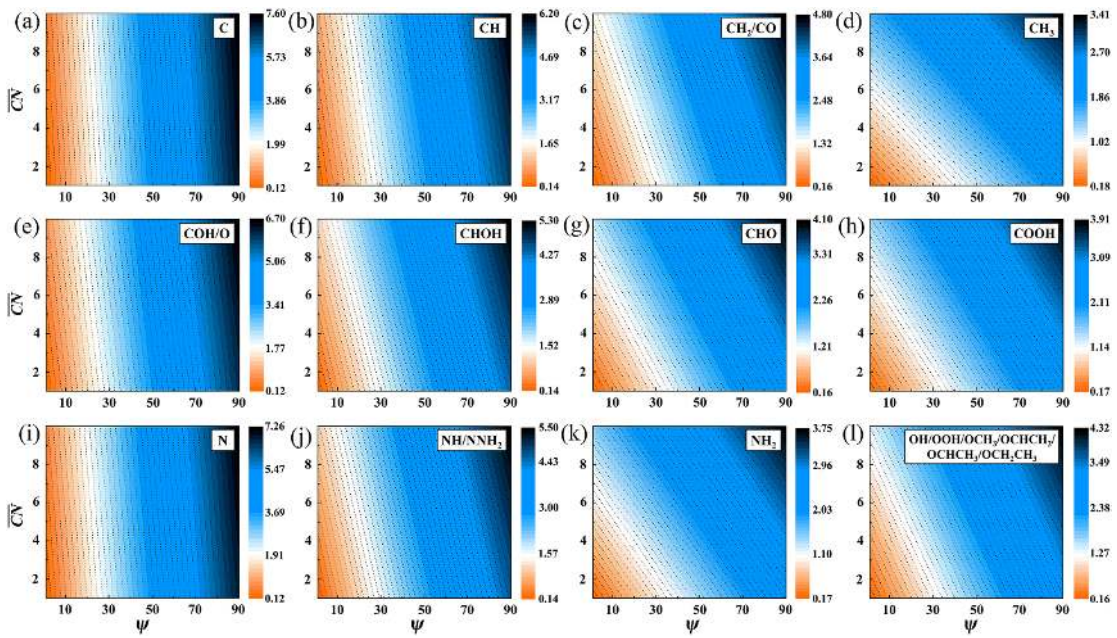

Figure 21. The efficiency in modulating the adsorption energy by means of the electronic descriptor ψ and the generalized coordination number ($\overline{CN}$). (a) C atom. (b) CH radical. (c) CH_2 radical or CO molecule. (d) CH_3 radical. (e) COH radical or O atom. (f) CHOH radical. (g) CHO radical. (h) COOH radical. (i) N atom. (j) NH radical or NNH_2 radical. (k) NH_2 radical. (l) OH radical, OOH radical, OCH_3 radical, $OCHCH_2$ radical, $OCHCH_3$ radical, or OCH_2CH_3 radical. Reproduced from [34]. CC BY 4.0.

in equation (52). This is in good agreement with the direct DFT-fitted results (0.08–0.11) [33]. We also identify that the constant term of the coordination-determined relation is governed by the θ term of the two adsorbates and is affected by their actual bonding numbers. Overall, the intrinsic model can derive the LSR and its generalized form naturally by providing a more general expression, reflecting the solid physical–chemical foundations.

With the intrinsic model, one can engineer the adsorption energy for a given adsorbate by modulating the electronic and geometric structures of substrates respectively. According to equation (44), the prefactors of electronic and geometric terms dominate the efficiency of the electronic and geometric determinants in engineering the adsorption energy, namely it is the adsorbates that control the efficiency in modulating the adsorption energy. Figure 21 shows the efficiency in modulating the adsorption energy for species binding via C, N and O. Clearly that the electronic descriptor ψ is more effective in unsaturated atoms like C and N, but the geometric descriptor $\overline{CN}$ becomes more important in saturated atoms like CH_3, COOH and NH_2. This insight paves the way for effectively engineering the adsorption energy to obtain the optimal properties. Since the ψ of TMs and NPs are distributed discretely from 0 to 100, thus alloying allows one to fill in the gap between different TMs and NPs.

This scheme also uncovers the efficiency for modulating the reaction energy. The adsorption energy difference of any pair of adsorbates with the same central atom is as follows,

$$\Delta E_{\mathrm{ad}} = 0.1 \times \frac{X_2 - X_1}{X_{\mathrm{m}} + 1} \times \psi - 0.2 \times \frac{X_2 - X_1}{X_{\mathrm{m}} + 1} \times \overline{CN} + \theta'_{1,2} \tag{53}$$

clearly, the bonding number difference of the central atom between two species determines the adsorption energy difference. To maximize the modulating efficiency, ψ and $\overline{CN}$ should vary oppositely. We find that the predicted prefactors of ψ and $\overline{CN}$ of equation (53) are in good agreement with the direct DFT calculations for CO_2RR (see table 5) [18]. For instance, the predicted prefactors of ψ and $\overline{CN}$ of equation (53) for CO → HCO are merely 0.01 and 0.02, corresponding to a small variation for the energetics of CO → HCO as the nature or structure of surfaces changes. This is consistent with the literature findings [14, 18], where the limiting potential of CO protonation exhibits a nearly horizontal line over TMs. A special case is that with $X_1 = X_2$, the adsorption energy difference is always constant regardless of the electronic and geometric structures of substrates, leading to a limitation that it is impossible to engineer the reaction energy through changing the nature or the morphology of surface sites for any pathways involving a pair of intermediates with the same bonding numbers of the central atom. This exactly corresponds to the known thermodynamic limitations of ORR [33, 180]. Moreover, our scheme suggests that the associative pathway of NRR is

Table 5. Comparison between the predicted and DFT-calculated prefactors (ψ and $\overline{CN}$) [34] in equation (53) for five reaction steps of CO_2RR on transition-metal (TM) surfaces. The DFT-calculated results are extracted from [18].

	Prefactors of ψ		Prefactors of $\overline{CN}$	
Reaction steps	Predicted	Calculated	Predicted	Calculated
CO → COH	−0.027	−0.011	0.054	—
COH → C	−0.013	−0.012	0.026	—
CO → CHO	0.010	0.008	−0.020	—
COOH → CO	−0.013	−0.010	0.026	—
CH → CH_2	0.020	0.019	−0.040	—

restricted by the thermodynamic limitations since NH and NNH_2 possess the same bonding numbers, while the dissociative pathway is beneficial for improving the NRR. Note that there exist some outliers that deviate from the guiding line such as Cu(111) and Cu(211) for species binding via carbon and Au(111), Au(211), Au(100) and Cu(100) for species binding via oxygen shown in figures 16 and 17, breaking the scaling law. These outliers could be used to break the inherent adsorption thermodynamics to reach optimal performances.

Overall, with the intrinsic model, one can naturally deduce the LSR and its generalized form, recognize the *d*-band model and the generalized coordination number model, and uncover the efficiency and limitations in modulating the adsorption energy and reaction energy, thereby enabling the potential applications in catalysis.

3. Applications

We have systematically discussed the electronic and geometric determinants of adsorption and enumerated several crucial models, which have profound significance for applications in many fields especially in catalysis. In the following, we specifically introduce some typical applications of these models in catalysis, such as ORR, CO_2RR and NRR, compare their performances and indicate the direction for screen catalysts with optimal properties.

3.1. Oxygen reduction reaction

ORR, an important electrochemical reaction that plays a key role in alternative energy conversion and storage devices such as fuel cells and metal-air batteries [195–200]. It has been identified that a variety of materials exhibit high activity towards ORR including pure TMs and NPs [193, 194], TM oxides [149, 150], alloys [16] and SACs [168]. Therefore, finding the proper descriptors to explain the activity trends of ORR for these materials has been a long-term goal in the fields.

There have been some descriptors for describing the activity trends of ORR for TMs, Pt_5M-series alloys and NSAs. Norskov *et al* [193, 194, 201] demonstrate that the binding energy of O (E_b [O]) can well describe the activity trends of ORR for TMs as shown in figure 22(a). Clearly, pure Pt is the best catalyst for ORR among TMs which is in agreement with experiments. Pt_5M, in which M represents the alloying elements with La-series metals and Ca, is one of crucial members in Pt-based catalysts [16, 20]. The previous work by Escudero-Escribano *et al* [202] has correlated the activity of ORR for Pt_5M with the lattice parameter, obtaining a volcano-shaped relation shown in figure 22(b). They propose that Pt_5Tb and Pt_5Gd are the best catalysts for ORR among considered substrates, which bind OH neither too weak nor too strong. Actually, the lattice constant reflects the strain effects of Pt overlayer on Pt_5M: compressive strain generates the downward shift of the *d*-band center of Pt, resulting in the reduction of the binding strength of O-species and the enhancement of the activity of ORR [203, 204]. NSAs represent an important family of alloy catalysts, where the guest atoms on top or second layer significantly change the electronic properties of surfaces [20, 135–137]. The activity of ORR as a function of adsorption energy of OH (E_{OH}) for NSAs is illustrated in figure 22(c), where the substrate is Pt(111) surface and the A_xB_{3-x}/A_yB_{3-y} formulation represents the thin film of the first and second atomic layer of the NSAs [205]. The volcano curve indicates that $Pt_3/PtAu_2$ performs best among considered NSAs since it locates near to the peak of the volcano.

We find that the electronic descriptor ψ can give a good description for the activity towards ORR among all the above discussed substrates [206]. Figure 22(d) plots the volcano curve of the activity of ORR against ψ for pure TMs [194]. Remarkably, the left leg of the volcano exhibits two branches, dividing the TMs into two groups. The first group (the upper scaling line) includes the metals that all comply with the *d*-band model with ε_d independent on W_d, while the second group (the lower scaling line) represents the metals with ε_d correlated strongly to W_d [112]. As has been mentioned above, the electronic descriptor ψ can well capture the different role of W_d for TMs (see figure 19(a)). The volcano behavior implies that Pt and Pd are the

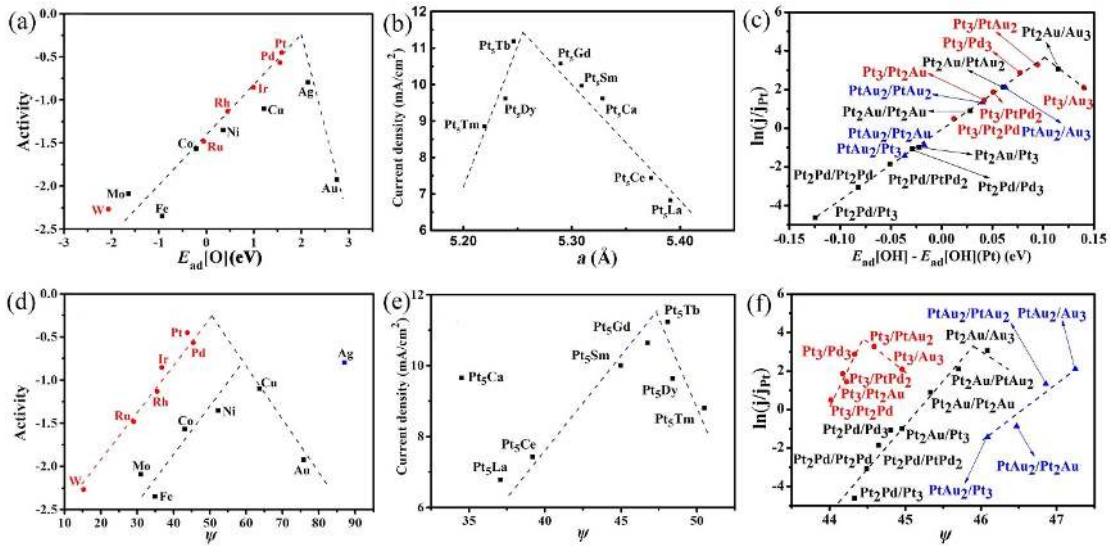

Figure 22. The traditional models and the intrinsic model in describing the activity of ORR for transition metals (TMs), Pt_5M-alloys and near-surface alloys (NSAs). (a) The volcano curve of the activity of ORR versus the binding energy of O E_{ad} [O] for pure TMs [194]. (b) The volcano curve of the activity of ORR versus the lattice parameter a for Pt_5M-alloys [202]. (c) The volcano curve of the activity of ORR versus the binding energy of OH relative to pure Pt E_{ad} [OH] − E_{ad} [OH](Pt) for NSAs [205]. (d)–(f) The volcano curve of the activity of ORR versus the electronic descriptor ψ for pure TMs [194] (d), Pt_5M-alloys [202] (e) and NSAs [205] (f). (a), (c), (d)–(f) are reprinted with permission from [206]. Copyright (2020) American Chemical Society.

optimal catalysts towards ORR among considered TMs. There is still room to design catalysts to further reach the volcano peak. These results are consistent with the traditional adsorption-energy based volcano curve in figure 22(a). One of the advantages of the intrinsic model is that it can effectively screen alloy catalysts by only considering the first-group metals since catalysts always obey the electronic properties of the dominant metal in alloys, leading to a limitation in enhancing the activity for the second-group metals expect Cu, Ag and Au. In fact, the experiments and DFT calculations have proved this point: the activity of Ir alloys approaches that of pure Pt after alloying Ir with Co [207]; Pt_5M family alloys are known to be more reactive than pure Pt [208]. Moreover, there are no alloys whose dominant metal comes from the second-group metals that are as active as pure Pt for ORR. Figure 22(e) plots the volcano curve between the activity of ORR and electronic descriptor ψ for Pt_5M [202]. Note that the f-electrons of La-series metals are taken into consideration, namely the S_v term in equation (45) including 4f-, 5d- and 6s-electrons. The reason of the deviation from the guiding line for Ca is attributed to the different properties of Ca compared with La-series metals: there is no f-electron for Ca. Clearly, Pt_5Tb stands close to the peak of the volcano curve, serving as an optimal catalyst among Pt_5M for ORR. It is noteworthy that the activity of Pt_5Dy is substantially less than that of Pt_5Tb despite the similar value of ψ (53.46 for Pt_5Dy vs 52.71 for Pt_5Tb), which is due to the fact that the right leg of the volcano curve decreases dramatically compared to the left one. This implies that it is more convenient to choose the metals belonging to the volcano's left leg to further design advanced Pt_5M-based catalysts for ORR. Moreover, this result also implies that ψ captures the strain effects of Pt_5M alloys, namely it is the intrinsic valence and electronegativity of Pt and La-series metals that control the strain effects of Pt overlayer and the activity of ORR. The activity of ORR as a function of ψ for NSAs is illustrated in figure 22(f) [205], where the volcano curve exists. Remarkably, ψ divides the NSAs into three classes compared to the adsorption-energy based descriptors in figure 22(c), exhibiting three different volcano-type behaviors. It is intriguing that the classification is based on the components of top surface layer atoms, and the efficiency of modulating the activity of alloying is in the order $Pt_3 > Pt_2M > PtM_2$ for NSAs in the left leg of the volcano due to the different slope. Therefore, one obtains a strategy to design optimal NSA catalysts: pure Pt is selected as the first-layer metal of NSA and adjusting the components of the second layer with a bit smaller ψ than that of $Pt_3/PtAu_2$ on Pt(111) surface. Overall, the electronic descriptor ψ not only characterizes the activity trends of ORR for pure TMs, Pt_5M-series alloys and NSAs but also indicates the strategy to screen optimal catalysts for ORR.

In addition to the determination of the optimal materials for catalysts, it is also necessary to find out which structure or site is more prior, namely the geometric effects must be taken into account. In the case of ORR, the first proton-electron transfer (O_2 is transferred into *OOH) and the last proton-electron transfer (*OH is transferred to H_2O) are the two potential-determining steps [194]. Figure 23 plots the reaction energies of these two steps as a function of the generalized coordination number $\overline{CN}$ [26]. The typical

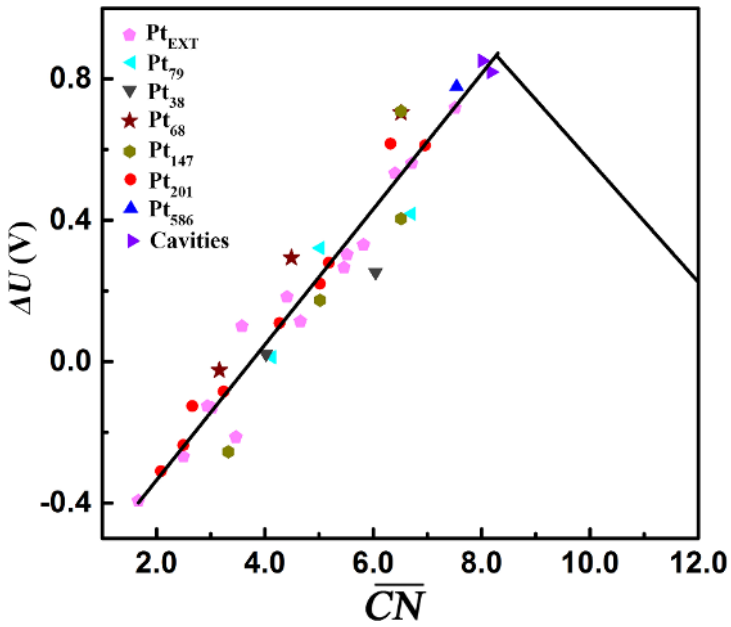

Figure 23. The volcano curve of the activity of ORR versus the generalized coordination number ($\overline{CN}$) on Pt extended surfaces and Pt-nanoparticles (NPs). The data are adapted from [26].

volcano curve indicates that the optimal activity should have geometric sites with $\overline{CN} \approx 8.3$. Clearly, the optimal sites should possess more neighbors than (111) terrace whose $\overline{CN}$ is equal to 7.5 in extended surfaces and sufficiently large NPs. Although some sites possess larger CN_u than (111) terrace such as the bottom of (100) step sites ($CN_u = 10$) and the bottom of (111) step sites ($CN_u = 11$), their $\overline{CN}$ are 8.75 and 9.5 respectively, exceeding the predicted optimal value. In addition, these sites normally have weak activity due to the steric hindrance and adsorbates on these sites are inclined to diffuse to the neighboring uncoordinated sites. Thus, an effective method to reach the optimal activity is to artificially create some defective sites with $\overline{CN}$ close to 8.3. In figure 23, Calle-Vallejo *et al* [26] propose two kinds of cavities whose $\overline{CN}$ are 8.0 and 8.17 respectively. Theoretically, these two cavities should possess good catalytic properties. This prediction has been confirmed by experiments [26]. The defective Pt electrodes can increase the activity 3.5 times compared to Pt(111) surface, demonstrating that the geometric-descriptor based volcano curve is indeed reasonable to screen catalysts with optimal sites. Actually, this geometric effect to design optimal facets is involved in the intrinsic model [34] as seen in equation (44).

We also identify that the electronic descriptor ψ can be used to elucidate the activity of ORR for SACs [206]. Figures 24(a) and (b) plot the adsorption energies of O (E_{ad} [O]) against ψ for single atoms embedded in pristine graphene and N-doped graphene (M–C_4–G and M–N_4–G) [168]. E_{ad} [O] shows a broken-line behavior with ψ, with Cr and V as the turning points for M–C_4–G and M–N_4–G respectively. The different turning points for M–C_4–G and M–N_4–G obey the octet rule of 8-electrons structure: the unpaired electrons are 2 and 3 for C and N atoms, corresponding to the valence of $3d^5 4s^1$ for Cr and $3d^3 4s^2$ for V. Notably, three branches are found out from figures 24(a) and (b) where Sc, Ti and V systems stand at the left branch and the rest SACs locate at the right-higher or right-lower branch. This classification is related to the element period of the involved TMs in SACs. The third period TMs (Cr, Mn, Fe, Co, Ni and Cu) constantly locate at the right-lower branch while the fourth period TMs (Mo, Ru, Rh and Pd) are in the range of the right-higher branch. Intriguingly, N-doping affects the behavior of the fifth period TMs such as Pt, Ir and Os: Pt and Ir (Os) belong to the right lower (higher) branch for M–C_4–G, while they are classified into the right higher (lower) branch for M–N_4–G. The special case for Au and Ag is due to the deep-lying *d*-bands relative to the Fermi level. Moreover, the crystal structures of doped TM atoms on SACs in bulk also contribute to distributions of the SACs on the relation of E_{ad} vs ψ. The adsorption energies of O on SACs increase as the bulk structures of the doped TM atoms change with the order of bcc < hcp < fcc. Figures 24(c)–(f) shows the onset potential of ORR against ψ on SACs. One remarkable feature is that the left branch TMs are integrated into the right-lower one and the whole trends show two volcano-type relations. Rh and Pt for M–C_4–G and Co and Fe for M–N_4–G locate near the peak of the volcano curve, thus are the optimal catalysts for ORR among the considered SACs. The volcano curve provides guidance to design catalysts for SACs: one should choose the right branch candidates in figures 24(a) and (b) to serve as the catalysts of ORR.

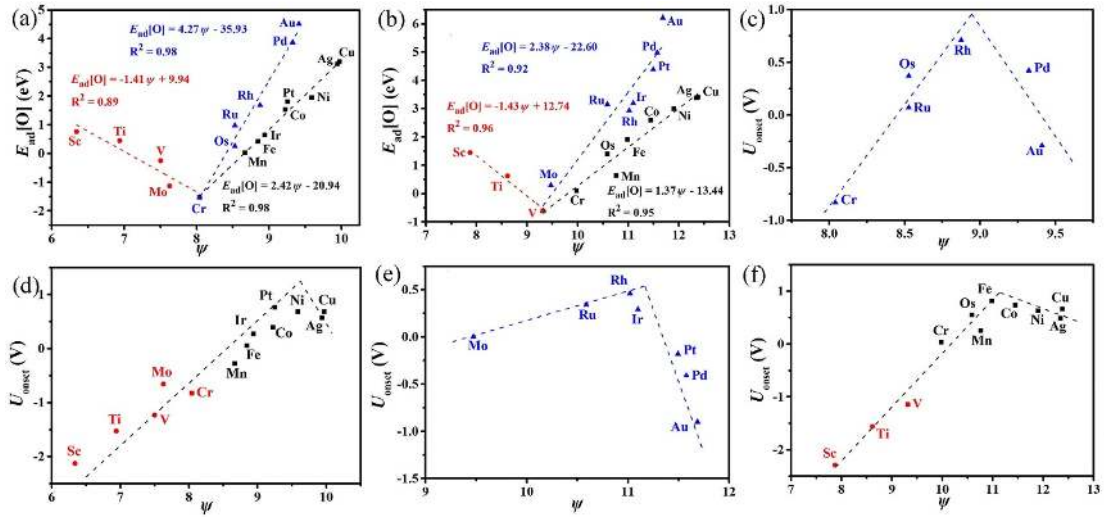

Figure 24. The intrinsic model in describing the activity of ORR for single-atom catalysts (SACs). (a), (b) The adsorption energies of O versus the electronic descriptor ψ on M–C_4–G (a) and N–N_4–G (b) [168]. (c), (d) The volcano curve of the activity of ORR versus ψ on M–C_4–G [168]. (e), (f) The volcano curve of the activity of ORR versus ψ on M–N_4–G [168]. Reprinted with permission from [206]. Copyright (2020) American Chemical Society.

Overall, the electronic descriptor ψ can elucidate the volcano-type trend of activity of ORR for pure TMs, NPs, Pt_5M-alloys, NSAs and SACs. Namely ψ is a universal descriptor in describing the catalytic properties of ORR.

3.2. CO_2 reduction reaction

As a key reaction for producing fuels and chemicals that matter to the renewable energy, CO_2RR has attracted extensive attention. Normally, CO_2RR contains four essential pathways which generate CO, HCOOH, CH_4/CH_3OH and H_2 respectively [209, 210]. Numerous intermediates are included in these four pathways such as C-terminated species, O-terminated species and H atoms, which are also important in understanding many other reactions. Moreover, CO_2RR has been performed both experimentally and theoretically on TMs and NPs [18, 27, 28], TM oxides [211, 212], alloys [213, 214] and SACs [189, 215, 216]. Thus, it is crucial to identify effective descriptors to characterize the selectivity of these pathways for CO_2RR on these substrates.

The previous works have proposed some descriptors to explain the trends of activity towards CO_2RR. Nørskov *et al* [14] use the binding energy of CO as a descriptor to elucidate the activity trend of CH_4 production since the protonation of CO is the rate-determining step, identifying that Cu serves as the optimal catalyst among considered TMs (see figure 25(a)). The adsorption energy of H* is utilized to clarify the trends of hydrogen reduction reaction (HER) over TM surfaces [18] (see figure 25(b)). Moreover, the adsorption energy of COOH* is considered as the descriptor to explain the trend of CO production by Jaramillo *et al* [217] since the adsorbed COOH* is the key intermediates for CO production, proposing that Au should be the optimal catalyst since it stands at the peak of the volcano (see figure 25(c)). They also find that the *HCOO binding energy could serve as a descriptor for the activity of CO_2RR to $HCOO^-$. Sn appears close to the top of the volcano and acts as the optimal catalyst (see figure 25(d)). Although these descriptors rationalize the activity trends of the corresponding pathways, they can hardly reveal the entire selectivity of CO_2RR since the four pathways are competitive and coupled. Note that the binding energy of CO has been considered as a universal descriptor to characterize the activity towards the entire CO_2RR, unfortunately, the underlying basis is unclear.

The intrinsic model provides a new picture in describing the activity of CO_2RR [218]. Figures 26(a) and (b) exhibit the theoretical onset potentials for four competitive pathways (CO, HCOOH, CH_4/CH_3OH and H_2 formation) versus the electronic descriptor ψ on both close-packed and stepped surfaces [18, 219]. Clearly, the volcano-shaped trends can be observed for all four competitive pathways. This is encouraging, since ψ could compare the activities for multiple pathways simultaneously which is inaccessible or controversial for the traditional adsorption-energy based descriptors. The intrinsic model suggests that Cd is inclined to produce HCOOH, while Pt, Pd and Ti favor H_2 production. As Cu locates at the turning point or the peak of the volcano for the CH_4/CH_3OH production, Cu serves as the optimal catalyst among considered TMs. Figure 26(c) plots the correlation between the experimental onset potential and ψ [220]. The volcano-shaped behavior of the experimental onset potential further confirms the applicability of this

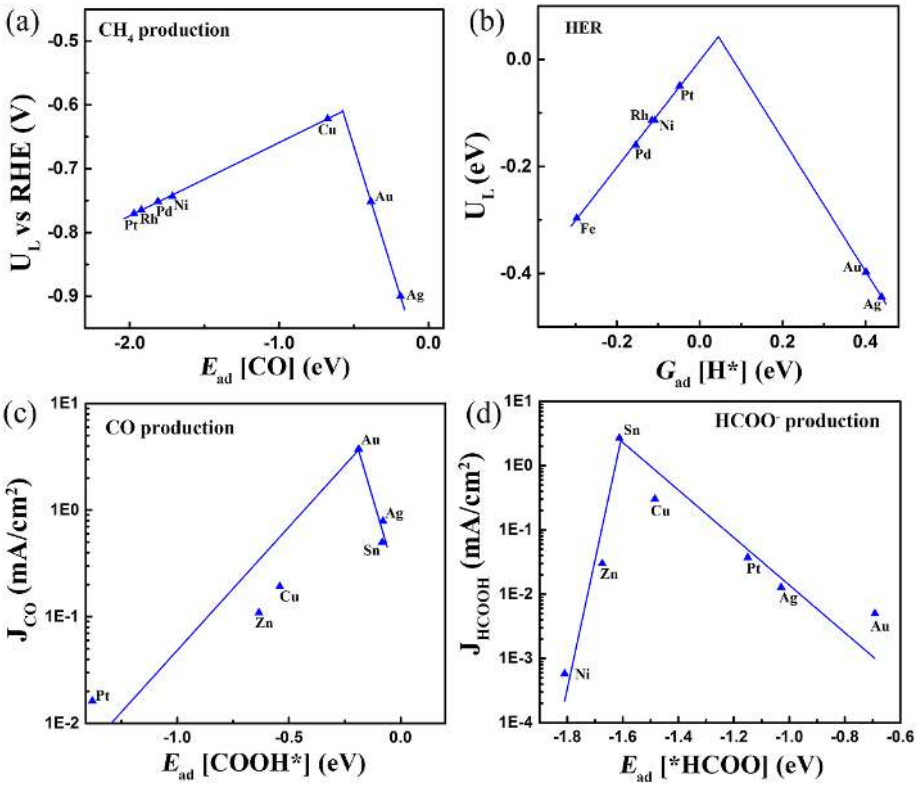

Figure 25. The traditional models in describing the activity of CO_2RR for transition metals (TMs). (a) Limiting potential (U_L) of the CH_4 production versus the binding energy of CO for TMs. The data are adapted from [14]. (b) U_L of the HER versus the adsorption free energy of *H for TMs. The data are adapted from [18]. (c) The CO partial current at −0.9 V vs RHE versus the binding energy of COOH* for TMs. (d) The $HCOO^-$ partial current at −0.9 V vs RHE versus the binding energy of *HCOO for TMs. The data are adapted from [217].

scheme, where Cu is inclined to produce CH_4/CH_3OH as it stands at the turning point of the volcano and Au shows the optimal performance towards the overall CO_2RR. By comparing the experimental trends with theoretical results [18], one can easily obtain that the experiments in [220] are performed on close-packed surfaces of TMs since the trend of CH_4/CH_3OH production of the experiments is close to the theoretical prediction on close-packed surfaces. The trends in figure 26(c) can also be utilized to guide the selectivity of CO_2RR. For TMs with $\psi < 76$, the selectivity of CH_4/CH_3OH is enhanced with the decreasing ψ; for TMs with $\psi > 76$, the increase of ψ from 76 improves the selectivity of CO and other products like HCOOH. Experimental partial current densities for the overall CO_2RR at −0.8 V and for the CO and HCOOH production at −0.9 V are correlated with ψ shown in figures 26(d) and (e) [217, 220], where the volcano curves emerge again. Au has the highest activity for the overall CO_2RR at −0.8 V. For the CO and HCOOH production at −0.9 V, Au and Cu possess the highest activity respectively. Similar to the relation of onset potential and ψ, ψ can characterize the selectivity of the CO and HCOOH production at −0.9 V in experiments: TMs with $\psi < 64$ are prone to produce HCOOH while TMs with $\psi > 64$ are inclined to generate CO. The experimental exchange currents of HER are correlated with ψ in figure 26(f). The clear volcano curve can be observed and Pt locates at the peak of the volcano, serving as the optimal catalyst for HER among considered TMs [221, 222]. The unreactive TMs such as Cu, Au and Ag stand at the right leg of the volcano, while the reactive TMs locate at the left leg. Note that the left leg of the volcano is divided into two branches, which is consistent with the conventional adsorption-energy based descriptors. This is due to the difference of the transfer coefficient in one electron transfer reaction. All these findings demonstrate that the electronic descriptor ψ can well clarify the activity and selectivity of CO_2RR.

Figure 26(g) exhibits the theoretical onset potential for CO, CH_4/CH_3OH and H_2 production as a function of ψ on M–N_4–G SACs [215]. The clear volcano curves for all three competitive reduction pathways verify that ψ is indeed reasonable to elucidate the activity trend of CO_2RR for M–N_4–G SACs. Note that Rh–N_4–G and Ir–N_4–G possess the highest activity for all three pathways and serve as the optimal catalysts. The left leg of these volcano curves shows clear selectivity towards CO_2RR, while the selectivity towards CO_2RR for the right leg is comparable. It is clear that Rh–N_4–G and Ir–N_4–G are inclined to produce CO at a low onset potential, Fe–N_4–G and Co–N_4–G produce CO and/or H_2 with an overpotential of −0.4 V, while a high overpotential is required for Ni–N_4–G to CO production. The experimental activity volcano curve of

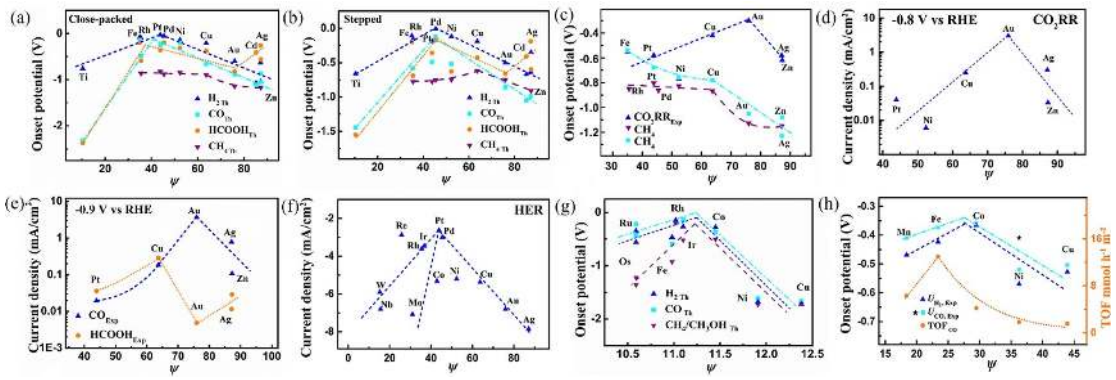

Figure 26. The intrinsic model in describing the activity of CO_2RR for transition metals (TMs) and single-atom catalysts (SACs). (a), (b) The theoretical onset potential versus ψ for CO, CH_4/CH_3OH, HCOOH, and H_2 production on close-packed (a) and stepped TM surfaces (b) [18, 219]. (c) The experimental onset potential versus ψ for the total CO_2RR (to any product) and CH_4/CH_3OH production [220], along with the theoretical onset potential versus ψ for CH_4/CH_3OH production on TM close-packed surfaces [18]. (d) The current density versus ψ for the total CO_2RR on TM surfaces [220]. (e) The experimental current density versus ψ for CO and HCOOH production on TM surfaces [217]. (f) The experimental current density versus ψ for HER on TM surfaces [221]. (g) The theoretical onset potential versus ψ for CO, CH_4/CH_3OH, and H_2 production on $M–N_4–G$ SACs [215]. (h) The experimental onset potential versus ψ for CO and H_2 production and turnover frequency (TOF) versus ψ for CO on $M–N_4–G$ SACs [223]. Reprinted with permission from [218]. Copyright (2020) American Chemical Society.

CO_2RR against ψ for $M–N_4–G$ SACs is illustrated in figure 26(h) [223], which is in good agreement with the theoretical predictions. The experimental order of catalytic activity also fulfills the theoretical prediction: $Co–N_4–G > Fe–N_4–G > Mn–N_4–G > Cu–N_4–G > Ni–N_4–G$. Moreover, figure 26(h) demonstrates that both the volcano relationship between the activity of H_2 production and ψ and the order of the catalytic activity for H_2 production on $M–N_4–G$ SACs exhibit excellent consistency between theoretical predictions and experimental measurements. Hence, ψ can be used to clarify the catalytic properties of CO_2RR for both TMs and SACs, exhibiting good generality [218].

3.3. Nitrogen reduction reaction

NH_3 is one of the most promising carbon-free alternative energy storage materials with a high weight fraction of hydrogen [224, 225]. Traditional Haber–Bosch process to produce NH_3 is incomplete and requires harsh conditions [226], making NRR an alternative strategy for green and sustainable production of NH_3 due to the environmental-friendly character and mild reaction conditions. The previous studies have demonstrated that TMs [13], TM oxides and sulfides [227, 228], SACs and bi-atom catalysts (BACs) [229, 230] can serve as the potential catalysts for NRR. Hence, effective descriptors should be made to elucidate the activity trends towards NRR for these catalysts.

For NRR, the volcano curve has been found as a function of binding energy of nitrogen to the TM close-packed and stepped surfaces seen in figures 27(a) and (b) [231]. The volcano curve illustrates that Ru is the optimal catalyst towards NRR. The intrinsic model can also be utilized to elucidate the activity of NRR. Figures 27(c) and (d) exhibit the volcano curve that is obtained by plotting the limiting potential for NRR versus the electronic descriptor ψ for TMs on both close-packed and stepped surfaces [231]. Remarkably, the peak of the volcano curve for stepped surfaces shifts rightwards relative to that for close-packed surfaces, which is attributed to the different determining steps for the left leg of the volcano. The left leg on close-packed surfaces corresponds to the NH* protonation to form NH_2* while that on stepped surfaces represents the proton transfer from NH_2* to NH_3. Overall, Ru should be the optimal catalyst for NRR since it stands close to the top of the volcano curve, which is in good agreement with the traditional adsorption-energy based descriptors. It is noteworthy that all considered TMs exhibit higher activity on stepped surfaces than on close-packed surfaces except Re, following the bond-order conservation rule that the surfaces with smaller coordination number are more inclined to form new bonds. The reason for the abnormality of Re is due to the fact that the adsorption energies of *NH_2 and *NH for Re are too strong, leading to the lower limiting potential. Similar result has been made by Wang *et al* [232] that Mo(110) preferred orientation and NP-clustering morphology were beneficial for NRR compared with Mo foil. This scheme also allows one to uncover the surface selectivity for NRR: close-packed surfaces possess higher activity for TMs with $25 < \psi < 36$ while stepped surfaces are more favorable for TMs with $29 < \psi < 53$. This provides beneficial guidance to design optimal catalysts for NRR. Note that the onset potential of HER is always larger than that of NRR (see figure 27), namely the activity of HER is higher than NRR. Hence, it is crucial to suppress HER in order to improve the NRR.

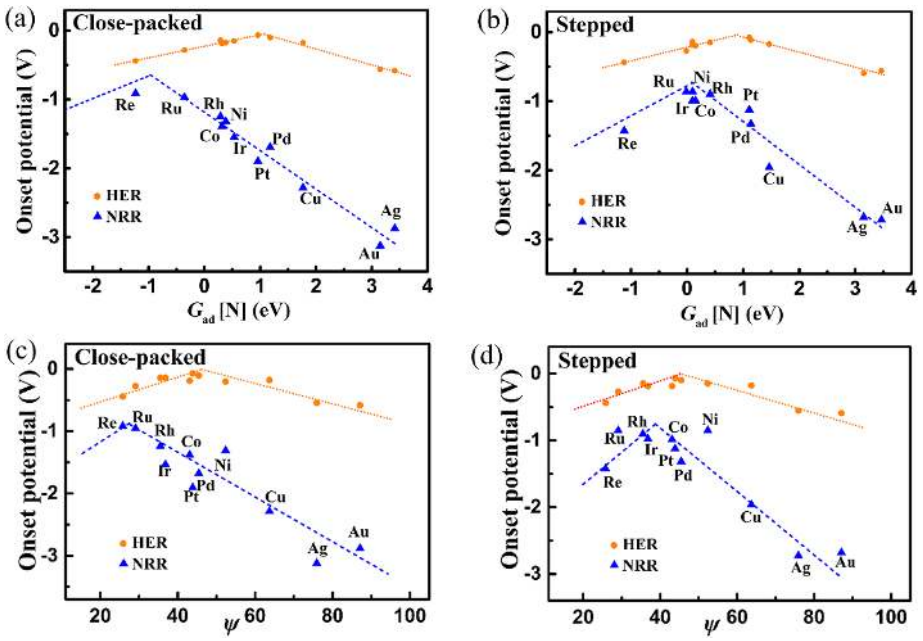

Figure 27. The models in describing the activity of NRR for transition metals (TMs). (a), (b) The activity of NRR versus the adsorption energy of N on TM close-packed (a) and stepped surfaces (b). (c), (d) The activity of NRR and HER versus ψ on TM close-packed (c) and stepped surfaces (d). The data are adapted from [231].

4. Conclusions and remarks

In summary, we introduce several typical models with respect to the electronic and geometric structures of substrates and adsorbates for describing and predicting adsorption energy, including the *d*-band model, the coordination-based models, the LSR and the intrinsic model, and uncover the inherent connection of these models. Among these models, the *d*-band model is original and can serve as a reasonable basis for understanding and rationalizing the other subsequent models, the generalized coordination model is prominent in describing the geometric effect of substrates, and the LSR is effective in correlating the adsorption energies between different adsorbates, while the intrinsic model bridges the gap between the adsorption energies and the readily accessible intrinsic properties of adsorption systems and provides an effective way to capture the local environment effects of active centers. The intrinsic model reflects a relatively comprehensive physical picture for adsorption on solids and is more effective for rapid screening materials with optimal adsorption properties, since it combines the nature of the *d*-band model, the generalized coordination model and the LSR and its parameters can be obtained by table lookup. In particular, the easily accessible parameters of the intrinsic model are convenient for machine learning to do material design. By further applying these models into reactions, such as ORR, CO_2RR and NRR, one can see that the adsorption energy is universal in describing reactivity because of the Sabatier principle, while the intrinsic model is also effective in describing reactivity and selectivity across multiple scale materials. We expect all these models to continue to play an important role in catalytic reactions in the future.

Although the introduced models have been useful and successful in describing the adsorption properties, there are still many challenges that need to be further explored:

(a) There still lacks a complete picture for understanding the strain effects [132, 134] on adsorption. The underlying mechanism of strain effects has to be identified based on the electronic and geometric structures of adsorption systems.
(b) The adsorption properties are not yet quantitatively correlated to the stability of materials, which is crucial in applications, although many attempts have been made in this regard [233, 234]. A model that bridges the gap between the stability and activity of catalysts needs to be uncovered in the future.
(c) The reaction barriers and diffusion barriers of adsorbates are essential for catalysis but are rarely correlated with the properties of adsorbates and substrates. One needs to find out the applicability of Brønsted–Evans–Polanyi relation and seeks a more general picture for correlating thermodynamics and kinetics of reaction [7, 235–237]. Moreover, it is also crucial to build a simple model for describing the friction and energy dissipation during reactions [238–243].

Acknowledgments

The authors are thankful for the support from the Program of the Thousand Young Talents Plan, the National Natural Science Foundation of China (Grant Nos. 21673095, 11974128 and 51631004), the Opening Project of State Key Laboratory of High Performance Ceramics and Superfine Microstructure (SKL201910SIC), the Program of Innovative Research Team (in Science and Technology) in University of Jilin Province, the Program for JLU (Jilin University) Science and Technology Innovative Research Team (Grant No. 2017TD-09), the Fundamental Research Funds for the Central Universities, and the computing resources of the High Performance Computing Center of Jilin University, China.

ORCID iDs

Wang Gao https://orcid.org/0000-0003-0331-2299
Qing Jiang https://orcid.org/0000-0003-0660-596X

References

[1] Brown W A, Kose R and King D A 1998 Femtomole adsorption calorimetry on single-crystal surfaces *Chem. Rev.* **98** 797–831
[2] Ma Z and Zaera F 2006 Organic chemistry on solid surfaces *Surf. Sci. Rep.* **61** 229–81
[3] Kasemo B 2002 Biological surface science *Surf. Sci.* **500** 656–77
[4] Zhang Q, Uchaker E, Candelaria S L and Cao G 2013 Nanomaterials for energy conversion and storage *Chem. Soc. Rev.* **42** 3127–71
[5] Hammer B and Nørskov J K 2000 Theoretical surface science and catalysis—calculations and concepts *Adv. Catal.* **45** 71–129
[6] Sabatier P 1913 *La Catalyse En Chimie Organique* (Paris: Librarie Polytechnique)
[7] Bligaard T, Nørskov J K, Dahl S, Matthiesen J, Christensen C H and Sehested J 2004 The Brønsted–Evans–Polanyi relation and the volcano curve in heterogeneous catalysis *J. Catal.* **224** 206–17
[8] Hammer B and Norskov J K 1995 Why gold is the noblest of all the metals *Nature* **376** 238–40
[9] Hammer B and Nørskov J K 1995 Electronic factors determining the reactivity of metal surfaces *Surf. Sci.* **343** 211–20
[10] Jones G, Bligaard T, Abild-Pedersen F and Nørskov J K 2008 Using scaling relations to understand trends in the catalytic activity of transition metals *J. Phys. Condens. Matter* **20** 064239
[11] Greeley J and Mavrikakis M 2004 Alloy catalysts designed from first principles *Nat. Mater.* **3** 810–5
[12] Studt F, Abild-Pedersen F, Bligaard T, Sorensen R Z, Christensen C H and Norskov J K 2008 Identification of non-precious metal alloy catalysts for selective hydrogenation of acetylene *Science* **320** 1320–2
[13] Skúlason E, Bligaard T, Gudmundsdóttir S, Studt F, Rossmeisl J, Abild-Pedersen F, Vegge T, Jónsson H and Nørskov J K 2012 A theoretical evaluation of possible transition metal electro-catalysts for N_2 reduction *Phys. Chem. Chem. Phys.* **14** 1235–45
[14] Peterson A A and Nørskov J K 2012 Activity descriptors for CO_2 electroreduction to methane on transition-metal catalysts *J. Phys. Chem. Lett.* **3** 251–8
[15] Nørskov J K, Bligaard T, Rossmeisl J and Christensen C H 2009 Towards the computational design of solid catalysts *Nat. Chem.* **1** 37–46
[16] Greeley J, Stephens I E L, Bondarenko A S, Johansson T P, Hansen H A, Jaramillo T F, Rossmeisl J, Chorkendorff I and Nørskov J K 2009 Alloys of platinum and early transition metals as oxygen reduction electrocatalysts *Nat. Chem.* **1** 552–6
[17] Liu X, Xiao J, Peng H, Hong X, Chan K and Nørskov J K 2017 Understanding trends in electrochemical carbon dioxide reduction rates *Nat. Commun.* **8** 15438
[18] Shi C, Hansen H A, Lausche A C and Nørskov J K 2014 Trends in electrochemical CO_2 reduction activity for open and close-packed metal surfaces *Phys. Chem. Chem. Phys.* **16** 4720–7
[19] Tripa C E, Zubkov T S, Yates J T, Mavrikakis M and Nørskov J K 1999 Molecular N_2 chemisorption—specific adsorption on step defect sites on Pt surfaces *J. Chem. Phys.* **111** 8651–8
[20] Kitchin J R, Nørskov J K, Barteau M A and Chen J G 2004 Modification of the surface electronic and chemical properties of Pt(111) by subsurface 3d transition metals *J. Chem. Phys.* **120** 10240–6
[21] Markovic N M and Ross Jr P N 2002 Surface science studies of model fuel cell electrocatalysts *Surf. Sci. Rep.* **45** 117–229
[22] Kibler L A, El-Aziz A M, Hoyer R and Kolb D M 2005 Tuning reaction rates by lateral strain in a palladium monolayer *Angew. Chem. Int. Ed.* **44** 2080–4
[23] Zhang J, Vukmirovic M B, Sasaki K, Nilekar A U, Mavrikakis M and Adzic R R 2005 Mixed-metal Pt monolayer electrocatalysts for enhanced oxygen reduction kinetics *J. Am. Chem. Soc.* **127** 12480–1
[24] Nikolla E, Schwank J and Linic S 2009 Measuring and relating the electronic structures of nonmodel supported catalytic materials to their performance *J. Am. Chem. Soc.* **131** 2747–54
[25] Calle-Vallejo F, Martínez J I, García-Lastra J M, Sautet P and Loffreda D 2014 Fast prediction of adsorption properties for platinum nanocatalysts with generalized coordination numbers *Angew. Chem., Int. Ed.* **53** 8316–9
[26] Calle-Vallejo F, Tymoczko J, Colic V, Vu Q H, Pohl M D, Morgenstern K, Loffreda D, Sautet P, Schuhmann W and Bandarenka A S 2015 Finding optimal surface sites on heterogeneous catalysts by counting nearest neighbors *Science* **350** 185–9
[27] Back S, Yeom M S and Jung Y 2015 Active sites of Au and Ag nanoparticle catalysts for CO_2 electroreduction to CO *ACS Catal.* **5** 5089–96
[28] Back S, Yeom M S and Jung Y 2018 Understanding the effects of Au morphology on CO_2 electrocatalysis *J. Phys. Chem.* C **122** 4274–80
[29] Li H, Li Y, Koper M T M and Calle-Vallejo F 2014 Bond-making and breaking between carbon, nitrogen, and oxygen in electrocatalysis *J. Am. Chem. Soc.* **136** 15694–701
[30] Calle-Vallejo F and Koper M T M 2017 Accounting for bifurcating pathways in the screening for CO_2 reduction catalysts *ACS Catal.* **7** 7346–51
[31] Zhao Z, Chen Z, Zhang X and Lu G 2016 Generalized surface coordination number as an activity descriptor for CO_2 reduction on Cu surfaces *J. Phys. Chem.* C **120** 28125–30

[32] Abild-Pedersen F, Greeley J, Studt F, Rossmeisl J, Munter T R, Moses P G, Skúlason E, Bligaard T and Nørskov J K 2007 Scaling properties of adsorption energies for hydrogen-containing molecules on transition-metal surfaces *Phys. Rev. Lett.* **99** 016105
[33] Calle-Vallejo F, Loffreda D, Koper M T M and Sautet P 2015 Introducing structural sensitivity into adsorption-energy scaling relations by means of coordination numbers *Nat. Chem.* **7** 403–10
[34] Gao W, Chen Y, Li B, Liu S-P, Liu X and Jiang Q 2020 Determining the adsorption energies of small molecules with the intrinsic properties of adsorbates and substrates *Nat. Commun.* **11** 1196
[35] Giustino F 2014 *Materials Modeling Using Density Functional Theory* (Oxford : Oxford University Press)
[36] Sholl D S and Steckel J A 2009 *Density Functional Theory: A Practical Introduction* (New York: Wiley)
[37] Wu X, Kang F, Duan W and Li J 2019 Density functional theory calculations: a powerful tool to simulate and design high-performance energy storage and conversion materials *Prog. Nat. Sci. Mater. Int.* **29** 247–55
[38] Kohn W and Sham L J 1965 Self-consistent equations including exchange and correlation effects *Phys. Rev.* **140** A1133–8
[39] Kohn W 1999 Nobel lecture: electronic structure of matter—wave functions and density functionals *Rev. Mod. Phys.* **71** 1253–66
[40] Perdew J P and Schmidt K 2001 Jacob's ladder of density functional approximations for the exchange-correlation energy *AIP Conf. Proc.* **577** 1–20
[41] Perdew J P, Ruzsinszky A, Tao J, Staroverov V N, Scuseria G E and Csonka G I 2005 Prescription for the design and selection of density functional approximations: more constraint satisfaction with fewer fits *J. Chem. Phys.* **123** 062201
[42] Perdew J P and Wang Y 1992 Accurate and simple analytic representation of the electron-gas correlation energy *Phys. Rev.* B **45** 13244–9
[43] Perdew J P, Burke K and Wang Y 1996 Generalized gradient approximation for the exchange-correlation hole of a many-electron system *Phys. Rev.* B **54** 16533–9
[44] Perdew J P, Burke K and Ernzerhof M 1996 Generalized gradient approximation made simple *Phys. Rev. Lett.* **77** 3865–8
[45] Krukau A V, Vydrov O A, Izmaylov A F and Scuseria G E 2006 Influence of the exchange screening parameter on the performance of screened hybrid functionals *J. Chem. Phys.* **125** 224106
[46] Becke A D 1993 Density-functional thermochemistry. III. The role of exact exchange *J. Chem. Phys.* **98** 5648–52
[47] Zhao Y and Truhlar D G 2006 Density functional for spectroscopy: no long-range self-interaction error, good performance for rydberg and charge-transfer states, and better performance on average than B3LYP for ground states *J. Phys. Chem.* A **110** 13126–30
[48] Zhao Y and Truhlar D G 2006 A new local density functional for main-group thermochemistry, transition metal bonding, thermochemical kinetics, and noncovalent interactions *J. Chem. Phys.* **125** 194101
[49] Zhao Y and Truhlar D G 2008 The M06 suite of density functionals for main group thermochemistry, thermochemical kinetics, noncovalent interactions, excited states, and transition elements: two new functionals and systematic testing of four M06-class functionals and 12 other functionals *Theor. Chem. Acc.* **120** 215–41
[50] Hammer B, Hansen L B and Nørskov J K 1999 Improved adsorption energetics within density-functional theory using revised Perdew–Burke–Ernzerhof functionals *Phys. Rev.* B **59** 7413–21
[51] Tao J, Perdew J P, Staroverov V N and Scuseria G E 2003 Climbing the density functional ladder: nonempirical meta-generalized gradient approximation designed for molecules and solids *Phys. Rev. Lett.* **91** 146401
[52] Sun J, Ruzsinszky A and Perdew J 2015 Strongly constrained and appropriately normed semilocal density functional *Phys. Rev. Lett.* **115** 036402
[53] Sun J *et al* 2015 SCAN: an efficient density functional yielding accurate structures and energies of diversely-bonded materials (arXiv: 1511.01089)
[54] Grimme S 2006 Semiempirical hybrid density functional with perturbative second-order correlation *J. Chem. Phys.* **124** 034108
[55] Karton A, Tarnopolsky A, Lameère J F, Schatz G C and Martin J M L 2008 Highly accurate first-principles benchmark data sets for the parametrization and validation of density functional and other approximate methods. Derivation of a robust, generally applicable, double-hybrid functional for thermochemistry and thermochemical kinetics *J. Phys. Chem.* A **112** 12868–8
[56] Kozuch S, Gruzman D and Martin J M L 2010 DSD-BLYP: a general purpose double hybrid density functional including spin component scaling and dispersion correction *J. Phys. Chem.* C **114** 20801–8
[57] Goerigk L and Grimme S 2011 Efficient and accurate double-hybrid-meta-GGA density functionals—evaluation with the extended GMTKN30 database for general main group thermochemistry, kinetics, and noncovalent interactions *J. Chem. Theory Comput.* **7** 291–309
[58] Zhang Y, Xu X and Goddard W A 2009 Doubly hybrid density functional for accurate descriptions of nonbond interactions, thermochemistry, and thermochemical kinetics *Proc. Natl Acad. Sci.* **106** 4963–8
[59] Schwabe T and Grimme S 2007 Double-hybrid density functionals with long-range dispersion corrections: higher accuracy and extended applicability *Phys. Chem. Chem. Phys.* **9** 3397–406
[60] Ramalho J P P, Gomes J R B and Illas F 2013 Accounting for van der Waals interactions between adsorbates and surfaces in density functional theory based calculations: selected examples *RSC Adv.* **3** 13085
[61] Grimme S 2011 Density functional theory with London dispersion corrections *WIREs Comput. Mol. Sci.* **1** 211–28
[62] Stöhr M, Van Voorhis T and Tkatchenko A 2019 Theory and practice of modeling van der Waals interactions in electronic-structure calculations *Chem. Soc. Rev.* **48** 4118–54
[63] Dion M, Rydberg H, Schröder E, Langreth D C and Lundqvist B I 2004 Van der Waals density functional for general geometries *Phys. Rev. Lett.* **92** 246401
[64] Wu X, Vargas M C, Nayak S, Lotrich V and Scoles G 2001 Towards extending the applicability of density functional theory to weakly bound systems *J. Chem. Phys.* **115** 8748–57
[65] Grimme S 2004 Accurate description of van der Waals complexes by density functional theory including empirical corrections *J. Comput. Chem.* **25** 1463–73
[66] Grimme S 2006 Semiempirical GGA-type density functional constructed with a long-range dispersion correction *J. Comput. Chem.* **27** 1787–99
[67] Grimme S, Antony J, Ehrlich S and Krieg H 2010 A consistent and accurate *ab initio* parametrization of density functional dispersion correction (DFT-D) for the 94 elements H-Pu *J. Chem. Phys.* **132** 154104
[68] Tkatchenko A and Scheffler M 2009 Accurate molecular van der Waals interactions from ground-state electron density and free-atom reference data *Phys. Rev. Lett.* **102** 073005
[69] Johnson E R and Becke A D 2005 A post-Hartree–Fock model of intermolecular interactions *J. Chem. Phys.* **123** 024101
[70] Olasz A, Vanommeslaeghe K, Krishtal A, Veszprémi T, Van Alsenoy C and Geerlings P 2007 The use of atomic intrinsic polarizabilities in the evaluation of the dispersion energy *J. Chem. Phys.* **127** 224105

[71] Tkatchenko A, DiStasio R A, Car R and Scheffler M 2012 Accurate and efficient method for many-body van der Waals interactions *Phys. Rev. Lett.* **108** 236402
[72] Ambrosetti A, Reilly A M, DiStasio R A and Tkatchenko A 2014 Long-range correlation energy calculated from coupled atomic response functions *J. Chem. Phys.* **140** 18A508
[73] Donchev A G 2006 Many-body effects of dispersion interaction *J. Chem. Phys.* **125** 074713
[74] Cole M W, Velegol D, Kim H-Y and Lucas A A 2009 Nanoscale van der Waals interactions *Mol. Simul.* **35** 849–66
[75] Ruiz V G, Liu W, Zojer E, Scheffler M and Tkatchenko A 2012 Density-functional theory with screened van der Waals interactions for the modeling of hybrid inorganic–organic systems *Phys. Rev. Lett.* **108** 146103
[76] Zhang G-X, Tkatchenko A, Paier J, Appel H and Scheffler M 2011 van der Waals interactions in ionic and semiconductor solids *Phys. Rev. Lett.* **107** 245501
[77] Gao W and Tkatchenko A 2013 Electronic structure and van der Waals interactions in the stability and mobility of point defects in semiconductors *Phys. Rev. Lett.* **111** 045501
[78] Hermann J, Alfè D and Tkatchenko A 2017 Nanoscale π–π stacked molecules are bound by collective charge fluctuations *Nat. Commun.* **8** 14052
[79] Schatschneider B, Liang -J-J, Reilly A M, Marom N, Zhang G-X and Tkatchenko A 2013 Electrodynamic response and stability of molecular crystals *Phys. Rev.* B **87** 060104
[80] DiStasio R A, von Lilienfeld O A and Tkatchenko A 2012 Collective many-body van der Waals interactions in molecular systems *Proc. Natl Acad. Sci.* **109** 14791–5
[81] Cui T-T, Li J-C, Gao W, Hermann J, Tkatchenko A and Jiang Q 2020 Nonlocal electronic correlations in the cohesive properties of high-pressure hydrogen solids *J. Phys. Chem. Lett.* **11** 1521–7
[82] Cui T T, Chen D, Li J C, Gao W and Jiang Q 2019 Favored decomposition paths of hydrogen sulfide at high pressure *New J. Phys.* **21** 033023
[83] Gao W and Tkatchenko A 2015 Sliding mechanisms in multilayered hexagonal boron nitride and graphene: the effects of directionality, thickness, and sliding constraints *Phys. Rev. Lett.* **114** 096101
[84] Gao W, Chen Y and Jiang Q 2016 Discriminating between metallic and semiconducting single-walled carbon nanotubes using physisorbed adsorbates: role of wavelike charge-density fluctuations *Phys. Rev. Lett.* **117** 246101
[85] Ambrosetti A, Ferri N, DiStasio R A and Tkatchenko A 2016 Wavelike charge density fluctuations and van der Waals interactions at the nanoscale *Science* **351** 1171–6
[86] DiStasio R A, Gobre V V and Tkatchenko A 2014 Many-body van der Waals interactions in molecules and condensed matter *J. Phys. Condens. Matter* **26** 213202
[87] Maurer R J, Ruiz V G, Camarillo-Cisneros J, Liu W, Ferri N, Reuter K and Tkatchenko A 2016 Adsorption structures and energetics of molecules on metal surfaces: bridging experiment and theory *Prog. Surf. Sci.* **91** 72–100
[88] Chen Y, Gao W and Jiang Q 2019 Molecular switch by adsorbing the Au_6 cluster on single-walled carbon nanotubes: role of many-body effects of vdW forces *J. Phys. Chem.* C **123** 9217–22
[89] Kühne T D 2014 Second generation Car-Parrinello molecular dynamics *Wiley Interdiscip. Rev.-Comput. Mol. Sci.* **4** 391–406
[90] Car R and Parrinello M 1985 Unified approach for molecular dynamics and density-functional theory *Phys. Rev. Lett.* **55** 2471–4
[91] Kaxiras E, Bar-Yam Y, Joannopoulos J D and Pandey K C 1987 *Ab initio* theory of polar semiconductor surfaces. I. Methodology and the (2x2) reconstructions of GaAs(111) *Phys. Rev.* B **35** 9625–35
[92] Qian G-X, Martin R M and Chadi D J 1988 First-principles study of the atomic reconstructions and energies of Ga- and As-stabilized GaAs(100) surfaces *Phys. Rev.* B **38** 7649–63
[93] Scheffler M and Dabrowski J 1988 Parameter-free calculations of total energies, interatomic forces and vibrational entropies of defects in semiconductors *Philos. Mag.* A **58** 107–21
[94] Weinert C M and Scheffler M 1986 *Defects in Semiconductors* von Bardeleben H J (Aedermannsdorf: Trans Tech Publications) p 25
[95] Scheffler M 1988 *Physics of Solid Surfaces—1987* (Amsterdam: Elsevier)
[96] Reuter K and Scheffler M 2003 First-principles atomistic thermodynamics for oxidation catalysis: surface phase siagrams and catalytically interesting regions *Phys. Rev. Lett.* **90** 046103
[97] Reuter K and Scheffler M 2003 Composition and structure of the RuO_2(110) surface in an O_2 and CO environment: implications for the catalytic formation of CO_2 *Phys. Rev.* B **68** 045407
[98] Kertesz M and Hoffmann R 1984 Octahedral vs. trigonal-prismatic coordination and clustering in transition-metal dichalcogenides *J. Am. Chem. Soc.* **106** 3453–60
[99] Hughbanks T and Hoffmann R 1983 Chains of trans-edge-sharing molybdenum octahedra: metal-metal bonding in extended systems *J. Am. Chem. Soc.* **105** 3528–37
[100] Wijeyesekera S D and Hoffmann R 1984 Transition metal carbides. A comparison of bonding in extended and molecular interstitial carbides *Organometallics* **3** 949–61
[101] Saillard J Y and Hoffmann R 1984 Carbon-hydrogen and hydrogen-hydrogen activation in transition metal complexes and on surfaces *J. Am. Chem. Soc.* **106** 2006–26
[102] Hoffman R 1988 *Solids and Surfaces: A Chemist's View of Bonding in Extended Structures* (New York: Wiley)
[103] Dronkowski R 2005 *Computational Chemistry of Solid State Materials: A Guide for Materials Scientists, Chemists, Physicists and Others* (New York: Wiley)
[104] Mulliken R S 1955 Electronic population analysis on LCAO-MO molecular wave functions. IV. Bonding and antibonding in LCAO and valence-bond theories *J. Chem. Phys.* **23** 2343–6
[105] Hoffmann R 1988 A chemical and theoretical way to look at bonding on surfaces *Rev. Mod. Phys.* **60** 601–28
[106] Blyholder G 1964 Molecular orbital view of chemisorbed carbon monoxide *J. Phys. Chem.* **68** 2772–7
[107] Nørskov J K and Lang N D 1980 Effective-medium theory of chemical binding: application to chemisorption *Phys. Rev.* B **21** 2131–6
[108] Lang N D 1973 *Solid State Physics* vol 28 (New York: Academic) p 225
[109] Anderson P W 1961 Localized magnetic states in metals *Phys. Rev.* **124** 41–53
[110] Newns D M 1969 Self-consistent model of hydrogen chemisorption *Phys. Rev.* **178** 1123–35
[111] Bligaard T and Nørskov J K 2008 *Chapter 4 in 'Chemical Bonding at Surfaces and Interfaces'* (Amsterdam: Elsevier)
[112] Vojvodic A, Nørskov J K and Abild-Pedersen F 2014 Electronic structure effects in transition metal surface chemistry *Top. Catal.* **57** 25–32
[113] Hammer B and Nørskov J K 1997 *Chemisorption and Reactivity on Supported Clusters and Thin Films* (Dordrecht: Kluwer Academic) pp 285–351

[114] Hammer B and Scheffler M 1995 Local chemical reactivity of a metal alloy surface *Phys. Rev. Lett.* **74** 3487–90
[115] Hammer B, Morikawa Y and Nørskov J K 1996 CO chemisorption at metal surfaces and overlayers *Phys. Rev. Lett.* **76** 2141–4
[116] Gil A, Clotet A, Ricart J M, Kresse G, García-Hernández M, Rösch N and Sautet P 2003 Site preference of CO chemisorbed on Pt(111) from density functional calculations *Surf. Sci.* **530** 71–87
[117] Mason S E, Grinberg I and Rappe A M 2004 First-principles extrapolation method for accurate CO adsorption energies on metal surfaces *Phys. Rev.* B **69** 161401
[118] Stampfl C, Schwegmann S, Over H, Scheffler M and Ertl G 1996 Structure and stability of a high-coverage (1x1) oxygen phase on Ru(0001) *Phys. Rev. Lett.* **77** 3371–4
[119] Stampfl C, Kreuzer H J, Payne S H, Pfnür H and Scheffler M 1999 First-principles theory of surface thermodynamics and kinetics *Phys. Rev. Lett.* **83** 2993–6
[120] Diekhöner L, Mortensen H, Åkerlund C, Baurichter A and Luntz A C 2001 Dynamic displacement of N_2 from Ru(0001) by incident D and H atoms *J. Chem. Phys.* **114** 4215–20
[121] Hammer B and Nørskov J K 1997 Adsorbate reorganization at steps: NO on Pd(211) *Phys. Rev. Lett.* **79** 4441–4
[122] Mortensen J J, Morikawa Y, Hammer B and Nørskov J K 1997 Density functional calculations of N_2 adsorption and dissociation on a Ru(0001) surface *J. Catal.* **169** 85–92
[123] Luo M and Guo S 2017 Strain-controlled electrocatalysis on multimetallic nanomaterials *Nat. Rev. Mater.* **2** 17059
[124] Shu D J, Liu F and Gong X G 2001 Simple generic method for predicting the effect of strain on surface diffusion *Phys. Rev.* B **64** 245410
[125] Deng Q, Gopal V and Weissmüller J 2015 Less noble or more noble: how strain affects the binding of oxygen on gold *Angew. Chem., Int. Ed.* **54** 12981–5
[126] Francis M F and Curtin W A 2015 Mechanical work makes important contributions to surface chemistry at steps *Nat. Commun.* **6** 6261
[127] Liu F, Wu C, Yang G and Yang S 2015 CO oxidation over strained Pt(100) surface: a DFT study *J. Phys. Chem.* C **119** 15500–5
[128] Pala R G S and Liu F 2004 Determining the adsorptive and catalytic properties of strained metal surfaces using adsorption-induced stress *J. Chem. Phys.* **120** 7720–4
[129] Roudgar A and Groß A 2003 Local reactivity of metal overlayers: density functional theory calculations of Pd on Au *Phys. Rev.* B **67** 033409
[130] Sakong S and Groß A 2003 Dissociative adsorption of hydrogen on strained Cu surfaces *Surf. Sci.* **525** 107–18
[131] Shuttleworth I G 2017 Strain engineering of H/transition metal systems *Surf. Sci.* **661** 49–59
[132] Mavrikakis M, Hammer B and Nørskov J K 1998 Effect of strain on the reactivity of metal surfaces *Phys. Rev. Lett.* **81** 2819–22
[133] Calle-Vallejo F and Bandarenka A S 2018 Enabling generalized coordination numbers to describe strain effects *ChemSusChem* **11** 1824–8
[134] Khorshidi A, Violet J, Hashemi J and Peterson A A 2018 How strain can break the scaling relations of catalysis *Nat. Catal.* **1** 263–8
[135] Andersson K J, Calle-Vallejo F, Rossmeisl J and Chorkendorff I 2009 Adsorption-driven surface segregation of the less reactive alloy component *J. Am. Chem. Soc.* **131** 2404–7
[136] Knudsen J, Nilekar A U, Vang R T, Schnadt J, Kunkes E L, Dumesic J A, Mavrikakis M and Besenbacher F 2007 A Cu/Pt near-surface alloy for water−gas shift catalysis *J. Am. Chem. Soc.* **129** 6485–90
[137] Stephens I E L *et al* 2011 Tuning the activity of Pt(111) for oxygen electroreduction by subsurface alloying *J. Am. Chem. Soc.* **133** 5485–91
[138] Calle-Vallejo F, Martínez J I, García-Lastra J M, Rossmeisl J and Koper M T M 2012 Physical and chemical nature of the scaling relations between adsorption energies of atoms on metal surfaces *Phys. Rev. Lett.* **108** 116103
[139] Mitchell P R and Parish R V 1969 The eighteen-electron rule *J. Chem. Educ.* **46** 811–4
[140] Tolman C A 1972 The 16 and 18 electron rule in organometallic chemistry and homogeneous catalysis *Chem. Soc. Rev.* **1** 337–53
[141] Xin H, Holewinski A, Schweitzer N, Nikolla E and Linic S 2012 Electronic structure engineering in heterogeneous catalysis: identifying novel alloy catalysts based on rapid screening for materials with desired electronic properties *Top. Catal.* **55** 376–90
[142] Desjonqueres M-C and Spanjaard D 1993 *Concepts in Surface Physics* (Berlin: Springer)
[143] Barreteau C, Spanjaard D and Desjonquères M C 1999 Electronic structure and energetics of transition metal surfaces and clusters from a new spd tight-binding method *Surf. Sci.* **433** 751–5
[144] Mehl M J and Papaconstantopoulos D A 1996 Applications of a tight-binding total-energy method for transition and noble metals: elastic constants, vacancies, and surfaces of monatomic metals *Phys. Rev.* B **54** 4519–30
[145] Bockris J O 1984 The electrocatalysis of oxygen evolution on perovskites *J. Electrochem. Soc.* **131** 290
[146] Matsumoto Y and Sato E 1986 Electrocatalytic properties of transition metal oxides for oxygen evolution reaction *Mater. Chem. Phys.* **14** 397–426
[147] Tejuca L G, Fierro J L G and Tascón J M D 1989 Structure and reactivity of perovskite-type oxides *Adv. Catal.* **36** 237–3288
[148] Trasatti S 1984 Electrocatalysis in the anodic evolution of oxygen and chlorine *Electrochim. Acta* **29** 1503–12
[149] Suntivich J, May K J, Gasteiger H A, Goodenough J B and Shao-Horn Y 2011 A perovskite oxide optimized for oxygen evolution catalysis from molecular orbital principles *Science* **334** 1383–5
[150] Suntivich J, Gasteiger H A, Yabuuchi N, Nakanishi H, Goodenough J B and Shao-Horn Y 2011 Design principles for oxygen-reduction activity on perovskite oxide catalysts for fuel cells and metal-air batteries *Nat. Chem.* **3** 546–50
[151] Stambouli A B and Traversa E 2002 Solid oxide fuel cells (SOFCs): a review of an environmentally clean and efficient source of energy *Renew. Sustain. Energy Rev.* **6** 433–55
[152] Calle-Vallejo F, Inoglu N G, Su H Y, Martínez J I, Man I C, Koper M T M, Kitchin J R and Rossmeisl J 2013 Number of outer electrons as descriptor for adsorption processes on transition metals and their oxides *Chem. Sci.* **4** 1245–9
[153] Xu Z and Kitchin J R 2014 Relating the electronic structure and reactivity of the 3d transition metal monoxide surfaces *Catal. Commun.* **52** 60–64
[154] Dickens C F, Montoya J H, Kulkarni A R, Bajdich M and Nørskov J K 2019 An electronic structure descriptor for oxygen reactivity at metal and metal-oxide surfaces *Surf. Sci.* **681** 122–9
[155] Montoya J H, Doyle A D, Nørskov J K and Vojvodic A 2018 Trends in adsorption of electrocatalytic water splitting intermediates on cubic ABO_3 oxides *Phys. Chem. Chem. Phys.* **20** 3813–8
[156] Lefèvre M, Proietti E, Jaouen F and Dodelet J P 2009 Iron-based catalysts with improved oxygen reduction activity in polymer electrolyte fuel cells *Science* **324** 71–74
[157] Wu G, More K L, Johnston C M and Zelenay P 2011 High-performance electrocatalysts for oxygen reduction derived from polyaniline, iron, and cobalt *Science* **332** 443–7

[158] Qiao B, Wang A, Yang X, Allard L F, Jiang Z, Cui Y, Liu J, Li J and Zhang T 2011 Single-atom catalysis of CO oxidation using Pt_1/FeO_x *Nat. Chem.* **3** 634–41
[159] Zhang X, Guo J, Guan P, Liu C, Huang H, Xue F, Dong X, Pennycook S J and Chisholm M F 2013 Catalytically active single-atom niobium in graphitic layers *Nat. Commun.* **4** 1924
[160] Fei H *et al* 2015 Atomic cobalt on nitrogen-doped graphene for hydrogen generation *Nat. Commun.* **6** 8668
[161] Chen X, Chen S and Wang J 2016 Screening of catalytic oxygen reduction reaction activity of metal-doped graphene by density functional theory *Appl. Surf. Sci.* **379** 291–5
[162] Li X, Zhong W, Cui P, Li J and Jiang J 2016 Design of efficient catalysts with double transition metal atoms on C_2N layer *J. Phys. Chem. Lett.* **7** 1750–5
[163] Fan L, Liu P F, Yan X, Gu L, Yang Z Z, Yang H G, Qiu S and Yao X 2016 Atomically isolated nickel species anchored on graphitized carbon for efficient hydrogen evolution electrocatalysis *Nat. Commun.* **7** 10667
[164] Chen Y *et al* 2017 Isolated single iron atoms anchored on N-doped porous carbon as an efficient electrocatalyst for the oxygen reduction reaction *Angew. Chem., Int. Ed.* **56** 6937–41
[165] Chen W *et al* 2017 Rational design of single molybdenum atoms anchored on N-doped carbon for effective hydrogen evolution reaction *Angew. Chem. Int. Ed.* **56** 16086–90
[166] Wang Y, Song E, Qiu W, Zhao X, Zhou Y, Liu J and Zhang W 2019 Recent progress in theoretical and computational investigations of structural stability and activity of single-atom electrocatalysts *Prog. Nat. Sci. Mater. Int.* **29** 256–64
[167] Yang X, Wang A, Qiao B, Li J, Liu J and Zhang T 2013 Single-atom catalysts: a new frontier in heterogeneous catalysis *Acc. Chem. Res.* **46** 1740–8
[168] Xu H, Cheng D, Cao D and Zeng X C 2018 A universal principle for a rational design of single-atom electrocatalysts *Nat. Catal.* **1** 339–48
[169] Zheng Y, Jiao Y, Jaroniec M and Qiao S Z 2015 Advancing the electrochemistry of the hydrogen-evolution reaction through combining experiment *Angew. Chem., Int. Ed.* **54** 52–65
[170] Fajín J L C, DS Cordeiro M N and Gomes J R B 2014 Density functional theory study of the water dissociation on platinum surfaces: general trends *J. Phys. Chem.* A **118** 5832–40
[171] Kleis J *et al* 2011 Finite size effects in chemical bonding: from small clusters to solids *Catal. Lett.* **141** 1067–71
[172] Shustorovich E and Sellers H 1998 The UBI-QEP method: a practical theoretical approach to understanding chemistry on transition metal surfaces *Surf. Sci. Rep.* **31** 1–119
[173] Kratzer P, Hammer B and Nørskov J K 1996 Geometric and electronic factors determining the differences in reactivity of H_2 on Cu(100) and Cu(111) *Surf. Sci.* **359** 45–53
[174] Hammer B, Nielsen O H and Nørskov J K 1997 Structure sensitivity in adsorption: CO interaction with stepped and reconstructed Pt surfaces *Catal. Lett.* **46** 31–35
[175] Swalin R A 1963 *Thermodynamics of Solids* (New York: Wiley)
[176] Methfessel M, Hennig D and Scheffler M 1992 Trends of the surface relaxations, surface energies, and work functions of the 4d transition metals *Phys. Rev.* B **46** 4816–29
[177] Jiang Q, Lu H M and Zhao M 2004 Modelling of surface energies of elemental crystals *J. Phys. Condens. Matter* **16** 521–30
[178] Ma X and Xin H 2017 Orbitalwise coordination number for predicting adsorption properties of metal nanocatalysts *Phys. Rev. Lett.* **118** 036101
[179] Gaspard J P and Cyrot-Lackmann F 1973 Density of states from moments. Application to the impurity band *J. Phys.* C **6** 3077–96
[180] Koper M T M 2011 Thermodynamic theory of multi-electron transfer reactions: implications for electrocatalysis *J. Electroanal. Chem.* **660** 254–60
[181] Xin H, Holewinski A and Linic S 2012 Predictive structure–reactivity models for rapid screening of Pt-based multimetallic electrocatalysts for the oxygen reduction reaction *ACS Catal.* **2** 12–16
[182] Ma X, Li Z, Achenie L E K and Xin H 2015 Machine-learning-augmented chemisorption model for CO_2 electroreduction catalyst screening *J. Phys. Chem. Lett.* **6** 3528–33
[183] Bhowmik A, Vegge T and Hansen H A 2016 Descriptors and thermodynamic limitations of electrocatalytic carbon dioxide reduction on rutile oxide surfaces *ChemSusChem* **9** 3230–43
[184] Fernndez E M *et al* 2008 Scaling relationships for adsorption energies on transition metal oxide, sulfide, and nitride surfaces *Angew. Chem., Int. Ed.* **47** 4683–6
[185] Dong C, Fu J, Liu H, Ling T, Yang J, Qiao S Z and Du X W 2017 Tuning the selectivity and activity of Au catalysts for carbon dioxide electroreduction via grain boundary engineering: a DFT study *J. Mater. Chem.* A **5** 7184–90
[186] Xu H, Cheng D, Gao Y and Zeng X C 2018 Assessment of catalytic activities of gold nanoclusters with simple structure descriptors *ACS Catal.* **8** 9702–10
[187] Hong X, Chan K, Tsai C and Nørskov J K 2016 How doped MoS_2 breaks transition-metal scaling relations for CO_2 electrochemical reduction *ACS Catal.* **6** 4428–37
[188] Back S and Jung Y 2017 TiC- and TiN-supported single-atom catalysts for dramatic improvements in CO_2 electrochemical reduction to CH_4 *ACS Energy Lett.* **2** 969–75
[189] Kirk C, Chen L D, Siahrostami S, Karamad M, Bajdich M, Voss J, Nørskov J K and Chan K 2017 Theoretical investigations of the electrochemical reduction of CO on single metal atoms embedded in graphene *ACS Cent. Sci.* **3** 1286–93
[190] Back S, Lim J, Kim N Y, Kim Y H and Jung Y 2017 Single-atom catalysts for CO_2 electroreduction with significant activity and selectivity improvements *Chem. Sci.* **8** 1090–6
[191] Back S, Kim H and Jung Y 2015 Selective heterogeneous CO_2 electroreduction to methanol *ACS Catal.* **5** 965–71
[192] Hummelshøj J S, Abild-Pedersen F, Studt F, Bligaard T and Nørskov J K 2012 CatApp: a web application for surface chemistry and heterogeneous catalysis *Angew. Chem., Int. Ed.* **51** 272–4
[193] Greeley J, Rossmeisl J, Hellmann A and Norskov J K 2007 Theoretical trends in particle size effects for the oxygen reduction reaction *Z. Phys. Chem.* **221** 1209–20
[194] Nørskov J K, Rossmeisl J, Logadottir A, Lindqvist L, Kitchin J R, Bligaard T and Jónsson H 2004 Origin of the overpotential for oxygen reduction at a fuel-cell cathode *J. Phys. Chem.* B **108** 17886–92
[195] Bard A J and Fox M A 1995 Artificial photosynthesis: solar splitting of water to hydrogen and oxygen *Acc. Chem. Res.* **28** 141–5
[196] Lewis N S and Nocera D G 2006 Powering the planet: chemical challenges in solar energy utilization *Proc. Natl Acad. Sci.* **103** 15729–35
[197] Sealy C 2008 The problem with platinum *Mater. Today* **11** 65–68

[198] Wang Z, Zhao D, Yu S, Nie Z, Li Y and Zhang L 2019 First-principles investigation of structural and electronic properties of oxygen adsorbing phosphorene *Prog. Nat. Sci. Mater. Int.* **29** 316–21

[199] Zhao C, Gao W and Jiang Q 2019 CO adsorption on metal doped 2D InSe: mechanism and application *Prog. Nat. Sci. Mater. Int.* **29** 305–9

[200] Yang X, Hu Q, Hou X, Mi J and Zhang P 2018 Oxygen reduction reaction on M_3(hexaiminobenzene)$_2$: a density function theory study *Catal. Commun.* **115** 17–20

[201] Stamenkovic V, Mun B S, Mayrhofer K J J, Ross P N, Markovic N M, Rossmeisl J, Greeley J and Nørskov J K 2006 Changing the activity of electrocatalysts for oxygen reduction by tuning the surface electronic structure *Angew. Chem., Int. Ed.* **45** 2897–901

[202] Escudero-Escribano M, Malacrida P, Hansen M H, Vej-Hansen U G, Velazquez-Palenzuela A, Tripkovic V, Schiotz J, Rossmeisl J, Stephens I E L and Chorkendorff I 2016 Tuning the activity of Pt alloy electrocatalysts by means of the lanthanide contraction *Science* **352** 73–76

[203] Mistry H, Varela A S, Kühl S, Strasser P and Cuenya B R 2016 Nanostructured electrocatalysts with tunable activity and selectivity *Nat. Rev. Mater.* **1** 16009

[204] Wang H *et al* 2016 Direct and continuous strain control of catalysts with tunable battery electrode materials *Science* **354** 1031–6

[205] Tripkovic V, Hansen H A, Rossmeisl J and Vegge T 2015 First principles investigation of the activity of thin film Pt, Pd and Au surface alloys for oxygen reduction *Phys. Chem. Chem. Phys.* **17** 11647–57

[206] Zhao C X, Gao W and Jiang Q 2020 Scheme for screening O_2 reduction electrocatalysts: from pure metals and alloys to single-atom catalysts *J. Phys. Chem.* C **124** 25412–20

[207] Greeley J and Nørskov J K 2009 Combinatorial density functional theory-based screening of surface alloys for the oxygen reduction reaction *J. Phys. Chem.* C **113** 4932–9

[208] Kulkarni A, Siahrostami S, Patel A and Nørskov J K 2018 Understanding catalytic activity trends in the oxygen reduction reaction *Chem. Rev.* **118** 2302–12

[209] Appel A M *et al* 2013 Frontiers, opportunities, and challenges in biochemical and chemical catalysis of CO_2 fixation *Chem. Rev.* **113** 6621–58

[210] Hori Y 2008 Electrochemical CO_2 reduction on metal electrodes *Mod. Asp. Electrochem.* **42** 89–189

[211] Gao S *et al* 2016 Ultrathin Co_3O_4 Layers realizing optimized CO_2 electroreduction to formate *Angew. Chem., Int. Ed.* **55** 698–702

[212] Gao S, Lin Y, Jiao X, Sun Y, Luo Q, Zhang W, Li D, Yang J and Xie Y 2016 Partially oxidized atomic cobalt layers for carbon dioxide electroreduction to liquid fuel *Nature* **529** 68–71

[213] Kim D, Resasco J, Yu Y, Asiri A M and Yang P 2014 Synergistic geometric and electronic effects for electrochemical reduction of carbon dioxide using gold-copper bimetallic nanoparticles *Nat. Commun.* **5** 1–8

[214] Bai X, Chen W, Zhao C, Li S, Song Y, Ge R, Wei W and Sun Y 2017 Exclusive formation of formic acid from CO_2 electroreduction by a tunable Pd–Sn alloy *Angew. Chem., Int. Ed.* **56** 12219–23

[215] Tripkovic V, Vanin M, Karamad M, Björketun M E, Jacobsen K W, Thygesen K S and Rossmeisl J 2013 Electrochemical CO_2 and CO reduction on metal-functionalized porphyrin-like graphene *J. Phys. Chem.* C **117** 9187–95

[216] Zhang P, Yang X, Hou X, Xu X, Xiao B, Huang J and Stampfl C 2019 Metal-bipyridine complexes as electrocatalysts for the reduction of CO_2: a density functional theory study *Phys. Chem. Chem. Phys.* **21** 23742–8

[217] Feaster J T, Shi C, Cave E R, Hatsukade T, Abram D N, Kuhl K P, Hahn C, Nørskov J K and Jaramillo T F 2017 Understanding selectivity for the electrochemical reduction of carbon dioxide to formic acid and carbon monoxide on metal electrodes *ACS Catal.* **7** 4822–7

[218] Guan X, Zhao C X, Liu X, Liu S P, Gao W and Jiang Q 2020 Universal principle to describe reactivity and selectivity of CO_2 electroreduction on transition metals and single-atom catalysts *J. Phys. Chem.* C **124** 25898–906

[219] Yoo J S, Christensen R, Vegge T, Nørskov J K and Studt F 2016 Theoretical insight into the trends that guide the electrochemical reduction of carbon dioxide to formic acid *ChemSusChem* **9** 358–63

[220] Kuhl K P, Hatsukade T, Cave E R, Abram D N, Kibsgaard J and Jaramillo T F 2014 Electrocatalytic conversion of carbon dioxide to methane and methanol on transition metal surfaces *J. Am. Chem. Soc.* **136** 14107–13

[221] Nørskov J K, Bligaard T, Logadottir A, Kitchin J R, Chen J G, Pandelov S and Stimming U 2005 Trends in the exchange current for hydrogen evolution *J. Electrochem. Soc.* **152** J23

[222] Qi L J, Gao W and Jiang Q 2020 Effective descriptor for designing high-performance catalysts for the hydrogen evolution reaction *J. Phys. Chem.* C **124** 23134–42

[223] Ju W, Bagger A, Hao G-P, Varela A S, Sinev I, Bon V, Roldan Cuenya B, Kaskel S, Rossmeisl J and Strasser P 2017 Understanding activity and selectivity of metal-nitrogen-doped carbon catalysts for electrochemical reduction of CO_2 *Nat. Commun.* **8** 944

[224] Erisman J W, Sutton M A, Galloway J, Klimont Z and Winiwarter W 2008 How a century of ammonia synthesis changed the world *Nat. Geosci.* **1** 636–9

[225] Service A R F 2014 New recipe produces ammonia from air, water, and sunlight *Science* **345** 610–610

[226] Saadatjou N, Jafari A and Sahebdelfar S 2015 Ruthenium nanocatalysts for ammonia synthesis: a review *Chem. Eng. Commun.* **202** 420–48

[227] Fang Y, Liu Z, Han J, Jin Z, Han Y, Wang F, Niu Y, Wu Y and Xu Y 2019 High-performance electrocatalytic conversion of N_2 to NH_3 using oxygen-vacancy-rich TiO_2*in situ* grown on $Ti_3C_2T_x$ MXene *Adv. Energy Mater.* **9** 1803406

[228] Suryanto B H R, Wang D, Azofra L M, Harb M, Cavallo L, Jalili R, Mitchell D R G, Chatti M and MacFarlane D R 2019 MoS_2 polymorphic engineering enhances selectivity in the electrochemical reduction of nitrogen to ammonia *ACS Energy Lett.* **4** 430–5

[229] Geng Z, Liu Y, Kong X, Li P, Li K, Liu Z, Du J, Shu M, Si R and Zeng J 2018 Achieving a record-high yield rate of 120.9 μg_{NH3} mgcat.$^{-1}$ h^{-1} for N_2 electrochemical reduction over Ru single-atom catalysts *Adv. Mater.* **30** 1803498

[230] Chen Z W, Yan J and Jiang Q 2019 Single or double: which is the altar of atomic catalysts for nitrogen reduction reaction? *Small Methods* **3** 1800291

[231] Montoya J H, Tsai C, Vojvodic A and Nørskov J K 2015 The challenge of electrochemical ammonia synthesis: a new perspective on the role of nitrogen scaling relations *ChemSusChem* **8** 2180–6

[232] Yang D, Chen T and Wang Z 2017 Electrochemical reduction of aqueous nitrogen (N_2) at a low overpotential on (110)-oriented Mo nanofilm *J. Mater. Chem.* A **5** 18967–71

[233] Roling L T and Abild-Pedersen F 2018 Structure-sensitive scaling relations: adsorption energies from surface site stability *ChemCatChem* **10** 1643–50

[234] Dean J, Taylor M G and Mpourmpakis G 2019 Unfolding adsorption on metal nanoparticles: connecting stability with catalysis *Sci. Adv.* **5** eaax5101

[235] Ferrin P, Simonetti D, Kandoi S, Kunkes E, Dumesic J A, Nørskov J K and Mavrikakis M 2009 Modeling ethanol decomposition on transition metals: a combined application of scaling and Brønsted-Evans-Polanyi relations *J. Am. Chem. Soc.* **131** 5809–15
[236] Cheng J, Hu P, Ellis P, French S, Kelly G and Lok C M 2008 Brønsted–Evans–Polanyi relation of multistep reactions and volcano curve in heterogeneous catalysis *J. Phys. Chem.* C **112** 1308–11
[237] van Santen R A, Neurock M and Shetty S G 2010 Reactivity theory of transition-metal surfaces: a Brønsted−Evans−Polanyi linear activation energy−free-energy analysis *Chem. Rev.* **110** 2005–48
[238] Juaristi J I, Alducin M, Muiño R D, Busnengo H F and Salin A 2008 Role of electron-hole pair excitations in the dissociative adsorption of diatomic molecules on metal surfaces *Phys. Rev. Lett.* **100** 116102
[239] Rittmeyer S P, Meyer J, Juaristi J I and Reuter K 2015 Electronic friction-based vibrational lifetimes of molecular adsorbates: beyond the independent-atom approximation *Phys. Rev. Lett.* **115** 046102
[240] Askerka M, Maurer R J, Batista V S and Tully J C 2016 Role of tensorial electronic friction in energy transfer at metal surfaces *Phys. Rev. Lett.* **116** 217601
[241] Rittmeyer S P, Ward D J, Gütlein P, Ellis J, Allison W and Reuter K 2016 Energy dissipation during diffusion at metal surfaces: disentangling the role of phonons versus electron-hole pairs *Phys. Rev. Lett.* **117** 196001
[242] Maurer R J, Jiang B, Guo H and Tully J C 2017 Mode specific electronic friction in dissociative chemisorption on metal surfaces: H_2 on Ag(111) *Phys. Rev. Lett.* **118** 256001
[243] Rittmeyer S P, Meyer J and Reuter K 2017 Nonadiabatic vibrational damping of molecular adsorbates: insights into electronic friction and the role of electronic coherence *Phys. Rev. Lett.* **119** 176808